

ABSTRACT

Title of dissertation: METALS AND METALLIC ALLOYS
FOR ENERGY HARVESTING
AND STORAGE

Chen Gong, Doctor of Philosophy, 2018

Dissertation directed by: Professor Marina S. Leite
Department of Materials Science
and Engineering
The Institute for Research in
Electronics and Applied Physics

Metals have been widely used for harvesting and storing energy in devices such as superabsorbers and Li-ion batteries. However, incorporating metals into a wider range of energy applications is severely limited by their intrinsic optical and electrochemical properties. Therefore, in this thesis, we provide a new class of metallic materials by forming binary mixtures of Ag, Au, Cu, and Al with novel physical properties for photonics, and a comprehensive understanding of the fundamental electrochemistry in Al and Si anode all-solid-state batteries for energy storage.

The first part of my thesis focuses on developing metallic alloys with a tunable optical response. We realize a new family of metallic materials by alloying Ag, Au, and Cu with on-demand dielectric functions, which can be used in superabsorbers and hot carrier devices. We design and fabricate alloyed nanostructures with engineered optical response and spatially resolve the electric field distribution at the nanoscale by utilizing near-field scanning optical microscopy, which can potentially

enhance the performance of optoelectronic devices. To understand the physical origin of the optical response of the alloys, we measure the valence band spectra and calculate the band structures of Ag-Au alloys, providing direct evidence that the change in the electronic bands is responsible for its optical property. Further, we obtain a photonic device with superior performance using metallic alloys. Specifically, an Al-Cu/Si bilayer superabsorber is reached in a lithography-free manner with maximum absorption $> 99\%$, which can be used for energy harvesting.

The second part of my thesis highlights the importance of understanding the reactions and ion distribution in energy storage devices. We inspect how the Al electrode surface changes upon cycling and directly map the Li distribution in 3-dimensions within all-solid-state batteries by implementing time-of-flight secondary ion mass spectroscopy. This research indicates that undesired chemical reactions, including the formation of an insulating layer on the Al anode surface and the trapping of Li ions at the interfaces, hinder the cycling performance of the devices. Overall, our results will contribute to the design of energy storage devices with enhanced electrochemical performance.

METALS AND METALLIC ALLOYS
FOR ENERGY HARVESTING AND STORAGE

by

Chen Gong

Dissertation submitted to the Faculty of the Graduate School of the
University of Maryland, College Park in partial fulfillment
of the requirements for the degree of
Doctor of Philosophy
2018

Advisory Committee:

Professor Marina S. Leite, Chair/Advisor

Professor Christopher Lobb, Dean's Representative

Professor Yifei Mo

Professor Lourdes G. Salamanca-Riba

Professor Ichiro Takeuchi

© Copyright by
Chen Gong
2018

Dedication

To my mom, dad, and my wife.

Love you.

Acknowledgments

First and foremost, I would like to acknowledge my advisor Professor Marina S. Leite for offering me this incredible opportunity to work here and supporting me during this wonderful journey. Her mentorship has been extremely helpful. Her vision and pursuit of perfection ensure the quality of the work. Her enthusiasm and encouragement always motivate me. During my staying here, I have learned so much from her in many aspects, from designing the experimental to presenting the results. It is my privilege and it has been a great pleasure to work with such an extraordinary individual.

I must acknowledge my committee members for their valuable time and input of my dissertation, which have included Professors Christopher Lobb, Yifei Mo, Lourdes G. Salamanca-Riba, and Ichiro Takeuchi. Particularly, this thesis will not be completed without the collaborations from Professor Lourdes G. Salamanca-Riba and Dr. Joshua A. Taillon on the alloy nanoparticles project, and the help from Professor Ichiro Takeuchi and Dr. Yangang Liang for the AFM measurement. I would also like to thank Professor Yifei Mo for the fruitful discussion on the battery work and Professor Christopher Lobb for being the dean's representative and inviting me to present my work at the CNAM talk.

I want to thank all my collaborators at the University of Maryland, National Institute of Standards and Technology, U.S. Army Research Laboratory, Sandia National Laboratories, and Sao Paulo State University. Much of this work would not be possible without our collaborators. Thanks Professor Jeremy N. Munday and

the team for the help and discussions, just to name a few, Dr. Joseph Garrett, Dr. Tao Gong, Dr. Dongheon Ha, Dr. Dakang Ma, Dr. Joseph Murray, Dr. Yunlu Xu, Lisa J. Krayner, Kevin Palm, and David A.T. Somers. I would like to thank Professor Gary Rubloff and Dr. Alexander Pearse for the help on XPS measurements. Thanks Drs. Gerard Henien and Joshua Schumacher for TEM sample preparation. Thanks Drs. A. Alec Talin, Farid El Gabaly, Elliot J. Fuller, and Dmitry Ruzmetov for fabricating and charging those nice and beautiful batteries. Thanks Drs. David R. Baker and Joshua P. McClure for the valence band spectra measurements and calculations, and it has been very nice to work with Professor Alexandre A. Rocha to get those DFT calculation results.

It has been awesome to work with talents here at Maryland. I would like to acknowledge Dr. Elizabeth M. Tennyson. We started from day one and have a great chemistry working together. I am so fortunate to know you. Professor Mariama R. S. Dias and Zackery A. Benson, working with you on the plasmonic project is fulfilled by a sense of achievement and joy. I remember all the details of going through the ups and downs together in the lab. Beth's, Mariama's, and Zack's contributions are embedded in each line of my thesis and upon that is our friendship that I will cherish forever. I also want to thank all the current members and alumni that I have worked with in the LeiteLab, including Allen Chang, John M. Howard, Zinab Jadidi, Alan Kaplan, Garrett C. Wessler, and two summer REU students, Julia Huddy and Cynthia Yu. Thank you for your help and support.

I would like to thank people who help me use many instrumentations. These include Drs. James M. O'Connor, John Abrahams, Jonathon Hummel, Mark Lecates,

and Tom Loughran of the Fablab, Drs. Wen-An Chiou, Sz-Chian Liou, and Jiancun Rao of the AIMLab, Dr. Peter Z. Zavaliy of the X-ray Crystallographic Center, Dr. Karen Gaskell of the Surface Analysis Center, and Valery Ray.

I want to acknowledge help and support from the staff members in both MSE and IREAP. Kathleen Hart, Nina K. Morris, Thomas Weimar, Bryan Quinn, Jay P, Kathryn Tracey, Taylor Prendergast, Judi Cohn Gorski, Roxanne Defendini, Edward Condon, Dorothea Brosius, Nancy Boone, Katie Holland Doyle, JoAnne Kagle, Sherri Tatum, Dr. Robert Bonenberger, Mike McNicholas, N. Adaire Parker (in no particular order). I also want to acknowledge all the funding support and fellowships that I have received.

I must single out Professor Darryll J. Pines. He has a huge impact on my decision to come here. Back in 2013, we had a great dinner at Shanghai, where he introduced me to Maryland. He always reminds me of the excellent faculty and staff, and the nice people here. It has been my honor to know and learn from him.

Last but not the least, I owe my deepest appreciation to my mother, my father and my wife, who have always stood by me and given me infinite support. They share my success and embrace the mistakes that I made. They love me not only as a son and husband, but also as an individual who has good days and bad days. I could have been nowhere close to this moment without them.

Chen Gong

College Park, MD, USA

2018 Spring

Table of Contents	vii
List of Tables	x
List of Figures	xi
1 Introduction to Energy Harvesting and Storage	1
1.1 Metals and Metallic Alloys in Photonics	1
1.2 Metals in Li-ion Batteries	7
1.3 Scope and Contributions of this Thesis	11
2 Coin-age Metal Alloys for Plasmonics	17
2.1 Introduction	19
2.2 Optical Properties of Metals and Metallic Alloys	21
2.3 Surface Plasmon Polariton Coupling Angle Measurements	37
2.4 Experimental Methods	44
2.4.1 Sample Fabrication	44
2.4.2 Transmission and Reflection Measurements	44
2.4.3 Modeling the Dielectric Function	45
2.4.4 SPP Coupling Experiments	46
2.4.5 Transmission and SPP Calculations	47
2.5 Conclusions	53
3 Optical Properties of Fully Alloyed Ag-Au Nanostructures	55
3.1 Introduction	57
3.2 Morphology, Transmission and Chemical Analysis	59
3.3 Near-field Optical Response: Experiments and Simulations	73
3.4 Experimental Methods	77
3.4.1 Fabrication of Alloyed Nanostructures	77
3.4.2 Macroscopic Transmission Measurements	78
3.4.3 Chemical Composition Analysis	78
3.5 Conclusions	78
4 Band Structure Engineering by Alloying for Plasmonics	81
4.1 Introduction	83
4.2 Tunable Dispersion Relations	85

4.3	Electronic Band Structures for Metallic Alloys	93
4.4	Experimental Methods	100
4.4.1	Sample Fabrication	100
4.4.2	Energy-dispersive X-ray Spectroscopy	100
4.4.3	Reflection and Transmission Spectra	100
4.4.4	Reflectivity Maps	101
4.4.5	Valence Band Measurement	101
4.4.6	Density of States Calculation	102
4.4.7	Element-projected Band Structure Calculations	103
4.5	Conclusions	103
5	Al-Cu/Si for Lithography-free Thin-film Superabsorbers	105
5.1	Introduction	107
5.2	Materials Selection for Near-unity Absorption	110
5.3	Superabsorbers: Simulation and Experiment	121
5.4	Experimental Methods	129
5.4.1	Sample Fabrication	129
5.4.2	Dielectric Function Model	129
5.4.3	Absorption Maps	130
5.4.4	Elemental Analysis	130
5.4.5	Transfer Matrix Method	131
5.4.6	Numerical Simulations	132
5.5	Conclusions	133
6	Aluminum for All-solid-state Li-ion Batteries	137
6.1	Introduction	139
6.2	Effect of Surface Reactions on the Electrochemical Performance	141
6.3	Excellent Cycling Performance of Silicon Anode	146
6.4	Experimental Methods	150
6.4.1	All-solid-state Battery Fabrication	150
6.4.2	High-resolution XPS Measurements	151
6.4.3	Conductive AFM Measurements	151
6.4.4	Cross-section SEM Imaging of Batteries	152
6.5	Conclusions	153
7	3D Tomography of Li ions in All-solid-state Batteries	155
7.1	Introduction	157
7.2	3D Lithium Mapping in All-solid-state Batteries	160
7.3	Universality of the Imaging Method	169
7.4	Experimental Methods	173
7.4.1	Battery Fabrication	173
7.4.2	ToF-SIMS Imaging	173
7.5	Conclusions	174
8	Conclusions and Outlook	177

A	Products of This Research	182
A.1	Awards/Honors	182
A.2	Publications/Presentations	182
A.2.1	Publications Related to This Thesis	182
A.2.2	Additional Publications during Ph.D.	184
A.2.3	Oral Presentations	184
A.2.4	Poster Presentations	188
A.3	Students Mentored during Ph.D.	190
	Bibliography	192

List of Tables

2.1	Chemical composition for noble metal alloy thin films	49
2.2	Optical properties for Ag-Au thin films	50
2.3	Optical properties for Au-Cu thin films	51
2.4	Optical properties for Cu-Ag thin films	52
3.1	Statistical parameters for Ag-Au alloy nanoparticles	62
3.2	Chemical composition of Ag-Au alloy nanoparticles	71
4.1	Chemical and optical properties of Ag-Au alloy thin films	86
4.2	Peak position extracted from valence band spectra of Ag-Au alloy thin films	96
5.1	Chemical composition for Al-Cu thin films	113

List of Figures

1.1	Intrinsic permittivity of pure metals	2
1.2	Schematic showing how all-solid-state batteries work	9
2.1	Illustration of noble metal alloys for plasmonics	17
2.2	Thin-film noble metal alloys with on-demand optical response	22
2.3	Chemical composition analysis	23
2.4	Morphology of pure metal thin films	24
2.5	Morphology of metallic alloy thin films	25
2.6	X-ray diffraction patterns of metallic thin films	26
2.7	Transmission spectra of alloyed thin films	28
2.8	Measured dielectric function of alloyed thin films	30
2.9	Transmission electron microscope image of alloyed thin films	31
2.10	Ellipsometry data	32
2.11	Measured and calculated dielectric function of Ag-Au alloy	34
2.12	Measured and calculated dielectric function of Au-Cu alloy	35
2.13	Measured and calculated dielectric function of Cu-Ag alloy	36
2.14	Quality factor of surface plasmon polaritons for pure metal thin films	37
2.15	Propagation length of surface plasmon polaritons for alloyed thin films	38
2.16	Effect of thickness on the optical properties for alloyed thin films	39
2.17	Surface plasmon polariton excitation in noble metal alloys	41
2.18	Dielectric function of Cu thin film with and without copper oxide	42
2.19	Optical response of metal-alloyed thin films	43
3.1	Illustration of fully alloyed nanostructures	55
3.2	SEM images of alloy NPs	61
3.3	AFM image of alloy NPs	62
3.4	Macroscopic optical response of Ag-Au alloyed NPs	64
3.5	Ellipsometry results of Ag-Au alloyed thin films	65
3.6	Transmission spectra of Ag-Au alloyed thin films	65
3.7	Index of refraction for Ag-Au alloyed thin films	66
3.8	Size effect on the optical properties	66
3.9	Shape effect on the optical properties	67
3.10	Scattering and absorption efficiencies	68
3.11	Fully alloyed Ag-Au nanoparticles	70
3.12	SEM and Cross-section EDS of Ag-Au alloy NPs	70
3.13	Plan-view EDS of multiple Ag-Au alloy NPs	71

3.14	Near-field optical response of $\text{Ag}_{0.5}\text{Au}_{0.5}$ fully alloyed nanoparticles . . .	72
3.15	Near-field optical response raw data	75
3.16	Full-field simulation of light-nanoparticle interaction at the nanoscale	77
4.1	Band structure of Ag-Au alloy	81
4.2	Ag-Au alloy with tunable optical properties	87
4.3	Permittivity of Ag-Au alloy thin films	88
4.4	Reflectivity maps of Ag-Au alloy thin films	90
4.5	Dispersion relations of Ag-Au alloy thin films	92
4.6	Valence band spectra of Ag-Au alloy thin films	94
4.7	Peak fittings of valence band spectra for Ag-Au alloy thin films . . .	95
4.8	Calculated partial density of states for Ag-Au alloy thin films	95
4.9	Comparisoin of d band and transmission peak for Ag-Au alloy thin films	95
4.10	Band structure of Ag-Au alloys	98
4.11	Illustration of critical points in the Brillouin zone	99
5.1	Illustration of thin film superabsorbers	105
5.2	Subwavelength superabsorbers	111
5.3	Optical properties of metallic thin films	112
5.4	Raw ellipsometry data of metallic thin films	112
5.5	Calculated absorption spectra for Si/metal superabsorbers	115
5.6	Calculated cross-section profile for the absorption for Si/AlCu super- absorbers	116
5.7	Calculated absorption maps for Si/metallic film superabsorbers	117
5.8	Calculated absorption spectra of thin film superabsorbers	118
5.9	Calculated cross-section profile for the absorption for Ge/AlCu su- perabsorbers	118
5.10	Calculated absorption maps for Ge/metallic film superabsorbers	119
5.11	Calculated cross-section profile for the absorption for GaAs/AlCu superabsorbers	119
5.12	Calculated absorption maps for GaAs/metallic film superabsorbers . .	120
5.13	Calculated absorption maps of Si/metal stacks for materials with dif- ferent refractive index	121
5.14	Calculated transmission spectra of Si/metal superabsorbers	122
5.15	Calculated transmission spectra of Si/AlCu alloyed thin film	122
5.16	Calculated absorption spectra of Si/CMOS-compatible metal thin film	123
5.17	Near-unity absorption sensitiveness to polarization and incident angle	124
5.18	Effect of surrounding media on metal alloyed-based superabsorbers . .	126
5.19	AFM image of the fabircated superabsorbers	127
5.20	Metal alloyed-based superabsorbers with zero transmission	127
5.21	Experimental demonstration of a-Si/AlCu superabsorbers	128
6.1	Illustration of thin-film all-solid-state batteries	137
6.2	Al negative electrode for all-solid-state batteries	143

6.3	Al-based batteries surface characterization	145
6.4	Electrochemical performance of thin-film all-solid-state batteries . . .	146
6.5	Cycling performance of Al, Al/Cu, Si/Cu anode	147
6.6	Electrochemical performance of thin-film all-solid-state battery with Si negative electrode	148
6.7	SEM image of Si-based thin-film batteries	149
6.8	Illustration of conductive atomic force microscopy	152
7.1	3D tomography of Li ions in all-solid-state batteries	155
7.2	Li depth profile of a pristine battery with Si anode	161
7.3	SEM images of solid-state batteries	161
7.4	Electrochemical performance of Si anode batteries	163
7.5	SEM images of Si anode batteries after ToF-SIMS measurements . . .	163
7.6	Depth profiles for Li in Si anode batteries at different state-of-charge	164
7.7	3D tomography of Li ion in Si anode batteries	166
7.8	Cycling performance of Si anode battery	167
7.9	Li distribution maps for the pristine battery	167
7.10	Li distribution maps for the charged battery	168
7.11	Li distribution maps for the cycled battery	169
7.12	Universality of 3D imaging method	170
7.13	Voltage profiles of Al anode battery	171
7.14	Li distribution maps for the cycled battery with Al anode	171
8.1	Building the library of optical properties for metallic alloy	180
A.1	Journal covers highlighting publications from this thesis	182

Chapter 1: Introduction to Energy Harvesting and Storage

1.1 Metals and Metallic Alloys in Photonics

As a branch of photonics, plasmonics is the study of light interaction with the free electrons in a metal. Different classes of materials have been explored for plasmonic applications including ceramics, intermetallics, semiconductors, and metals, depending on the desired wavelength range of operation [1–3]. In particular, noble metals such as Ag and Au have been extensively explored due to their localized surface plasmon resonances (LSPR) and surface plasmon polariton (SPP) waveguiding properties throughout the visible range [4, 5]. These phenomena are closely related to the metal dielectric function ϵ , which describes the electric polarizability of light (ϵ_1) and the absorption properties of the material (ϵ_2), where a small value of ϵ_2 is associated with a low-loss material. For Ag, Au, Cu and Al, these metals absorb light for different regions of the spectrum, which is related to their intrinsic dielectric functions (see Figure 1.1) and cannot be controlled [6].

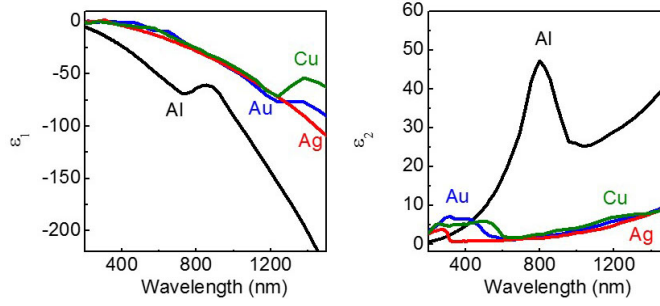


Figure 1.1: (Left) Real part (ϵ_1) and (Right) imaginary part (ϵ_2) of the dielectric functions for pure metals. Data from [7].

In the past decade, plasmonic materials have been widely used for energy harvesting, ranging from applications in solar cells to hot carrier devices. In the realm of photovoltaics (PV), it is well known that Si solar cells have limited light absorption due to their indirect band gap. Thus, plasmonic nanostructures have been implemented to trap light inside the semiconductor by promoting forward light scattering and, therefore, enhancing the light absorption within the solar cell [8]. In addition, heat generation for energy harvesting induced by light absorption for plasmonics nanostructures has potential applications in the field such as steam generation under room temperature [9]. For hot carrier devices, the heat generated by light absorption in metals is used to harvest energy [10]. While nanofabrication techniques have been successfully implemented to realize engineered metallic nanostructures and surfaces at the nanoscale with tunable optical response, the band energy and the dielectric function of metals are pre-defined. Here, we suggest alloying metals as an additional knob to access a class of metallic materials with optical properties not obtained otherwise [11].

Motivated by the rapid growth of information processing speed, researchers are constantly searching for ways of surpassing the tens of GHz limit of today's nanoelectronics. While photonics enables THz bandwidth data processing, it suffers from diffraction limitations [5], which restricts the size of the optical components, such as optical fibers, to approximately the wavelength of light. Plasmonics has the advantage of combining the high bandwidth from photonics with the nanoscale integration of nanoelectronics, by creating a sub-wavelength oscillation of the free-electron gas, a plasmon [12], which can transport information [13, 14]. However, one of the main challenges for effectively integrating metals into nanoscale devices is the fact that the metals have losses in the visible range of the spectrum, partially due to interband electronic transitions [1, 15]. Loss here is defined as the light absorbed by the metal, which is related to high ϵ_2 . One option to achieve low-loss plasmonic materials for CMOS compatible plasmonic devices in the near-infrared (NIR) wavelength range is to realize transparent conducting oxides (TCO), such as doped zinc oxide (ZnO) and indium tin oxide (ITO) [1, 16, 17]. Nitrides, such as TiN, are also a promising option for NIR applications. These materials are radiation tolerant and can be epitaxially grown onto substrates with cubic symmetry [2], which have the advantage of achieving ultra-smooth surfaces and thin-films without boundaries. Nevertheless, metals are still the most common materials under investigation for nanoplasmonic devices. Therefore, the control of the optical properties in metal thin films can have a significant impact on the development of metasurfaces and metamaterials in general [18, 19].

In systems where it is desired that the metal absorbs light there is a need

for large ϵ_2 , such as in hot carrier devices [10, 20, 21] and perfect absorbers [22–31]. Broadband perfect absorbers are devices that present near unity absorption over a large bandwidth of the spectrum. All incident radiation is absorbed independent of the frequency (transmission, reflection, and scattering events are negligible). These absorbers can find applications as thermal emitters, detectors or sensors, in infrared camouflage, etc. Nevertheless, despite all the progress in the field, it is still challenging to find a material/geometry that will not reflect or transmit light over an extremely broad range of the spectrum. Plasmon excitations in metallic nanostructures can be used to produce hot carriers and cause photoemission, a process where the energy of the electron is larger than the equivalent thermal excitation at ambient temperature. This phenomenon has been successfully implemented in a variety of situations, ranging from the photodissociation of H_2 and O_2 molecules to photodetector [32] and photovoltaic [33] devices. In all these applications the efficiency of the energy conversion processes involved are highly dependent on the Fermi level of the metal and, indirectly, its dielectric function.

In solar cells, the photons from the sun are absorbed by the semiconducting material, exciting electrons, which generate photocurrent. In the last ten years, there has been tremendous effort to improve the efficiency and decrease the cost of the solar cells technologies by: developing new materials for earth-abundant approaches [34, 35], new strategies for third generation concepts [36, 37], applying metallic nanostructures to enhance light absorption [38], among other methods. In particular, metallic nanostructures have been successfully implemented for concentrating and trapping light in PV devices because of the excitation of surface

plasmons. They can increase light absorption (Abs) in the semiconductor by essentially three mechanisms. First, by reducing reflection through increased forward scattering. Second, by increasing the local fields throughout the excitation of localized plasmon resonances, acting as antennas. Third, the incident light can be coupled into waveguide modes of the solar cell material (waveguiding), which can significantly increase the optical path length within the semiconductor [4, 8, 39–41]. These processes all heavily depend on the dielectric function ϵ of the metal, where $Abs \propto \epsilon_2 |E|^2$. An important figure-of-merit that describes the fraction of light scattered by the nanoparticle (NP) is defined by the scattering efficiency [42]:

$$\eta_{scat} = \frac{\sigma_{scat}}{\sigma_{scat} + \sigma_{abs}} \quad (1.1)$$

where

$$\sigma_{scat} = \frac{1}{6\pi} \left(\frac{2\pi}{\lambda} \right)^4 \left| 4\pi r^3 \frac{\epsilon_m - \epsilon_s}{\epsilon_m + 2\epsilon_s} \right|^2 \quad (1.2)$$

and

$$\sigma_{abs} = \left(\frac{2\pi}{\lambda} \right) Im \left[4\pi r^3 \frac{\epsilon_m - \epsilon_s}{\epsilon_m + 2\epsilon_s} \right] \quad (1.3)$$

Here, σ_{scat} and σ_{abs} are the scattering and absorption cross-sections for a spherical NP, respectively, λ is the wavelength of light, r is the radius of the NP, ϵ_m and ϵ_s are the dielectric functions (real + imaginary parts) of the metallic NP and the surrounding medium (solar cell), respectively. Note that the smaller σ_{abs} , the larger η_{scat} . Therefore, for PV applications, we want NPs with minimized σ_{abs} and maximum η_{scat} .

Extensive work has focused on using Ag sub-wavelength NPs to enhance light

absorption within PV devices due to its low loss throughout the visible spectrum (which requires small ϵ_2) [43]. These approaches have been shown to significantly increase the generated photocurrent within the solar cells; however, at short wavelengths Ag absorbs a large fraction of the light, which limits its application for PVs. Recent results have shown that Al can replace Ag when enhanced light absorption by the solar cells is required at short wavelength of the spectrum [44]. Nevertheless, Al oxidizes very easily and, depending on the volume of the NP, the plasmon resonance is sensitive to the intrinsic Al_2O_3 [45]. Despite all the progress achieved with pure Ag [40, 41, 43, 46–53], Au [54–59], Cu [4] and Al [44, 60], a material that leads to broadband enhancement in photocurrent is still missing.

For all the applications mentioned above, it is highly desired that one can predict and control the optical properties of the material to be synthesized. To overcome the limitations imposed by the pre-defined dielectric function of metals we are developing binary, ternary and quaternary mixtures of Ag, Au, Cu and Al to access materials with tunable optical responses not found in nature. Combinations of Ag, Au and Cu represent an ideal model system to investigate how alloying can affect the optical properties of the mixed material due to their similar structural properties (cubic crystalline structure and lattice constants differ by less than 11%) and energy bands (comparable energy gaps for transitions between the *s*- and *d*-bands at similar symmetry points) [15].

Al-based alloys are a promising material to realize CMOS-compatible and cheap building blocks with unique absorption characteristics. Recently, pure Al nanostructures has been investigated for plasmonics applications in the ultraviolet (UV)

and visible regions of the spectrum [32, 45, 61, 62]. While the binary nanostructures have been realized before [63–68], the understanding of how the chemical composition affects their optical response is still missing. ϵ of alloyed metals should not be approximated by the simple linear combination of the respective contribution from the individual metals because that would provide a physically non-realistic optical response for the new material, including negative absorption [65, 69]. Although ϵ for pure Ag, Au, Cu and Al has been extensively measured and calculated [6, 7, 70–72], there is very little work investigating its behavior as a function of the composition of the binary, ternary and quaternary alloys.

1.2 Metals in Li-ion Batteries

The ever-increasing demand for energy storage for intermittent power sources, such as solar and wind renewable power generation sources, for transportation (*e.g.* hybrid electric vehicles), and for mobile devices has stimulated intensive research on the pursuit of high energy and high power densities batteries [73–75]. Among these energy storage devices, rechargeable Li-ion batteries (LIBs) have become one of the most prominent candidates due to their low cost, high energy density and long lifetime [74]. The first rechargeable Li-ion battery was fabricated in the middle 1970s and was based on AlLi for the anode materials [76]. Since then, metals and metal alloys have been widely used for electrodes in LIBs. Particularly, Aluminum (Al), low-cost, earth-abundant, and non-toxic, is a potential candidate for battery anode because of its high specific energy (993 mAh/g) [77]. Batteries con-

sist of two electrodes, the anode and the cathode, connected by the electrolyte, a material with high ionic and low electronic conductivity. The two electrodes should have different equilibrium potentials, to yield a high voltage. During charging the electrons spontaneously flow from the cathode to the anode (with a more positive potential), resulting in the simultaneous transport of ions from the cathode to the anode, to keep the charge constant. An external circuit is used to store the electrical energy resulting from this electrochemical process. During the discharging step, the ions move back to the cathode, and now the electrons flow in the same direction, see Figure 1.2. In rechargeable (or secondary) batteries when the applied voltage exceeds the electrochemical potential of the cell, the flow of current reverses, thereby recharging the battery. However, usual rechargeable batteries contain a liquid electrolyte, resulting in severe design and safety constraints (*e.g.*, the battery system on the Boeing 787 Dreamliner airplanes caught on fire several times in 2012-2013). First, the electrolyte is usually a flammable liquid. Second, it prevents the miniaturization of the battery device itself, restricting its usage in ultra-compact electronics. To overcome these limitations, all-solid-state (rechargeable) batteries are being developed, encompassing a variety of materials and geometries.

For nearly all of today's applications, batteries with high energy density (energy stored/unit of mass) and power density (power stored/unit of mass) are being pursued. Mobile and small device applications require energy density around 250 Wh/Kg and power density of 500 W/Kg for fast charge/discharge [78, 79]. Here, we choose to investigate Li-ion batteries because Li has the highest electrochemical potential, delivers the largest energy density per weight, and is the lightest of all

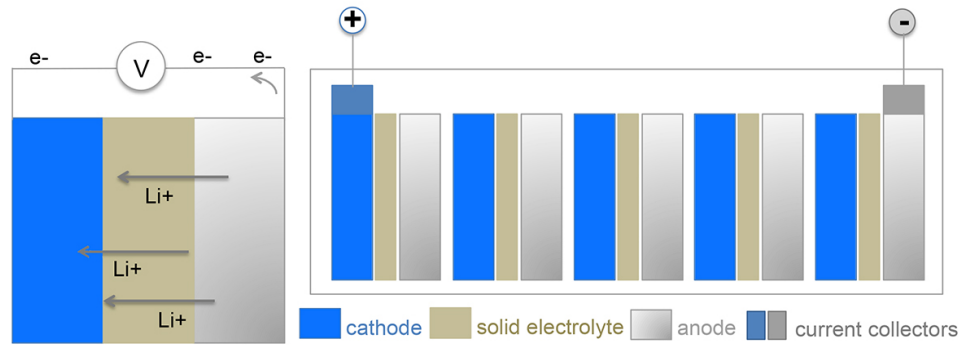


Figure 1.2: (Left) When a battery is used, the electrons are transported between the anode and the cathode to balance the charge transfer that takes place within the material (Li-ions diffusion). (Right) All-solid-state batteries enable compact devices due to smaller packaging, compared to liquid electrolyte designs.

metals [80,81] (at standard temperature and pressure).

One promising alternative to conventional liquid electrolyte cells are the all-solid-state Li-ion batteries, which provide: (i) high power density (> 200 kW/kg) [82], (ii) long cycle life, (iii) inherent safety, due to the absence of an organic liquid electrolyte that could cause leakage and fire, (iv) lightweight and possible compact packaging, and (v) flexibility in the types of materials that can be used as the electrodes [81,83–87]. The performance of all-solid-state batteries is usually described by their discharge capacity: the electric charge they can deliver at the rated voltage/unit of area or mass (Ah/cm^2 or Ah/g). This capacity depends on the current used to discharge the device, and is related to the C-rate: the discharge current divided by the theoretical current under which the battery would deliver its rated capacity in one hour. Another useful metric that defines how well a battery is performing is its Coulombic efficiency: the fraction of the electrical charge stored during

charging that is recoverable during discharge (Q_{out} / Q_{in}) [88, 89].

A primary advantage of all-solid-state batteries is the fact that small devices (nano- and micron-scale) can be achieved. The electrolyte of thin-film microbatteries is usually $< 1 \mu\text{m}$ in thickness, compared to $\sim 20 \mu\text{m}$ used in liquid-electrolyte cells [87]. These batteries are usually fabricated by the deposition of each active layer onto an inert substrate via different methods, depending on the materials chosen. In all-solid-state LIBs the ions diffuse from the cathode to the anode during the charging step by essentially three different types of reactions: (i) intercalation, (ii) conversion, or (iii) alloying. The intercalation mechanism dominates the commonly used graphite [81, 90–92] and $\text{Li}_4\text{Ti}_5\text{O}_{12}$ [93] anodes. The graphite reaction is described by: ($x\text{Li}^+ + \text{C}_6 + xe^- \rightleftharpoons \text{Li}_x\text{C}_6$). In these anode materials, this reaction is only reversible after a solid-electrolyte interface (SEI) is formed, which occurs during the first charging cycle of the battery, and ideally results in an ionically conductive and electrically insulating new layer. The conversion reaction commonly happens in anodes of the T_xA_y type, where T stands for the transition metals (Cu, Ni, V, Ti, Cr, Mn, Fe, Co), and A for anions (such as O, N, F, S, P). The conversion reaction is described by: $\text{T}_x\text{A}_y + (yn)\text{Li}^+ + xe^- \rightleftharpoons x\text{T} + y\text{Li}_n\text{A}$. Finally, alloying reactions can take place between Li and metals and semiconductors as: $\text{M} + x\text{Li}^+ + xe^- \rightleftharpoons \text{Li}_x\text{M}$, where M refers to Si, Ge, Sn, Al, and their alloys [78]. These materials present very high theoretical capacity, *e.g.* 4,200 mAh/g for Si, representing a very attractive class of anodes for high-energy density storage batteries. Nevertheless, the alloying reactions are usually accompanied by substantial volume changes of the anode during lithiation, which can lead to pulverization and the electrical isolation

of the active layer, limiting the lifetime of the device under repeated cycles.

Thin-film all-solid-state batteries have been successfully fabricated using a wide variety of materials for the anode, cathode, and electrolyte. The main advantage of the thin-film geometry is that one can leverage the well-established knowledge from microelectronics, including the materials physical deposition methods (sputtering, e-beam deposition, atomic layer deposition - ALD, chemical vapor deposition - CVD, pulsed laser deposition - PLD, ion-beam assisted deposition - IBAD, etc.) and photolithography to scale up the procedure involved in the fabrication of these devices. The simple fabrication routes resulted in a rapid improvement in the field, which used thin-film batteries as a model system to investigate the fundamental electrochemistry phenomena involved during the charging/discharging steps of the devices. Conversely, the key challenge of the thin-film design is the well-known volume expansion experienced by the anode during Li-ion insertion (charging) [94,95]. During cycling, the anode “breathes” due to Li-ions insertion/extraction upon charging/discharging, leading to the capacity fading. Thus, it is necessary to investigate the degradation mechanism by resolving where the Li-ions are in the batteries during cycling.

1.3 Scope and Contributions of this Thesis

This thesis explores novel metallic materials with physical and chemical properties not reachable by pure metals and sheds light into the applications ranging from photonics to energy storage. This work investigates the novel optical proper-

ties of alloys and the usage in fields including near-field optics and perfect absorbers. It also discloses the chemical and electrochemical properties of metallic materials and their applications in electrodes for all-solid-state LIBs.

Chapter 1 offers an introduction of utilizing metals and metallic alloys for energy harvesting and storage, and points out the suppressing need of discovering new metallic materials with novel optical properties for photonics and understanding the electrochemistry for energy storage.

Chapter 2 provides a detailed discussion of how the optical behavior of metal alloys can be modulated by changing their composition [11].

Chapter 3 discusses the fabrication and characterization of metal-alloyed nanostructures, including a comparison between experimental results and full-field simulations of light-matter interactions at the nanoscale [96].

Chapter 4 investigates the physical origin of the tunable optical properties of metallic alloys by measuring valence band spectra and calculated the band structure (manuscript under review).

Chapter 5 displays the implementation of a binary mixture of Cu and Al in energy harvesting devices, namely superabsorbers. The obtained Cu-Al/Si superabsorbers shows a maximum absorption $> 99\%$ [97].

Chapter 6 presents a detailed analysis of the surface/interface effects on the electrochemical performance of thin-film all-solid-state batteries by comparing Al and Si electrodes [77].

Chapter 7 focuses on building a 3D tomography of Li ions in solid-state energy storage devices and providing a universal imaging tool to study the correlation

between the ion migration and electrochemical performance (manuscript in preparation).

Chapter 8 gives the conclusion and outlook of this thesis, and part of the chapter is based on our Review [\[98\]](#).

Part I

Metallic Materials for Photonics

Chapter 2: Coin-age Metal Alloys for Plasmonics

Summary: The fixed optical properties of noble metals limit their use in photonic devices that operate at optical frequencies. To achieve metals with tunable optical response, we present noble metal alloyed thin-films formed by the binary mixture of Ag, Au, and Cu. As the permittivity (ϵ) of the alloys cannot be modeled as the linear combination of the pure metals, we combined transmission and reflection measurements of the alloyed thin films with a B-spline model that takes into account the Kromers-Kronig relation and experimentally determined the permittivity.

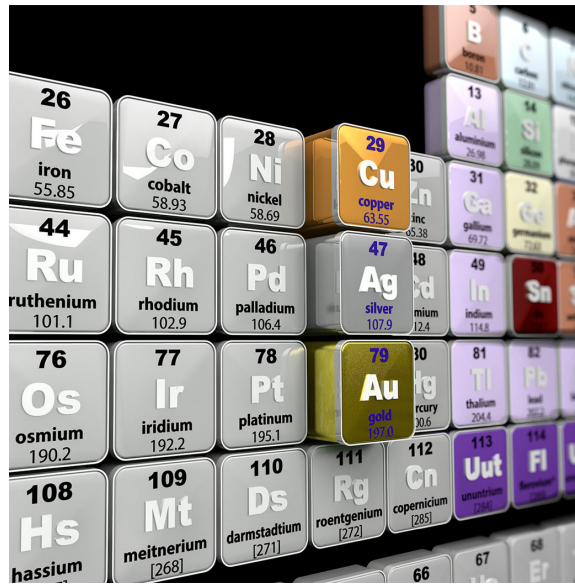


Figure 2.1: Illustration of noble metal alloys for plasmonics.

We found that in some cases a mixture can provide a material with higher surface plasmon polariton quality factor than the corresponding pure metals. We independently measured the surface plasmon polariton coupling angle for all alloys using the Kretschmann configuration and found excellent agreement between the two methods when determining ϵ . Our approach paves the way to implement metallic thin films and nanostructures with on-demand optical responses, overcoming the current limitation of the dielectric function of noble metals. This chapter is adapted from the following reference [11].

2.1 Introduction

If one had the option to arbitrarily modulate the dielectric function ($\epsilon = \epsilon_1 + i\epsilon_2$) of metallic structures, this would enable unprecedented control of the plasmon resonances in nanostructures and the surface plasmon propagation in thin films [5]. This, in turn, would allow for the development of a new class of metallic materials with tunable optical response for the fabrication of optoelectronic devices with unique characteristics, such as metasurfaces for tunable absorbers and optical filters [99–101], high-performance detectors [32, 102], and thin-film solar cells with enhanced performance [44, 46, 103], among others. Therefore, ways to control the dielectric function of a material are potentially very useful. In situations where one wants to minimize the material light absorption, such as in low-loss metamaterials with rationally designed composition and geometry or photonic devices where surface plasmons propagate on the surface of the metal, a small imaginary part of the dielectric function (ϵ_2) is required. Conversely, when one desires to use a metal as a light absorbing layer, for example, in hot carrier devices and perfect absorbers [30], a large value of ϵ_2 is essential.

Different classes of materials have been explored for plasmonics applications including ceramics, intermetallics, semiconductors, and metals, depending on the desired wavelength range of operation [1–3]. One promising option to achieve low-loss plasmonic materials in the NIR wavelength range is to realize TCO, such as ZnO and ITO [1]. Nitrides, such as TiN, are also a promising option for NIR applications [104]. These materials are radiation tolerant and can be epitaxially grown

onto substrates with cubic symmetry [2], which have the advantage of achieving ultrasmooth surfaces and thin films without boundaries. Noble metals such as Ag and Au have been extensively explored due to their LSPR and SPP waveguiding properties throughout the visible range [4,5]. However, despite all the research using noble metals, there are still considerable limitations related to their predetermined optical response.

One pathway to modulate the dielectric function of a metallic material is by alloying two metals [63–68,105]. Combinations of Ag, Au and Cu represent an ideal model system to investigate how alloying can affect the optical properties of the mixed material due to their similar structural properties (cubic crystalline structure and lattice constants differ by less than 11%) and energy bands (comparable energy gaps for transitions between the *s*- and *d*-bands at similar symmetry points) [15]. Nevertheless, ϵ of the alloyed metals cannot be approximated by the simple linear combination of the respective contribution from the individual metals because that would provide a physically nonrealistic optical response for the new material, including negative absorption [65,69]. Recently, it has been shown that the dielectric function of Ag-Au alloys can be predicted by using a multiparametric approach based on the Drude-Lorentz model [7], taking into account the band structure of each pure metal separately [106]. Although ϵ for pure Ag, Au and Cu has been extensively measured and calculated [6,7,70–72], there is very little work investigating the interpolated behavior of ϵ as a function of a range of compositions for the respective binary noble metal alloys.

Here we present the tuning of the optical properties of thin-film noble metal

mixtures by modification of their chemical composition, as a result of alloying. Thin films with a linear composition gradient formed by the binary mixture of Ag, Au, and Cu yielded alloys, an ideal model system to probe how the respective dielectric functions can be modulated by varying the content of each metal. Through the transmission and reflection measurements of the alloyed thin films and a B-spline model that takes into account the Kromers-Kronig relation, we experimentally determined the dielectric function of the noble metal alloys and found that, for the experimental conditions used here, in some cases a mixture of two metals can provide a material with higher SPP quality factor (Q_{SPP}) than the corresponding pure metals. We independently measured the SPP coupling angle for all alloys using the Kretschmann configuration and found excellent agreement between the two methods when determining ϵ . We provide a method for creating metallic thin films and nanostructures with tunable dielectric function, removing the predefined optical response constrain of pure noble metals.

2.2 Optical Properties of Metals and Metallic Alloys

Figure 2.2 shows the noble metal alloyed thin-film samples, formed by the binary linear combination of Ag, Au, and Cu, fabricated by cosputtering deposition. The evident color variation matches the composition gradient within the samples. In all cases a linear gradient in composition was obtained (Figure 2.3 and Table 2.1), as desired. All samples were very smooth (roughness < 1.7 nm, as measured by AFM; see Figures 2.4 and 2.5) [107, 108], and were composed of polycrystals, as

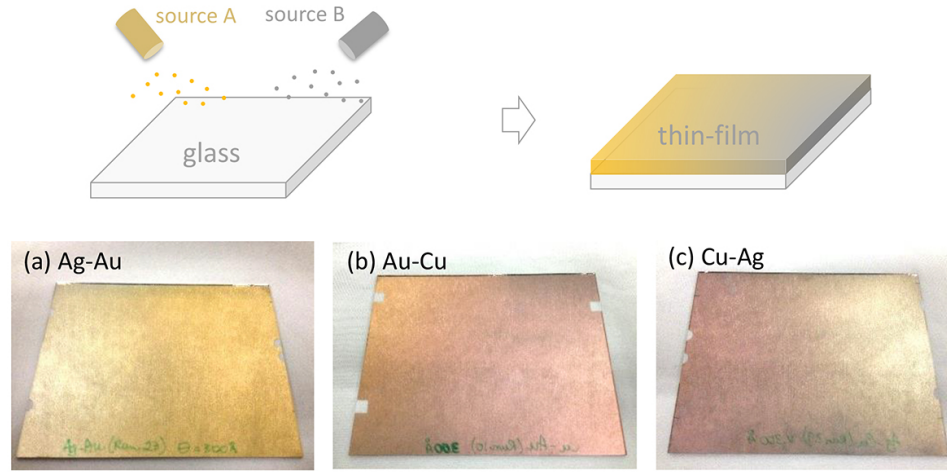


Figure 2.2: (top) Schematic of the cosputtering process used to achieve alloyed thin films with variable composition. (a-c) Photographs of three samples (nominal thickness = 30 nm in all cases) formed by binary combinations of Ag, Au, and Cu. Glass slides are $4 \times 6 \text{ in}^2$.

determined by X-ray diffraction measurements (see Figure 2.6). All thin films were approximately 30 nm in thickness and, therefore, suitable for both transmission and SPP prism coupling measurements. Note that the hazy texture observed in the photograph of the samples is actually from the cleanroom wipes under the samples and not from the roughness of the samples itself.

Figure 2.7 displays the transmission spectra for all alloyed samples, acquired at equally spaced locations across each sample, corresponding to a well-defined composition of the alloyed films. As expected, the pure metals (Ag, Au, and Cu) showed respective transmission peaks at 324, 499, and 581 nm, attesting to the high quality of the films, despite the fact that the metals were sputtered at low deposition rates [72]. In all cases, the samples were measured immediately after being removed from the sputtering chamber, minimizing air exposure and consequent oxidation. As

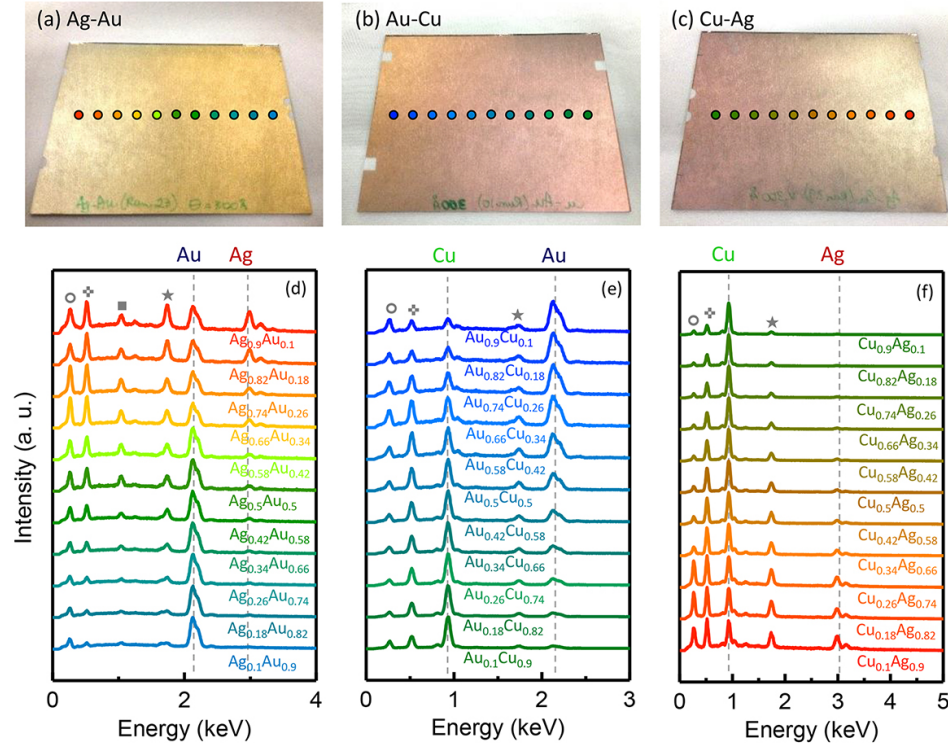


Figure 2.3: Photographs and EDS data obtained in plan view for (a,d) Ag-Au, (b,e) Au-Cu, and (c,f) Cu-Ag thin film samples. For EDS: acquisition area is $50 \times 50 \mu\text{m}^2$, acquisition time is 120 sec. The colored dots refer to the position where the EDS was acquired (out of scale for clarity). ○, ✚, ■, and ★ refer to C, O, Na and Si (from the glass slides), respectively.

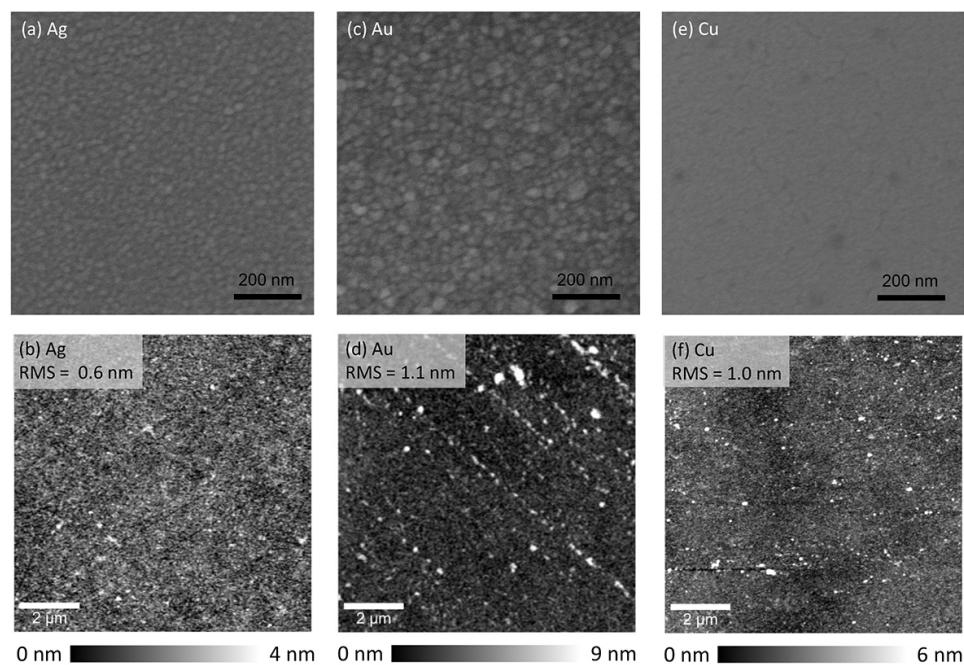


Figure 2.4: SEM plan-view images of (a) Ag, (c) Au, and (e) Cu thin films showing extremely small grains at the surface of each sample. AFM images of (b) Ag, (d) Au, and (f) Cu thin films and respective root-mean-square (RMS). The AFM measurements were performed in non-contact mode, using a Si probe (42 N/m) with 10 nm radius of curvature.

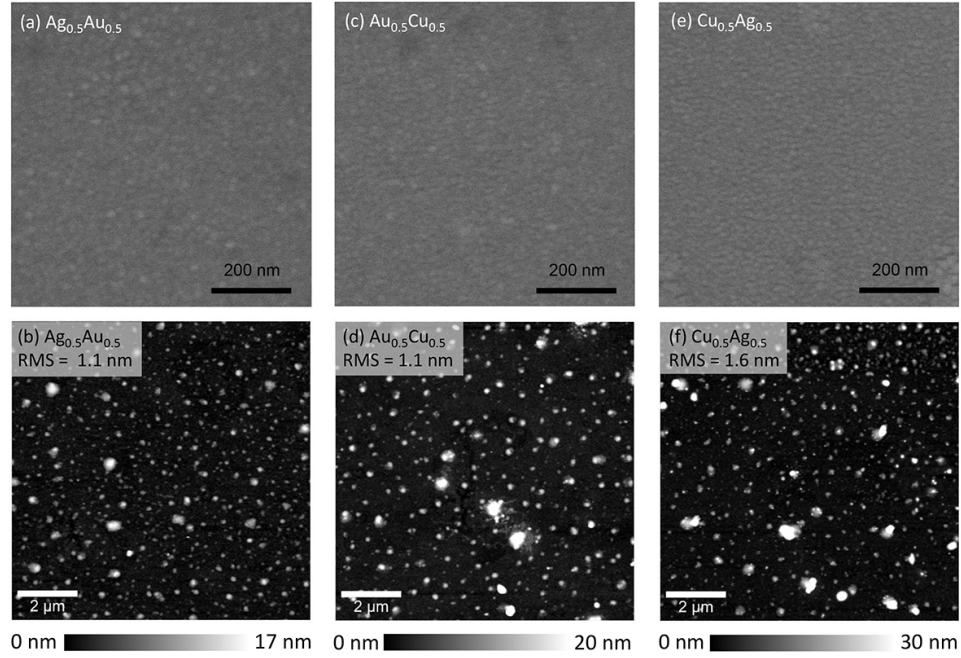


Figure 2.5: SEM plan-view images of (a) $\text{Ag}_{0.5}\text{Au}_{0.5}$, (c) $\text{Au}_{0.5}\text{Cu}_{0.5}$, and (e) $\text{Cu}_{0.5}\text{Ag}_{0.5}$ thin films. AFM images of (b) $\text{Ag}_{0.5}\text{Au}_{0.5}$, (d) $\text{Au}_{0.5}\text{Cu}_{0.5}$, and (f) $\text{Cu}_{0.5}\text{Ag}_{0.5}$ thin films and respective root-mean-square (RMS). The AFM measurements were performed in non-contact mode, using a Si probe (42 N/m) with 10 nm radius of curvature.

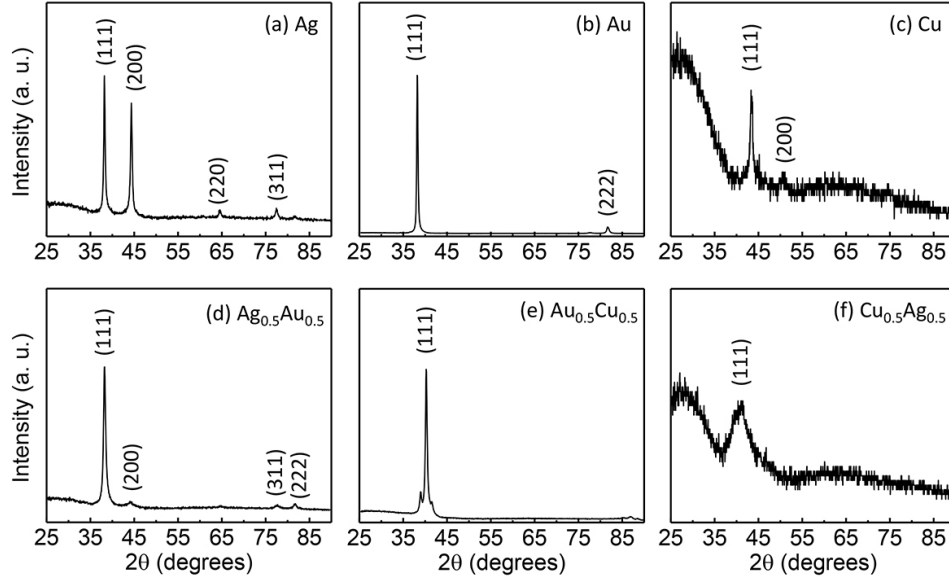


Figure 2.6: X-ray diffraction θ - 2θ measurements for (a,b,c) pure and (d,e,f) binary metal thin films. The right side shoulder peak on (e) refers to the presence of a small amount of AuCu(I) [109], (which can form even at room temperature [110]), while the left side peak is most likely due to the oxidation of Cu, as reported in [111]. For all measurements, the XRD signal was collected with 2D area detector, using a Cu K-alpha source. Five frames were collected for 10 minutes each, with a step size of 0.05 degrees. The intensity was then integrated and merged into a single diffraction. According to the international center for diffraction data (ICDD): Ag: PDF 01-087-0717, Au: PDF 01-071-4616, Cu: PDF 00-004-0836, Ag_{0.5}Au_{0.5}: PDF 01-071-9134, Au_{0.5}Cu_{0.5}: PDF 01-074-5367, Cu_{0.5}Ag_{0.5}: ref [112].

shown in Figure 2.7, the transmission measurements and are in very good agreement with the calculated transmission spectra. The $\text{Ag}_{0.5}\text{Au}_{0.5}$ alloy presents a broad peak at 454 nm, resulting from the contribution of both Ag and Au transmission signals, as shown in Figures 2.7a,b. In Figure 2.7c,d, all the $\text{Au}_x\text{Cu}_{1-x}$ alloys show one minor peak at ~ 350 nm and a major peak at 520-550 nm, resulting from both metals being present. The transmission spectra for the $\text{Cu}_x\text{Ag}_{1-x}$ sample (Figure 2.7e,f) present a continuous transition between the two pure metals, interpreted as a smooth change in relative intensity between the peaks of Cu and Ag. In particular, the region of the film corresponding to $\text{Cu}_{0.5}\text{Ag}_{0.5}$ shows a flat response over the 360 to 553 nm wavelength range. This behavior strongly indicates that the optical response of the alloys is not a result of the simple linear combination of the optical properties of the pure metals and requires a full investigation by an independent measurement technique, as will be discussed below.

In order to probe how the optical response of the noble metal alloys changes as a function of material composition we measured the dielectric function ϵ of the thin films by ellipsometry, combining transmission and reflection measurements [113]. To determine ϵ , we used a B-spline model to describe the optical response of the alloyed thin films, where the Kromers-Kronig relation was enforced at all times and the film thickness was also a variable parameter [114]. We verified the film thickness via cross-section TEM (see Figure 2.9) and found excellent agreement with the thickness value obtained by ellipsometry and the calculated optical response of the film. Figure 2.8 shows the measured real (ϵ_1) and imaginary (ϵ_2) parts of the dielectric function for all the noble alloyed thin films. The raw ellipsometry data

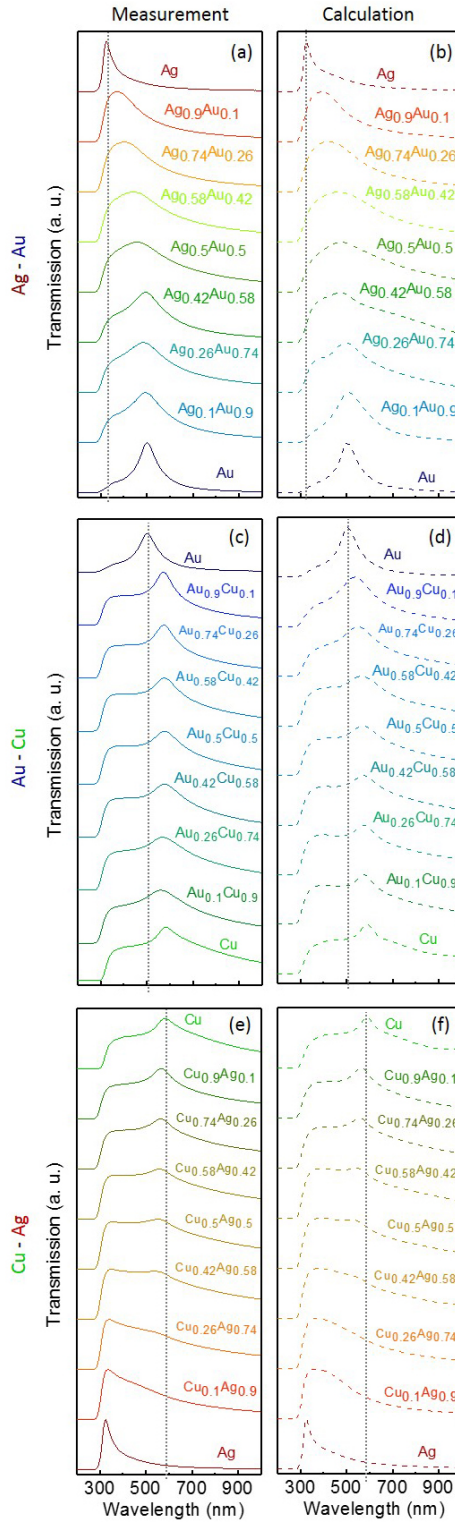


Figure 2.7: Normalized transmission measurements and calculations for 30 nm thick (a,b) Ag-Au, (c,d) Au-Cu, and (e,f) Cu-Ag thin films on glass showing the dependence of the peak shifts with the film composition. The dashed lines are guides for the eyes, showing the wavelength shift from one pure metal to another.

for all samples (Ψ and Δ as a function of wavelength) are presented in Figure 2.10. According to their phase diagram, Ag and Au form a solid solution over the whole concentration range [64], with a nearly constant lattice parameter [115]. As a result, the degree of disorder of the Ag-Au mixture is also constant for the different compositions, leading to a similar mean free path of conduction electrons for all alloys. This explains why ϵ_1 and ϵ_2 for Ag-Au do not vary drastically from 400 to 900 nm (see Figure 2.8a,b). ϵ_2 has a minimum value equal to 0.5 at ~ 700 nm, dominated by a disordered $\text{Ag}_{0.5}\text{Au}_{0.5}$ alloy [106]. The threshold of the interband transition, characterized by the sharp decrease of ϵ_2 , changes from about 300 nm (pure Ag) to 500 nm (pure Au) [106], as shown in Figure 2.8b.

For the Au-Cu alloy system, multiphases can also be obtained over certain composition ranges, such as $\text{Au}_{0.25}\text{Cu}_{0.75}$, $\text{Au}_{0.5}\text{Cu}_{0.5}$ and $\text{Au}_{0.25}\text{Cu}_{0.25}$ [116]. Here, the threshold of the interband transition shifted from 500 to 550 nm, from pure Au to pure Cu. From the spectrum of ϵ_2 (Figure 2.8e), the absence of peaks at 331 and 344 nm, corresponding to the ordered phase of $\text{Au}_{0.5}\text{Cu}_{0.5}$ and $\text{Au}_{0.26}\text{Cu}_{0.74}$ respectively, strongly indicates that these alloys form a disordered phase, as previously observed by Rivory [68]. Yet, De Silva recently reported that the overall effect of ordering on the dielectric function of Au-Cu is minor and can be easily masked by the scatter band resulting from variations of experimental measurements [109]. For instance, they observed that the Au-Cu porous thin film was composed by small grains, and that the resulting high density of boundaries enhanced light scattering and therefore the absorption by the thin-film layer, causing an overall increase of ϵ_2 . Conversely, they found that bulk Au-Cu was composed by large grains (almost free of defects

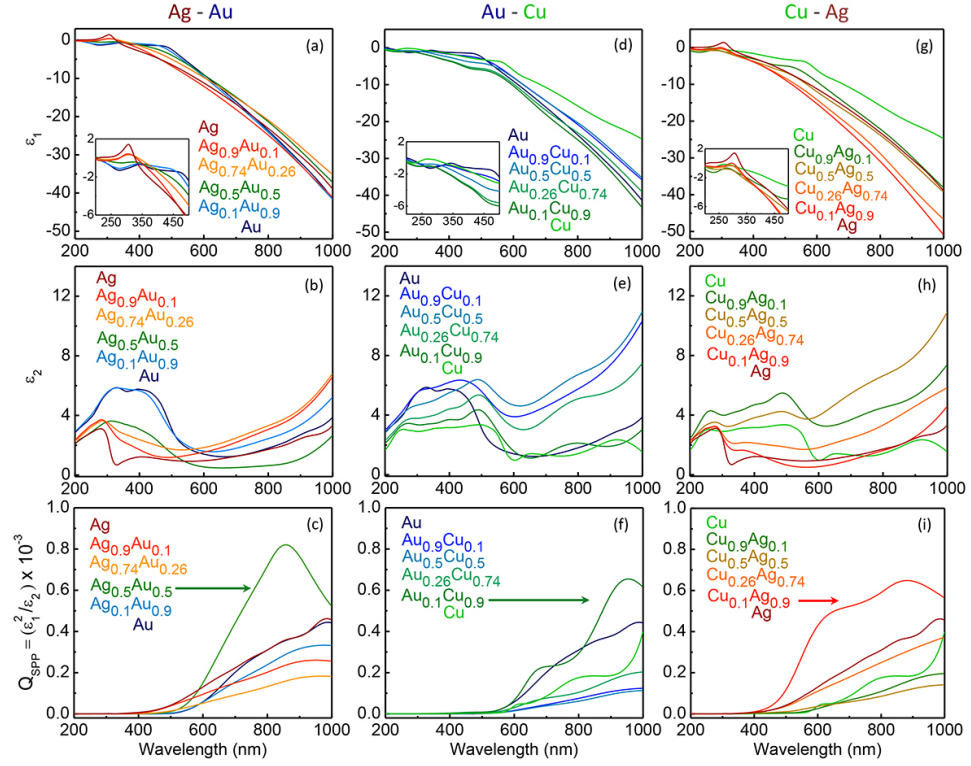


Figure 2.8: Measured dielectric function of noble metal alloyed thin films with variable composition. Real (ϵ_1) and imaginary (ϵ_2) parts of the dielectric function for metallic thin films with variable composition: (a, b) Ag-Au, (d, e) Au-Cu, and (g, h) Cu-Ag thin films. Insets: zoom-in of ϵ_1 as a function of wavelength for the ultraviolet and visible regions of the spectrum. Surface plasmon polariton quality factor Q_{SPP} for (c) Ag-Au, (f) Au-Cu, and (i) Cu-Ag thin film samples fabricated by sputtering, showing that metal alloyed thin films can outperform individual noble metals.

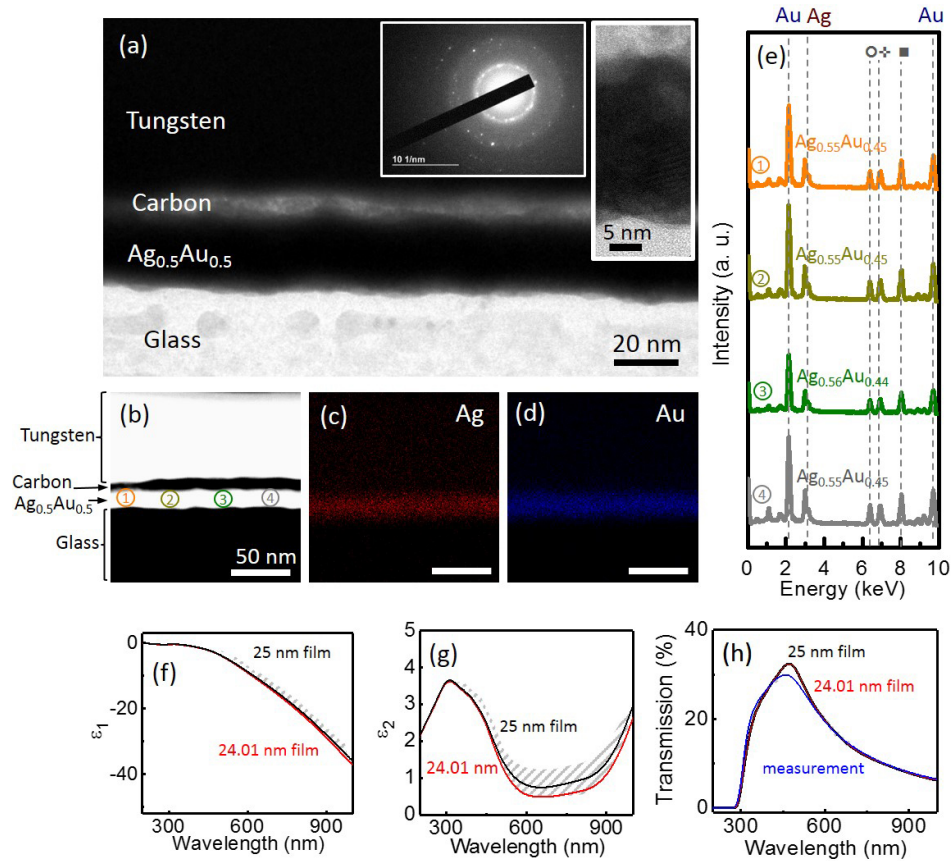


Figure 2.9: (a) Bright field TEM image showing 25 ± 2 nm thick $\text{Ag}_{0.5}\text{Au}_{0.5}$ thin film. Insets show high-resolution TEM image and electron diffraction pattern of polycrystalline film. (b) HAADF image and EDS maps of (c) Ag and (d) Au showing uniform distribution of metals within the thin film. (e) Four representative EDS point measurements [as marked in (b)] showing average composition of $\text{Ag}_{0.55}\text{Au}_{0.45}$. Carbon (C) and tungsten (W) were sequentially deposited on top of the $\text{Ag}_{0.5}\text{Au}_{0.5}$ sample for layer protection during Ga^+ milling process by FIB (\circ , \oplus , and \blacksquare refer to W, N, and Cu from the TEM grid, respectively). (f) Real and (g) imaginary parts of the dielectric function of $\text{Ag}_{0.5}\text{Au}_{0.5}$ thin film for the film thickness values obtained by ellipsometry (24.01 nm, red line) and while fixing the film thickness at 25 ± 2 nm (black line, as determined by TEM). (h) Measured (blue line) and the calculated transmission spectra for $\text{Ag}_{0.5}\text{Au}_{0.5}$ film using layer thickness equal to 25 nm (as determined by TEM, black line) and equal to 24 nm (as determined by ellipsometry, red line). In (f-h) the grey region refers to the variation in ϵ resulting from the variation in thickness determined by TEM (± 2 nm).

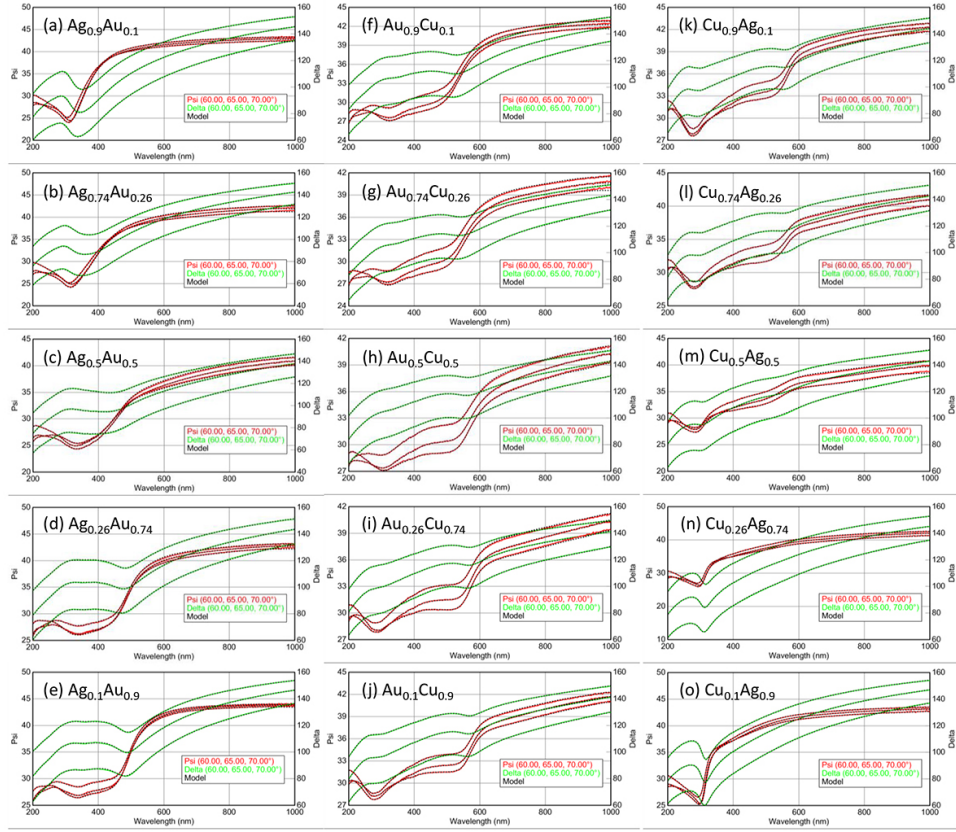


Figure 2.10: Ellipsometry data (reflection + transmission), Psi (Ψ , red) and Delta (Δ , green), for five different compositions of (a-e) Ag_xAu_{1-x} , (f-j) Au_xCu_{1-x} , and (k-o) Cu_xAg_{1-x} , obtained at three different angles (60, 65, and 70 degrees), including the fit (dashed black line, model) using a B-Spline function and enforcing K-K relation. Here, the thickness of the film was also a variable, as indicated in Tables 2.2-2.4.

and thus light scattering centers). Note that the experimental conditions of the film deposition can substantially affect the size of the grains constituting a film and the density of interfaces, which explains the different values of ϵ_2 reported by different groups. Postdeposition annealing treatments and the deposition rate are known for influencing the final structural characteristics and optical response of metal thin films [72].

Conversely, the phase diagram of the $\text{Cu}_x\text{Ag}_{1-x}$ system has a broad miscibility gap for the whole composition range for room temperature deposition as Cu-Ag does not form a solid solution [116], unless a liquid or vapor quenching is applied after deposition [117]. The spectra of ϵ_2 for the Cu-Ag alloys (Figure 2.8h) show two distinct absorption edges in the visible range, at 300 and 530 nm, indicating the independent contribution from both metals [117]. For this system, the d -bands from the pure metals slightly overlap, and the electron density of states from each metal contributes separately to the dielectric function of Cu-Ag alloys [68]. Our measurements show that both ϵ_1 and ϵ_2 can assume values higher and lower than what would be wrongly predicted by the composition-weighted linear combination, see Figures 2.11-2.13.

We compare the measured/modeled dielectric function of the noble metal alloys investigated here with the linear combination of its pure metals (see Figures 2.11-2.13). For these calculated values of ϵ_1 and ϵ_2 (dashed lines) we use the linear combination measured quantities of the pure metals as the input. Our measurements (solid lines) show that both ϵ_1 and ϵ_2 can assume values higher and lower than what would be wrongly predicted by the composition-weighted linear combination. As

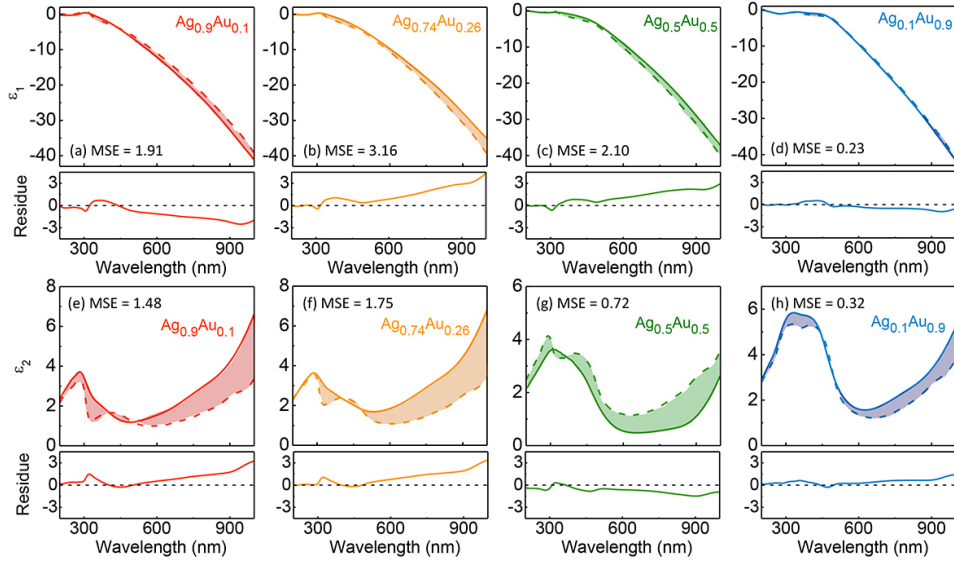


Figure 2.11: (a-d) Real and (e-h) imaginary parts of the dielectric function experimentally obtained (solid line) and calculated using the linear combination (dashed line) of pure Ag and Au. The colored areas highlight the difference between the measured and the calculated values of ϵ_1 and ϵ_2 . The residue graphs show the difference between these data.

demonstrated by the high discrepancy between the calculated and measured data, the simple linear combination weighted by the fraction composition of each metal is insufficient to describe the optical response of the alloys in a realistic manner. Here, the residue R refers to the difference between the measured and the calculated values of ϵ_1 and ϵ_2 , respectively, as a function of wavelength, as described below:

$$R = \epsilon_{1,2}^{measured} - \epsilon_{1,2}^{calculated} \quad (2.1)$$

Here, the mean squared error (MSE) is the average of the square of the difference between the measured and the calculated values of ϵ_1 and ϵ_2 , respectively, as described below:

$$MSE = \frac{1}{n} \sum_{i=1}^n |\epsilon_{(i)1,2}^{measured} - \epsilon_{(i)1,2}^{calculated}| \quad (2.2)$$

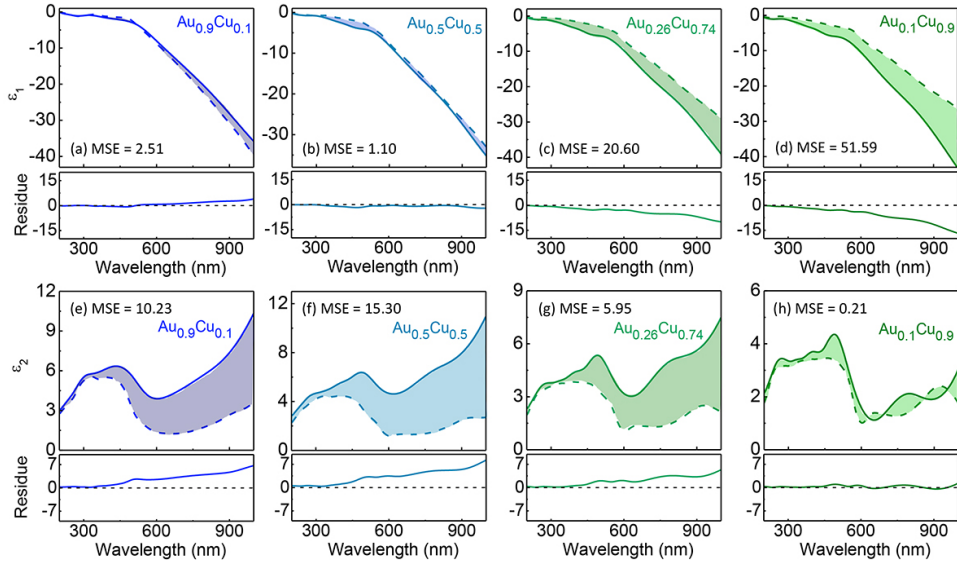


Figure 2.12: (a-d) Real and (e-h) imaginary parts of the dielectric function experimentally obtained (solid line) and calculated using the linear combination (dashed line) of pure Au and Cu. The colored areas highlight the difference between the measured and the calculated values of ϵ_1 and ϵ_2 . The residue graphs show the difference between these data.

The quality factor of the surface plasmon polariton of the alloys, defined as [20]

$$Q_{SPP} = (\epsilon_1^2/\epsilon_2) \times 10^{-3} \quad (2.3)$$

was calculated from the measurements of ϵ , and we found that certain compositions ($\text{Ag}_{0.5}\text{Au}_{0.5}$, $\text{Au}_{0.1}\text{Cu}_{0.9}$, and $\text{Cu}_{0.1}\text{Ag}_{0.9}$) present higher values of Q_{SPP} than the respective pure metals (see Figures 2.8c,f,i, 2.14, and 2.15). For instance, the disordered mixture of $\text{Ag}_{0.5}\text{Au}_{0.5}$ showed the largest values of Q_{SPP} for wavelength > 600 nm, with maximum value at ~ 830 nm, suggesting that a higher electron mean free path in the mixture of Ag and Au can provide a less absorptive material for NIR applications. Note that in all cases higher wavelength-dependent values of Q_{SPP} could be obtained by optimizing the deposition rate of each metal [72]; nonetheless,

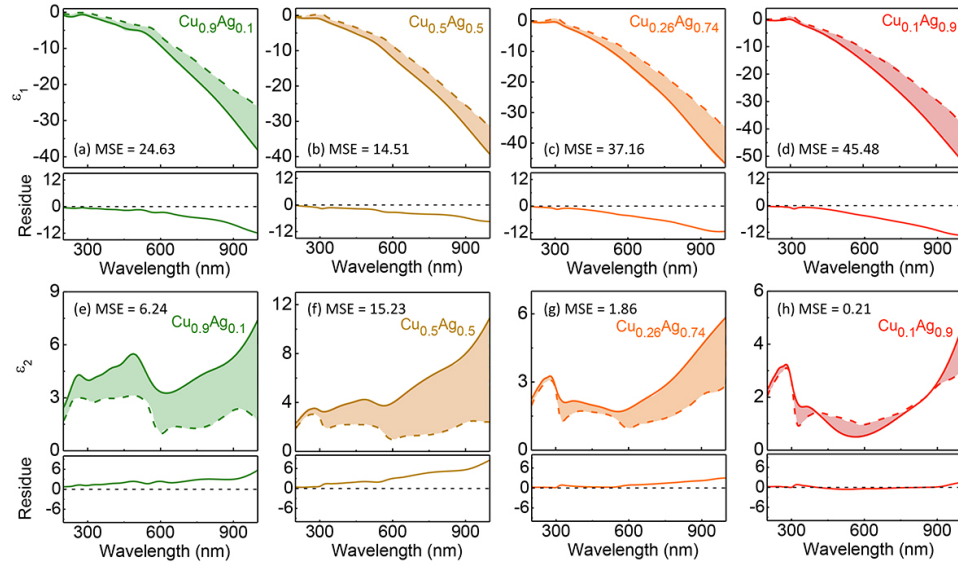


Figure 2.13: (a-d) Real and (e-h) imaginary parts of the dielectric function experimentally obtained (solid line) and calculated using the linear combination (dashed line) of pure Cu and Ag. The colored areas highlight the difference between the measured and the calculated values of ϵ_1 and ϵ_2 . The residue graphs show the difference between these data.

the trend of the relative improvement in Q_{SPP} as a function of the alloy composition should be the same, independent of the deposition rate used. Similarly, selected compositions of the binary-alloyed films exhibit higher propagation length of surface plasmon polariton than the pure metals (see Figure 2.15). To validate the ellispometry model, we determined scatter bands for transmission taking into account a film thickness variation of ± 3 nm (see Figure 2.16), finding that the originally obtained thicknesses are the best match to our experimental data.

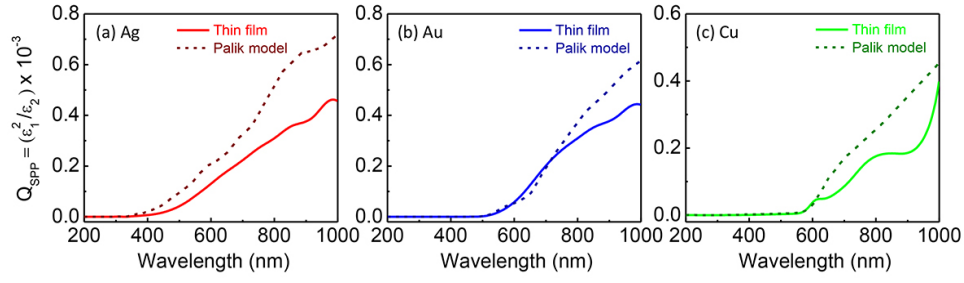


Figure 2.14: Quality factor Q_{SPP} for pure (a) Ag, (b) Au, and (c) Cu thin-film samples fabricated by sputtering (solid lines) and the respective values obtained by the Palik model of the dielectric functions (dashed lines) [7]. Note that the lower values of Q_{SPP} obtained for the fabricated thin films is simply due to the low deposition rate used here (2-5 Å/sec), which can be improved by implementing rates $> 10, 30,$ and 150 Å/sec for Au, Cu and Ag, respectively [72].

2.3 Surface Plasmon Polariton Coupling Angle

Measurements

The SPP angle-dependent reflection spectra for all samples were measured using the Kretschmann configuration [118], using a 637 nm diode laser p -polarized with 3.6 mW. The metal alloy thin film was placed on a rotational stage with step size of 0.1° and attached to an equilateral CaF_2 prism with $n_{prism} = 1.433$ using an index matching fluid for effective light coupling (see Methods for experimental details). As shown in Figure 2.17, in all cases (under identical experimental conditions) a well-defined minimum of the reflected laser power was observed, confirming the excitation of surface plasmons. Figures 2.17a,b displays the measured and calculated reflection spectra for the Ag-Au alloys, where the $\text{Ag}_{0.5}\text{Au}_{0.5}$ thin film presents a fairly shallow dip. Here, the small discrepancy between the measured and

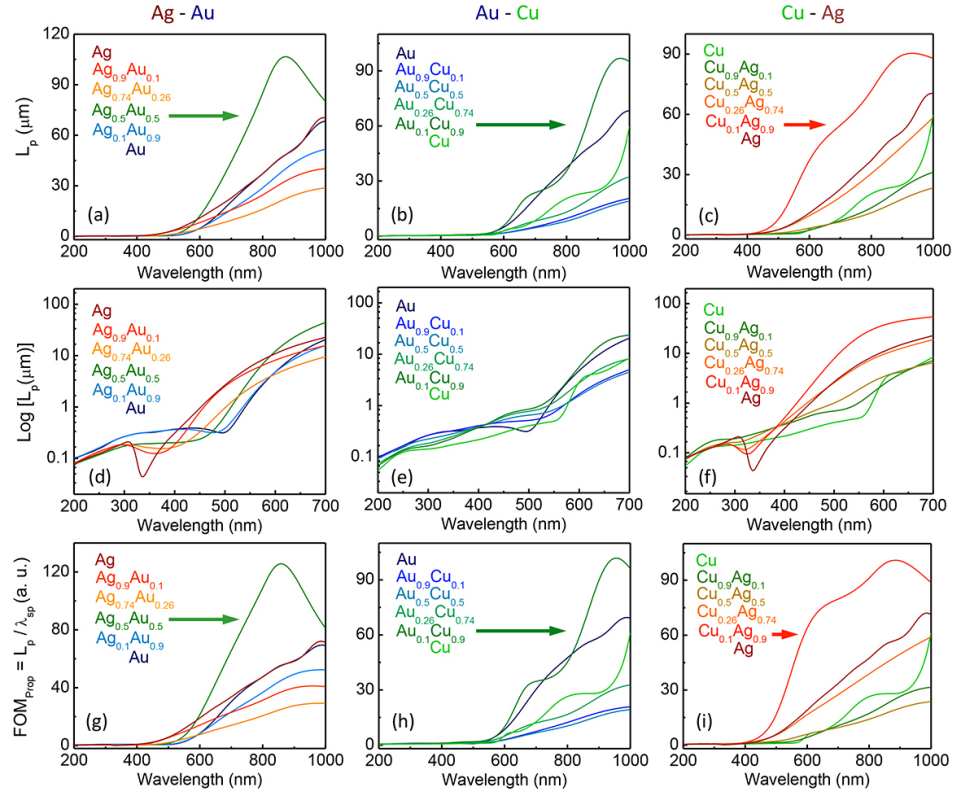


Figure 2.15: The propagation length (L_p) of the surface plasmon polariton for (a,d) Ag-Au, (b,e) Au-Cu, and (c,f) Cu-Ag, L_p is shown in log scale to highlight the details at short wavelength. FOM_{prop} for (g) Ag-Au, (h) Au-Cu, and (i) Cu-Ag thin films.

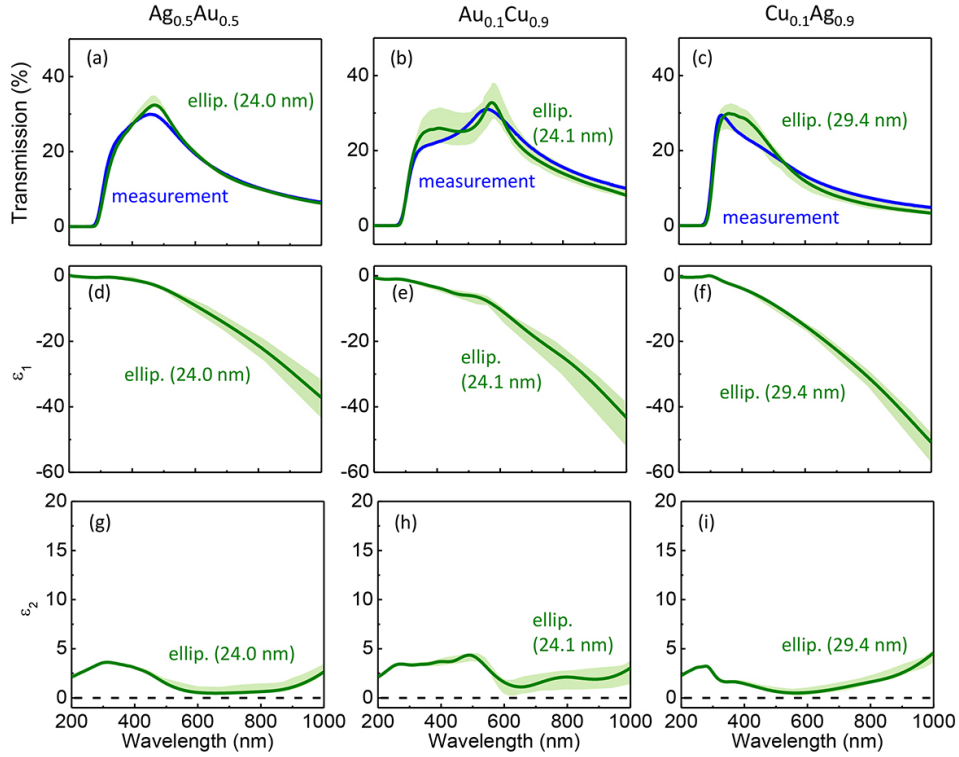


Figure 2.16: Measured (blue line) and calculated (green line) transmission spectra for (a) $\text{Ag}_{0.5}\text{Au}_{0.5}$, (b) $\text{Au}_{0.1}\text{Cu}_{0.9}$, and (c) $\text{Cu}_{0.1}\text{Ag}_{0.9}$, where the thickness of each thin-film sample, as determined by ellipsometry, is indicated in the respective figures. The light green region refers to the calculated transmission for film thickness ± 3 nm, showing that the originally obtained thicknesses are the best match to our experimental data. This comparison demonstrates that the measured transmission data is in very good agreement with the calculated one, using the film thickness as determined by ellipsometry as the input on the calculations. The small variations between the measured and calculated data could be due to light scattering effects caused by the grain interfaces in the samples. Real and imaginary parts of the dielectric function of (d,g) $\text{Ag}_{0.5}\text{Au}_{0.5}$, (e,h) $\text{Au}_{0.1}\text{Cu}_{0.9}$, and (f,i) $\text{Cu}_{0.1}\text{Ag}_{0.9}$ thin films, where the light green region refers to the film optical response assuming thickness variation of ± 3 nm in all cases.

calculated angle is primarily due to: (i) the uncertainty of the initial angle on the rotation stage ($< 0.1^\circ$), (ii) the presence of contaminants at the film surface, and (iii) the temperature variation of the sample during the SPP measurements [118–120]. The minimum reflection point for the $\text{Au}_x\text{Cu}_{1-x}$ alloys varies nonlinearly and non-monotonically as a function of the composition (see Figures 2.17c,d), in agreement with the ellipsometry measurements presented in Figure 2.8c. According to Figures 2.17e,f, despite the fact that the Cu-based alloys are formed by ~ 50 nm grains (see Figure 2.5 for AFM images) and that an extremely thin layer of Cu_2O is present (Figure 2.18), the SPP coupling angle is very well defined.

We find excellent agreement between the values of ϵ_1 measured by SPP coupling measurements and those obtained from ellipsometry, see Figures 2.19, two independent techniques. The real part of the dielectric function for each pure metal and the alloys (ϵ_1^m) were calculated using the following equation:

$$(n_{prism} \cdot \sin \theta_{spp})^2 = \frac{\epsilon_1^m \times \epsilon_1^{air}}{\epsilon_1^m + \epsilon_1^{air}} \quad (2.4)$$

where n_{prism} is the refractive index of the prism, θ_{spp} is the angle of minimum reflection in the SPP measurement, and ϵ_1^{air} ($= 1$) is the real part of the dielectric function for air. From the measured value of the internal angle corresponding to the minimum of the reflected power and the refractive index of the prism, we calculated ϵ_1 at 637 nm, and compared the results with the independent values obtained by the ellipsometry measurements on the same region of the samples. As confirmed by the latter, both Ag-Au and Au-Cu alloys only have one absorption edge over the visible range of the spectrum. As a result, the d bands strongly overlap in these

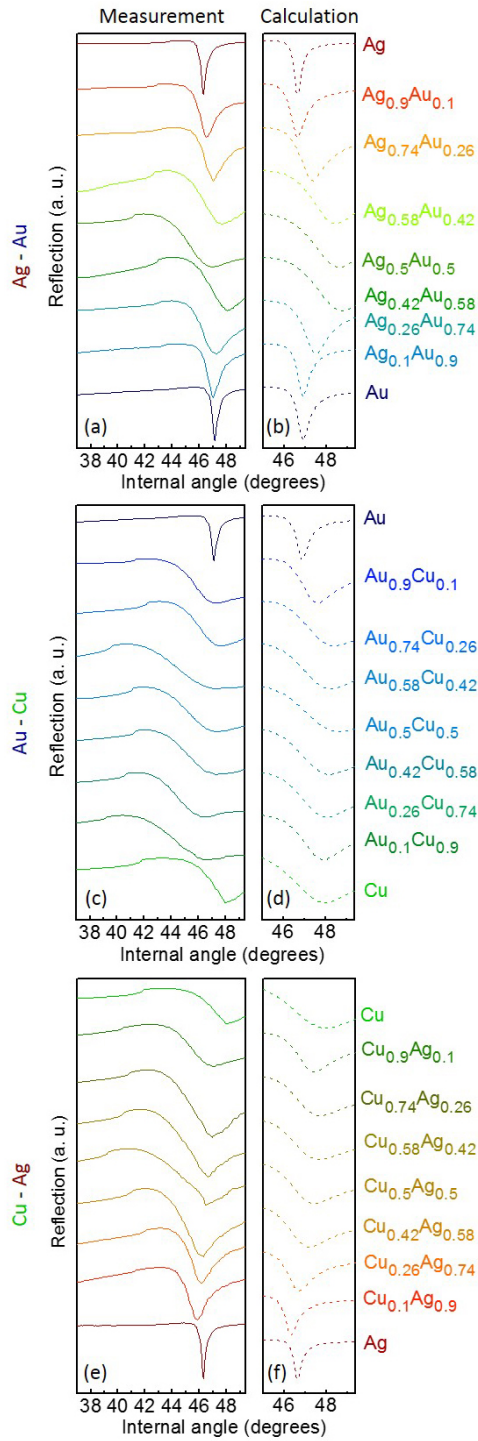


Figure 2.17: Measurements and calculations showing surface plasmon polariton excitation as a function of internal angle in a Kretschmann configuration for (a,b) Ag-Au, (c,d) Au-Cu, and (e,f) Cu-Ag thin films. Light source: 637 nm diode laser p -polarized with 3.6 mW.

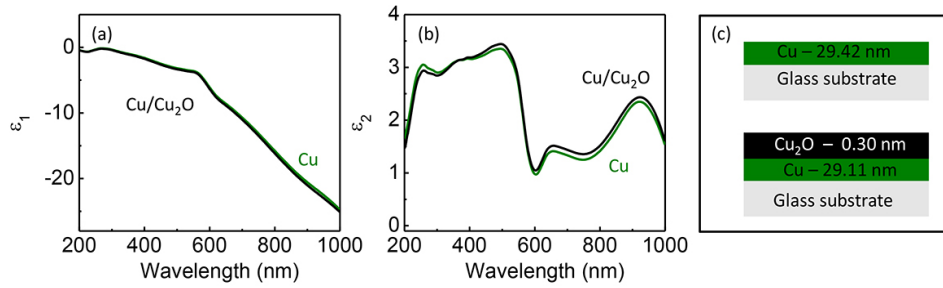


Figure 2.18: Comparison between the dielectric function of Cu thin film with and without considering a thin Cu₂O top layer. (a) ϵ_1 , (b) ϵ_2 , and (c) schematic of the thin-film stacks modeled by the B-spline function in each case. For both fit: $\text{MSE} < 2.3$.

systems, and the value of ϵ_1 varies as a function of the composition and the amount of overlap. For $\text{Au}_x\text{Cu}_{1-x}$, ϵ_1 decays almost monotonically as a function of x (see Figure 2.19b). The disordered AuCu and AuCu₃ alloys lead to constant values of ϵ_1 (for $0.48 < x < 0.52$ and $0.71 < x < 0.77$), corroborating Rivory's hypothesis that ordering/disordering can strongly affect the optical properties of these binary mixtures [68]. The dielectric function of very thin films is extremely sensitive to the film overall thickness, the grains size and the density of interfaces. As a result of the metal deposition conditions implemented, one can obtain thin films with a strong porous character and a high density of interfaces, which can result in additional light scattering centers and enhanced light absorption by the thin film [109]. In these situations, the effect of ordering on the dielectric function is indeed negligible, as the characteristic atomic disordering causes a flattening of the double peak usually observed in ordered Au-Cu (at ~ 330 nm for $\text{Au}_{0.5}\text{Cu}_{0.5}$, according to ref. [68]). The optical response of the Cu-Ag system is substantially different: the alloys do not

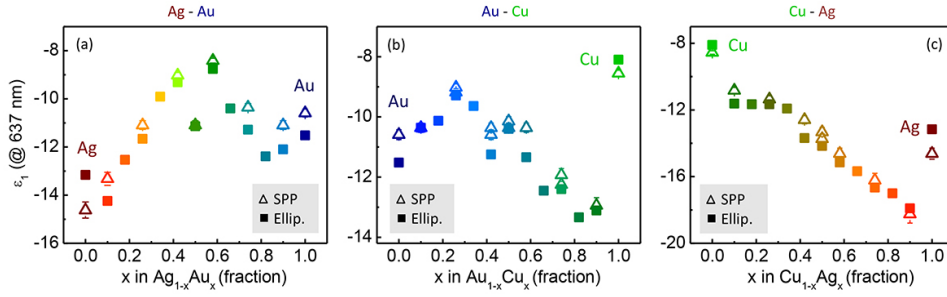


Figure 2.19: Real part of dielectric function ϵ_1 (at 637 nm) as a function of film composition, as determined from surface plasmon polariton excitation (SPP, open triangles) and ellipsometry (Ellip., solid squares) experiments for (a) Ag-Au, (b) Au-Cu, and (c) Cu-Ag thin films.

form a solid solution and the value of ϵ_1 decreases almost linearly from pure Cu to pure Ag [68, 117], see Figure 2.19c. In this mixture, the d bands do not overlap strongly.

Here we show evidence that the chemical composition of noble metal alloys can affect the dielectric function of the material in nontrivial ways, modifying both the strength of the polarization induced by an external electric field and the losses in the material due to absorption. Finding the precise physical origin of the nonmonotonic behavior of ϵ_1 for the alloys would require determining their band diagram and the density of states by X-ray photoelectron spectroscopy measurements as a function of their composition, which is beyond the scope of this work. Nevertheless, we have shown that depending on the wavelength range of interest, the alloying of noble metals yields materials with controlled optical response, such as enhanced surface plasmon propagation length or minimized optical loss.

2.4 Experimental Methods

2.4.1 Sample Fabrication

All metal-alloyed thin films were fabricated by the cosputtering deposition of single metals, at room temperature, with deposition rates between 2.0 and 5.0 Å/s, onto 4×6 in² glass slides. The glass slides were cleaned with acetone, isopropanol, and DI water, and then dried with N₂, prior the physical deposition. The pure metal sources (with purity > 99.99%) were placed 180° from each other, allowing for a linear gradient in composition for each alloyed sample.

2.4.2 Transmission and Reflection Measurements

The transmission and reflection measurements were performed using a variable-angle spectroscopic ellipsometer with a white-light source over a wavelength range of 200-1000 nm. Incident angles (with respect to normal incidence) of 60, 65, and 70° were used for reflection and 0° for transmission measurements. The ellipsometry data were analyzed using a B-spline model to determine the dielectric function for each pure metal and for the alloys, by assuming a two-layer vacuum-metal model to extract the dielectric function of each pure metal and each alloy.

2.4.3 Modeling the Dielectric Function

The dielectric function of each pure metal and the corresponding binary alloys was parametrized by B-spline function $S(x)$ defined as [114],

$$S(x) = \sum_{i=1}^n c_i B_i^k(x) \quad (2.5)$$

where c_i is the B-spline coefficient and B_i^k is a B-spline basis function defined as,

$$B_i^0(x) = \begin{pmatrix} 1, & t_i < x < t_{i+1} \\ 0, & \textit{otherwise} \end{pmatrix} \quad (2.6)$$

$$B_i^k(x) = \left(\frac{x - t_i}{t_{i+k} - t_i} \right) B_i^{k-1}(x) + \left(\frac{t_{i+k+1} - x}{t_{i+k+1} - t_{i+1}} \right) B_i^{k-1}(x) \quad (2.7)$$

where t_i is the perpendicular distance of the knot (where each polynomial segment in the curve is connected) from the y axis, and k is the degree of the B-spline. The Kramers-Kronig (K-K) relation was enforced during fitting to ensure the physical meaning of the results, as the imaginary part of the dielectric function ϵ_2 is parametrized by the B-spline curve as a function of wavelength λ as,

$$\epsilon_2(\lambda) = \sum_{i=1}^n c_i B_i^k(\lambda) \quad (2.8)$$

Then, ϵ_1 was calculated using the Kramers-Kronig relation. Therefore, each reflection measurement was appended to the corresponding transmission spectrum and was fitted using the Kramers-Kronig enforced B-spline model simultaneously. Roughness was neglected during fitting of the measured data due to the minimal root-mean-squared (RMS) surface roughness of the thin films (< 1.7 nm), as determined by AFM. In all cases, the root mean square error (RMSE) of the fits was $<$

4.3, and the thickness of the film was also a variable. For Cu-rich alloys, the thin layer of oxide was neglected in the modeling, as it was found that the thickness of oxide layer is negligible (< 0.55 nm) by considering this extra oxide layer using our model.

2.4.4 SPP Coupling Experiments

The SPP measurements were performed using the Kretschmann geometry, using a 637 nm diode laser with 3.6 mW incident power. A half-wave plate was used to select p -polarized light. The metal alloy thin film was attached to an equilateral CaF_2 prism with $n_{prism} = 1.433$ using an index-matching fluid. The sample was placed on a rotational stage that allowed us to change the angle of incidence, and the reflected light was detected using a silicon photodiode. The power of the reflected light was recorded at each external angle with a step size of 0.1° . The internal angle was calculated from the external one by considering the equilateral geometric shape and the dielectric function of the prism. The internal angle, corresponding to the reflection power minimum, was designated as θ_{spp} . The following equation was used to calculate the real part of the dielectric function for each pure metal and the alloys (ϵ_1^m) [118].

$$(n_{prism} \cdot \sin \theta_{spp})^2 = \frac{\epsilon_1^m \times 1}{\epsilon_1^m + 1} \quad (2.9)$$

2.4.5 Transmission and SPP Calculations

The calculated transmission spectra and SPP spectra (R_{spp}) were obtained using the equations below [5],

$$Transmission = \frac{T_{012,p} + T_{012,s}}{2} \quad (2.10)$$

$$T_{012,p} = \frac{t_{01,p}t_{12,p}exp(-i\beta)}{1 + r_{01,p}r_{12,p}exp(-i\beta)} \quad (2.11)$$

$$T_{012,s} = \frac{t_{01,s}t_{12,s}exp(-i\beta)}{1 + r_{01,s}r_{12,s}exp(-i\beta)} \quad (2.12)$$

$$R_{spp} = \frac{r_{01,p}r_{12,p}exp(-i2\beta)}{1 + r_{01,p}r_{12,p}exp(-i2\beta)} \quad (2.13)$$

where the transmission coefficient for p - ($t_{jk,p}$) and s -polarized ($t_{jk,s}$) light are defined as,

$$t_{jk,p} = \frac{2N_j \cos \Theta_j}{N_k \cos \Theta_j + N_j \cos \Theta_k} \quad (2.14)$$

$$t_{jk,s} = \frac{2N_j \cos \Theta_j}{N_j \cos \Theta_j + N_k \cos \Theta_k} \quad (2.15)$$

and the reflection coefficient for p - ($r_{jk,p}$) and s -polarized ($r_{jk,s}$) light are defined as,

$$r_{jk,p} = \frac{N_k \cos \Theta_j - N_j \cos \Theta_k}{N_k \cos \Theta_j + N_j \cos \Theta_k} \quad (2.16)$$

$$r_{jk,s} = \frac{N_j \cos \Theta_j - N_k \cos \Theta_k}{N_j \cos \Theta_j + N_k \cos \Theta_k} \quad (2.17)$$

where $j, k=0, 1, 2$. And the phase variation of the light is,

$$\beta = \frac{2\pi d}{\lambda} (N_1^2 - N_0^2 \sin^2 \Theta_0)^{1/2} \quad (2.18)$$

where d is the thickness of the film, as determined by ellipsometry. In the transmission calculations, 0 stands for air, 1 for the metal thin-film layer, and 2 for the glass substrate. In the SPP calculations, 0 refers to the prism, 1 to the metal thin-film

layer, and 2 to air, N is the experimentally determined complex refractive index of each layer, θ is the incidence angle of light (with wavelength λ) with respect to the normal direction.

Table 2.1: Chemical composition for (top) Ag-Au, (middle) Au-Cu, and (bottom) Cu-Ag thin-film samples, obtained from EDS data shown in Figure 2.3.

Nominal film composition	EDS atomic ratio of Ag (%)	EDS atomic ratio of Au (%)
$\text{Ag}_{0.9}\text{Au}_{0.1}$	86	14
$\text{Ag}_{0.82}\text{Au}_{0.18}$	80	20
$\text{Ag}_{0.74}\text{Au}_{0.26}$	71	29
$\text{Ag}_{0.66}\text{Au}_{0.34}$	65	35
$\text{Ag}_{0.58}\text{Au}_{0.42}$	58	42
$\text{Ag}_{0.5}\text{Au}_{0.5}$	52	48
$\text{Ag}_{0.42}\text{Au}_{0.58}$	42	58
$\text{Ag}_{0.34}\text{Au}_{0.66}$	35	65
$\text{Ag}_{0.26}\text{Au}_{0.74}$	27	73
$\text{Ag}_{0.18}\text{Au}_{0.82}$	14	86
$\text{Ag}_{0.1}\text{Au}_{0.9}$	8	92

Nominal film composition	EDS atomic ratio of Au (%)	EDS atomic ratio of Cu (%)
$\text{Au}_{0.9}\text{Cu}_{0.1}$	86	14
$\text{Au}_{0.82}\text{Cu}_{0.18}$	83	17
$\text{Au}_{0.74}\text{Cu}_{0.26}$	76	24
$\text{Au}_{0.66}\text{Cu}_{0.34}$	68	32
$\text{Au}_{0.58}\text{Cu}_{0.42}$	60	40
$\text{Au}_{0.5}\text{Cu}_{0.5}$	48	52
$\text{Au}_{0.42}\text{Cu}_{0.58}$	37	63
$\text{Au}_{0.34}\text{Cu}_{0.66}$	28	72
$\text{Au}_{0.26}\text{Cu}_{0.74}$	22	78
$\text{Au}_{0.18}\text{Cu}_{0.82}$	16	84
$\text{Au}_{0.1}\text{Cu}_{0.9}$	10	90

Nominal film composition	EDS atomic ratio of Cu (%)	EDS atomic ratio of Ag (%)
$\text{Cu}_{0.9}\text{Ag}_{0.1}$	91	9
$\text{Cu}_{0.82}\text{Ag}_{0.18}$	83	17
$\text{Cu}_{0.74}\text{Ag}_{0.26}$	78	22
$\text{Cu}_{0.66}\text{Ag}_{0.34}$	66	34
$\text{Cu}_{0.58}\text{Ag}_{0.42}$	54	46
$\text{Cu}_{0.5}\text{Ag}_{0.5}$	47	53
$\text{Cu}_{0.42}\text{Ag}_{0.58}$	42	58
$\text{Cu}_{0.34}\text{Ag}_{0.66}$	35	65
$\text{Cu}_{0.26}\text{Ag}_{0.74}$	28	72
$\text{Cu}_{0.18}\text{Ag}_{0.82}$	21	79
$\text{Cu}_{0.1}\text{Ag}_{0.9}$	14	86

Table 2.2: Optical properties for $\text{Ag}_{1-x}\text{Au}_x$ alloyed thin films from measurements and calculations. θ^{SPP} corresponds to the angle of minimum reflection in the SPP measurement, and ϵ_1^{SPP} is calculated using equation shown before. The error for ϵ_1^{SPP} is calculated via error propagation, considering the step size (0.1 degrees) of the angle in each SPP measurement. ϵ_1^{Ellip} is the real part of the dielectric function, as determined from ellipsometry measurements, and θ^{Ellip} is calculated. The thickness of the alloyed thin film was a variable parameter on the fitting of the experimental data, as displayed in column six. RMSE is the root mean square error from the ellipsometry fitting, as shown in Fig. 2.10.

Film composition	θ^{SPP} at 637 nm (degrees) measured	ϵ_1^{SPP} at 637 nm calculated	ϵ_1^{Ellip} at 637 nm measured	θ^{Ellip} at 637 nm (degrees) calculated	Thickness (nm)	RMSE
Ag	46.30	-14.64±0.34	-13.16	46.55	54.32	2.750
$\text{Ag}_{0.9}\text{Au}_{0.1}$	46.52	-13.32±0.27	-14.24	46.36	39.12	2.280
$\text{Ag}_{0.82}\text{Au}_{0.18}$	—	—	-12.53	46.67	38.25	2.451
$\text{Ag}_{0.74}\text{Au}_{0.26}$	47.02	-11.09±0.18	-11.66	46.87	37.34	2.877
$\text{Ag}_{0.66}\text{Au}_{0.34}$	—	—	-9.91	47.39	36.21	3.380
$\text{Ag}_{0.58}\text{Au}_{0.42}$	47.74	-9.01±0.12	-9.31	47.62	35.72	3.951
$\text{Ag}_{0.5}\text{Au}_{0.5}$	47.02	-11.09±0.18	-11.13	47.01	24.01	3.367
$\text{Ag}_{0.42}\text{Au}_{0.58}$	48.03	-8.40±0.10	-8.76	47.85	35.50	4.269
$\text{Ag}_{0.34}\text{Au}_{0.66}$	—	—	-10.40	47.22	34.86	2.713
$\text{Ag}_{0.26}\text{Au}_{0.74}$	47.24	-10.35±0.16	-11.28	46.97	36.19	3.304
$\text{Ag}_{0.18}\text{Au}_{0.82}$	—	—	-12.39	46.70	37.55	2.508
$\text{Ag}_{0.1}\text{Au}_{0.9}$	47.02	-11.09±0.18	-12.10	46.77	52.79	1.747
Au	47.17	-10.57±0.161	-11.52	46.91	69.21	1.836

Table 2.3: Optical properties for $\text{Au}_{1-x}\text{Cu}_x$ alloyed thin films from measurements and calculations. θ^{SPP} corresponds to the angle of minimum reflection in the SPP measurement, and ϵ_1^{SPP} is calculated using equation shown before. The error for ϵ_1^{SPP} is calculated via error propagation, considering the step size (0.1 degrees) of the angle in each SPP measurement. ϵ_1^{Ellip} is the real part of the dielectric function, as determined from ellipsometry measurements, and θ^{Ellip} is calculated. The thickness of the alloyed thin film was a variable parameter on the fitting of the experimental data, as displayed in column six. RMSE is the root mean square error from the ellipsometry fitting, as shown in Fig. 2.10.

Film composition	θ^{SPP} at 637 nm (degrees) measured	ϵ_1^{SPP} at 637 nm calculated	ϵ_1^{Ellip} at 637 nm measured	θ^{Ellip} at 637 nm (degrees) calculated	Thickness (nm)	RMSE
Au	47.17	-10.57±0.16	-11.52	46.91	69.21	1.836
$\text{Au}_{0.9}\text{Cu}_{0.1}$	47.24	-10.35±0.16	-10.36	47.24	52.29	2.464
$\text{Au}_{0.82}\text{Cu}_{0.18}$	—	—	-10.13	47.31	44.61	2.459
$\text{Au}_{0.74}\text{Cu}_{0.26}$	47.67, 47.74	-9.18±0.12, -9.01±0.11	-9.29	47.62	44.71	2.624
$\text{Au}_{0.66}\text{Cu}_{0.34}$	—	—	-9.64	47.49	38.20	2.385
$\text{Au}_{0.58}\text{Cu}_{0.42}$	47.17	-10.57±0.16	-11.25	46.98	27.91	2.674
$\text{Au}_{0.5}\text{Cu}_{0.5}$	47.24, 47.31	-10.35±0.16, -10.14±0.15	-10.40	47.22	18.32	1.942
$\text{Au}_{0.42}\text{Cu}_{0.58}$	47.24	-10.35±0.16	-11.34	46.95	27.31	2.915
$\text{Au}_{0.34}\text{Cu}_{0.66}$	—	—	-12.45	46.69	25.49	2.000
$\text{Au}_{0.26}\text{Cu}_{0.74}$	46.74	-12.23±0.23	-12.40	46.70	25.15	2.192
$\text{Au}_{0.18}\text{Cu}_{0.82}$	—	—	-13.34	46.52	24.15	2.372
$\text{Au}_{0.1}\text{Cu}_{0.9}$	46.59	-12.95±0.26	-13.11	46.56	24.05	2.588
Cu	47.95	-8.56±0.10	-8.10	48.19	29.42	2.222

Table 2.4: Optical properties for $\text{Cu}_{1-x}\text{Ag}_x$ alloyed thin films from measurements and calculations. θ^{SPP} corresponds to the angle of minimum reflection in the SPP measurement, and ϵ_1^{SPP} is calculated using equation shown before. The error for ϵ_1^{SPP} is calculated via error propagation, considering the step size (0.1 degrees) of the angle in each SPP measurement. ϵ_1^{Ellip} is the real part of the dielectric function, as determined from ellipsometry measurements, and θ^{Ellip} is calculated. The thickness of the alloyed thin film was a variable parameter on the fitting of the experimental data, as displayed in column six. RMSE is the root mean square error from the ellipsometry fitting, as shown in Fig. 2.10.

Film composition	θ^{SPP} at 637 nm (degrees) measured	ϵ_1^{SPP} at 637 nm calculated	ϵ_1^{Ellip} at 637 nm measured	θ^{Ellip} at 637 nm (degrees) calculated	Thickness (nm)	RMSE
Cu	47.95	-8.56±0.10	-8.10	48.19	29.42	2.222
$\text{Cu}_{0.9}\text{Ag}_{0.1}$	47.09	-10.84±0.17	-11.62	46.88	37.49	1.960
$\text{Cu}_{0.82}\text{Ag}_{0.18}$	—	—	-11.66	46.87	34.79	1.940
$\text{Cu}_{0.74}\text{Ag}_{0.26}$	46.95	-11.35±0.19	-11.66	46.87	32.52	1.977
$\text{Cu}_{0.66}\text{Ag}_{0.34}$	—	—	-11.92	46.81	30.05	2.202
$\text{Cu}_{0.58}\text{Ag}_{0.42}$	46.66	-12.60±0.24	-13.69	46.45	25.01	2.433
$\text{Cu}_{0.5}\text{Ag}_{0.5}$	46.52, 46.45	-13.32±0.27, -13.71±0.29	-14.16	46.37	25.92	3.145
$\text{Cu}_{0.42}\text{Ag}_{0.58}$	46.30	-14.64±0.34	-15.15	46.23	25.13	3.370
$\text{Cu}_{0.34}\text{Ag}_{0.66}$	—	—	-15.68	46.15	25.64	3.186
$\text{Cu}_{0.26}\text{Ag}_{0.74}$	46.09	-16.20±0.42	-16.66	46.04	26.65	3.467
$\text{Cu}_{0.18}\text{Ag}_{0.82}$	—	—	-17.00	46.00	28.40	3.059
$\text{Cu}_{0.1}\text{Ag}_{0.9}$	45.87	-18.27±0.54	-17.90	45.91	29.42	3.063
Ag	46.30	-14.64±0.34	-13.16	46.55	54.32	2.750

2.5 Conclusions

In conclusion, we have shown the correlation between the chemical composition of noble metal alloyed thin films and their respective dielectric functions, which can be tailored by tuning the composition fraction between the two metals. Our ellipsometry and SPP excitation measurements are in excellent agreement, demonstrating the validity of the ellipsometry analysis. Moreover, we have shown that for the deposition conditions implemented here the Q_{SPP} of some alloyed mixtures is higher than the respective pure metals, allowing for the rational design of metallic nanostructures with a high control of their optical response in the visible range of the spectrum. Our approach to fabricate a new class of metallic materials with optical response on-demand can be applied to metasurfaces and metamaterials, which commonly requires low optical loss materials, hot carrier devices, whose performance is very sensitive to the light absorption within the active layer, and other optical and optoelectronic devices.

Chapter 3: Optical Properties of Fully Alloyed Ag-Au Nanostructures

Summary: Combining metallic elements with different compositions at the nanoscale to obtain fully alloyed nanostructures can pave the way for an optical-electronic platform with fine-tunable response over a very broad range of the electromagnetic spectrum, from the UV to the IR. While the optical properties of pure metallic nanostructures have been extensively investigated by varying their size, shape and distribution, their intrinsic dielectric function still limits its application.

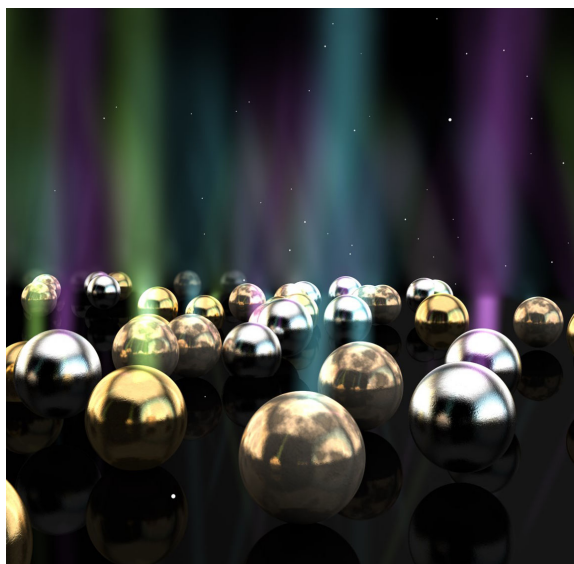


Figure 3.1: Illustration of fully alloyed nanostructures.

Here, we implement the dewetting of metallic thin films to produce fully alloyed $\text{Ag}_x\text{Au}_{1-x}$ nanoparticles (NPs), and show how their chemical composition affects the optical response of the self-assembled arrays. To show how alloying can be used to tune the LSPR of metallic nanostructure systems, we analyze the near-field optical properties of alloyed $\text{Ag}_{0.5}\text{Au}_{0.5}$ NPs by combining spectrally dependent near-field scanning optical microscopy (NSOM) with full-field simulations of the light-matter interactions. Our results demonstrate the potential of realizing alloyed nanostructures by a scalable method with engineered optical properties for applications ranging from nanophotonics to sensing. This chapter is adapted from the following reference [96].

3.1 Introduction

LSPR is the confinement of the collective oscillation of the electron charges in metallic nanostructures, causing a pronounced electric field enhancement at their surface and high optical absorption. This property has been widely explored for Ag and Au NPs in the fields of nanophotonics [5, 121], energy harvesting [103, 122], molecular detection [123], biomedical therapeutics [124], and catalysis [125]. The possibility of fabricating pure metallic NPs with controllable size and shape enables the modulation of the LSPR from the UV to the IR regions of the electromagnetic spectrum [12, 126, 127]. However, the pressing need for providing on-demand plasmonic properties for nanophotonic applications still remains due to the fact that the optical response of pure metals, such as Ag and Au, is dominated by their intrinsic dielectric function. Alloying of these noble metals has been applied to tune the material dielectric function, where the LSPR can be modulated progressively from the UV (pure Ag) to the NIR (pure Au) [11, 128–130]. Thus, metallic nanostructures composed of Ag-Au can enable the rational design of building blocks for different applications, such as metamaterials [131, 132], hot carrier devices [10], light absorption improvement in photovoltaics [133, 134], colored glasses [135], displays [136, 137], and catalysis [138].

To date, different fabrication techniques have been successfully utilized to realize $\text{Ag}_x\text{Au}_{1-x}$ alloyed NPs. They can be formed by colloidal synthesis via the reduction of precursors containing metals in solution [65, 139], and by the sequential pulsed laser deposition of Ag and Au targets [106, 140], which can yield large amounts

of NPs with narrow size distribution. However, the overall size of the NPs cannot be varied beyond 150 nm [141]. Alternatively, nanolithographic methods enable full control of NPs size, shape and distribution [128]. Nevertheless, this technique is constrained to specific applications due to its high cost and very limited scalability. The dewetting of metallic thin films has also been used to fabricate pure [135, 142–144] and alloyed [133] metal NPs. In this simple and effective fabrication route, a very thin layer of metal (< 50 nm) is initially deposited onto a substrate. Then, when the thin-film sample is annealed under a controlled environment (oxygen free), surface diffusion takes place and results in the formation of nanostructures to minimize the energy of the system [125, 145–147]. This method has been particularly useful for optoelectronic devices, where these metallic NPs act as light scattering centers that ultimately increase light absorption within the semiconductor [4, 122].

In this work, we fabricate fully alloyed $\text{Ag}_x\text{Au}_{1-x}$ NPs with controlled chemical composition by dewetting thin films and characterize their optical response at the macro- and nano-scale. Surprisingly, we find that the NPs' distribution heavily depends on the thin-film chemical composition, irrespective of the original film thickness. Simultaneously, we measure a shift of the LSPR due to the NPs' composition variation, which defines their optical response. We map the elemental distribution of Ag and Au and confirm that the NPs are fully alloyed, forming a solid solution at the nanoscale. To further illustrate how the chemical composition affects the material optical response, we perform a detailed analysis of the optical characteristics of fully alloyed $\text{Ag}_{0.5}\text{Au}_{0.5}$ nanostructures in the visible range of the spectrum. For that, we combine spectrally dependent NSOM measurements and finite-difference

time-domain (FDTD) simulations to locally resolve the optical response of individual NPs. Our results of the near-field light-matter interactions for $\text{Ag}_{0.5}\text{Au}_{0.5}$ nanostructures reveal an electric field enhancement of 30 times in the visible range of the spectrum under the NPs and in its vicinity. The NSOM measurements are in excellent agreement with our full-field simulations.

3.2 Morphology, Transmission and Chemical Analysis

We fabricate alloyed NPs by the co-sputtering deposition of Ag and Au on ITO/glass substrates, followed by a thermal annealing treatment under a controlled environment. Upon annealing, the thin film suffers substantial surface diffusion, and the NPs are formed to minimize the nanoparticles + substrate system's energy (the surface and edge energy terms of the enthalpy) [146]. A sequence of scanning electron microscopy (SEM) plan-view images of the NP samples are presented in Figure 3.2a to e, with its corresponding diameter statistics. NPs are obtained across the whole composition range, from pure Ag to pure Au, using the same annealing condition. Table 3.1 and Figure 3.3 show that Hemispherical NPs are formed in all alloyed samples containing Ag, with average base diameter equal to 53 ± 29 nm, 141 ± 70 nm, 253 ± 62 nm, and 184 ± 70 nm for Ag, $\text{Ag}_{0.75}\text{Au}_{0.25}$, $\text{Ag}_{0.5}\text{Au}_{0.5}$, and $\text{Ag}_{0.25}\text{Au}_{0.75}$, respectively. The spatial distribution (density) of the particles corresponds to a coverage area of 7%, 12%, 19%, and 19%, respectively. The samples with $\text{Ag}_{0.75}\text{Au}_{0.25}$ and $\text{Ag}_{0.25}\text{Au}_{0.75}$ present NPs with similar average size, but different distribution (see Figure 3.2). In particular, we observe a large population

of extremely small NPs on sample $\text{Ag}_{0.75}\text{Au}_{0.25}$, most likely resulting from incomplete ripening process, a common phenomenon defined by the coarsening of larger particles at the expense of smaller ones, resulting from their chemical potential minimization [148]. Conversely, the pure Au NPs are faceted, with an average major and minor axis equal to 441 ± 176 nm and 368 ± 148 nm, where the substrate area covered by the NPs is 9% [108]. The relatively strong cohesion between Ag and ITO leads to the formation of small particles, whereas the weak cohesion between Au and ITO gives rise to larger, faceted particles [145]. Therefore, the combination of such properties resulted in a narrower size distribution for $\text{Ag}_{0.5}\text{Au}_{0.5}$ NPs, compared to the other samples.

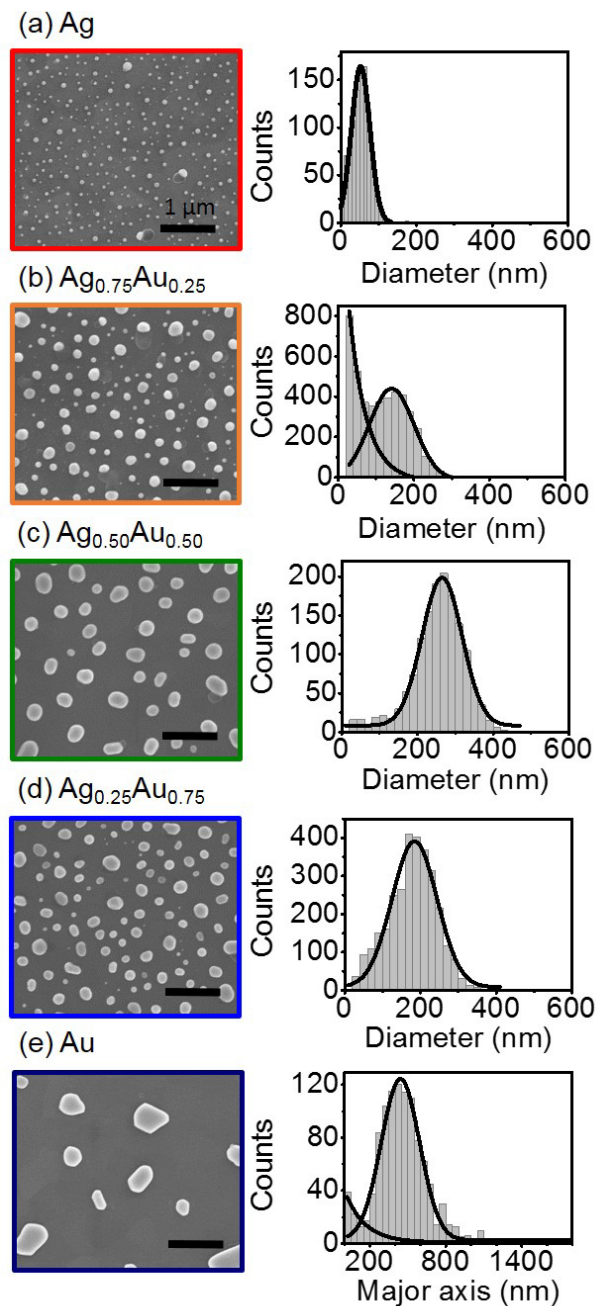


Figure 3.2: SEM plan-view images of (a) Ag, (b) $\text{Ag}_{0.75}\text{Au}_{0.25}$, (c) $\text{Ag}_{0.5}\text{Au}_{0.5}$, (d) $\text{Ag}_{0.25}\text{Au}_{0.75}$ and (e) Au nanoparticles (NPs) showing size and shape distribution. The corresponding diameter statistics are shown on the second row, where the average diameter for each sample is 53 ± 29 nm, 141 ± 70 nm, 253 ± 62 nm, 184 ± 70 nm, and 441 ± 176 nm, respectively. Here, the uncertainties refer to the full-width-half-maximum of the Gaussian fits. For Au NPs the major axis of a hemispheroid is used to describe their size distribution.

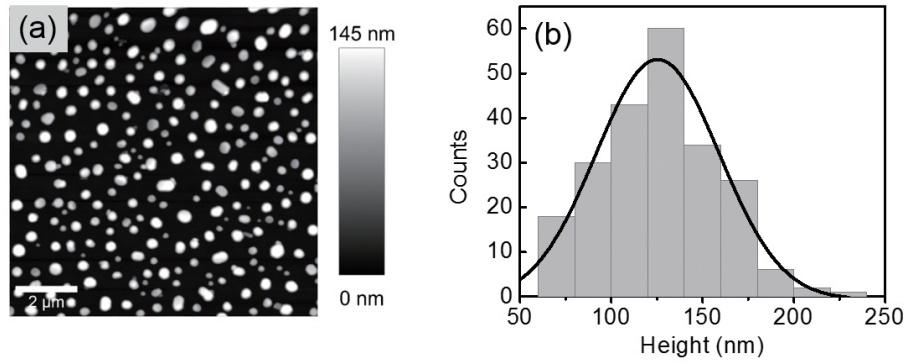


Figure 3.3: (a) AFM image of $\text{Ag}_{0.5}\text{Au}_{0.5}$ NPs sample. (b) Histogram of NPs height distribution (average height = 126 ± 40 nm).

Table 3.1: Statistical parameters for $\text{Ag}_x\text{Au}_{1-x}$ samples, obtained by the deposition of thin film alloys and sequential annealing treatment in N_2 . The initial film thickness and root mean square error (RMSE) were determined by ellipsometry (through transmission and reflection measurements). The particle size and distribution were determined by analyzing at least $500 \mu\text{m}^2$. The nominal and measured (by EDS) chemical composition are in very good agreement. Here, size refers to the base diameter for all samples containing Ag, and to the major axis of a hemispheroid for the pure Au sample (where the minor axis is equal to 368 ± 148 nm).

	Ag	$\text{Ag}_{0.75}\text{Au}_{0.25}$	$\text{Ag}_{0.5}\text{Au}_{0.5}$	$\text{Ag}_{0.25}\text{Au}_{0.75}$	Au
Initial film thickness (nm)	12.8	14.9	10.8	14.7	11.2
Thin film RMSE	3.1	2.7	3.0	2.6	2.8
Average NP size(nm)	53	142	253	184	441
Size standard deviation (nm)	29	70	62	70	176
Substrate area coverage (%)	7.0	12.0	19.0	18.6	9.3
Number of particle / μm^2	37	12	3	7	0.7
NPs with aspect ratio 1.0 - 1.3 (%)	83.2	86.1	79.1	80.2	32.7
EDS	$\text{Ag}_{1.0}$		$\text{Ag}_{0.54}\text{Au}_{0.46}$		$\text{Au}_{1.0}$

To assess the potential of our scalable fabrication method to produce arrays of NPs with tunable LSPR, we analyze the optical response of the NPs at the macro- and nanoscale. Figure 3.4 presents the measured and simulated transmission spectra for the $\text{Ag}_x\text{Au}_{1-x}$ system. For all samples containing Ag we observe well-defined resonance peaks, and a red shift of the LSPR by increasing the Au content. Figure 3.4b displays the photographs of the alloyed NPs on ITO/glass, where the corresponding colors of the samples are in agreement with the measured transmission spectra (due to their respective plasmon resonance). In order to corroborate our measurements, we use the FDTD method. Our calculated transmission spectra are in good agreement with our measurements, as shown in Figure 3.4c. We calculate the transmission for NPs with average diameter and density obtained from Figure 3.2, mimicking the fabricated nanostructures. Because the dielectric function of metal alloys cannot be estimated as the linear combination of their pure counterparts [77], we use the experimentally determined index of refraction of the alloyed thin films (before annealing treatment) as the input in our calculations by combining transmission and reflection ellipsometry measurements (see Figures 3.5, 3.6, and 3.7). The small discrepancy observed on the width of the LSPR peak results from the fact that our calculations do not take into account the size and the random spatial distributions of the NPs, which is well known to affect the broadening of the LSPR [49, 149, 150]. The chemical composition contributes to the red shift of the transmission (see Figures 3.8 and 3.9 for NP size and morphology effects).

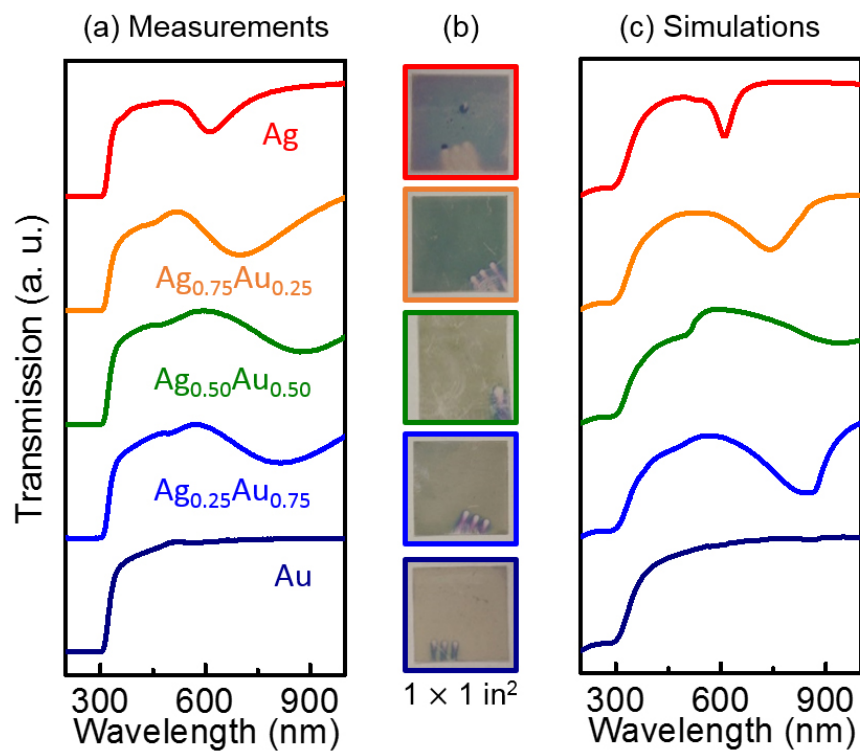


Figure 3.4: (a) Measured transmission spectra of the Ag_xAu_{1-x} NPs. (b) Photographs of alloyed NPs on ITO/glass substrate on a white background. (c) Finite-difference time-domain simulated transmission spectra.

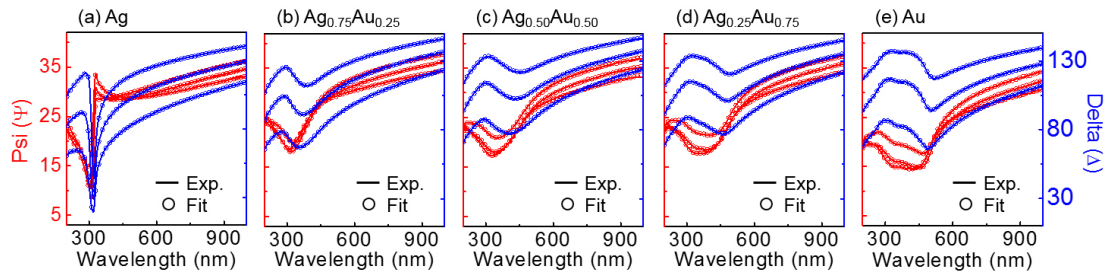


Figure 3.5: Raw ellipsometry measurements for $\text{Ag}_x\text{Au}_{1-x}$ alloyed thin films. Here, Psi (Ψ , open red circles) and Delta (Δ , open blue circles) were obtained from combined transmission and reflection measurements at 60, 65 and 70 degrees. The solid lines correspond to their fit, obtained by enforcing Kramers-Kronig relation, as described in. Substrate: glass.

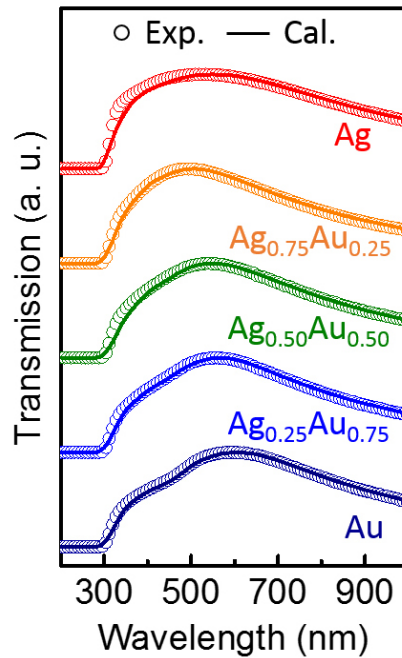


Figure 3.6: Transmission spectra for $\text{Ag}_x\text{Au}_{1-x}$ alloyed thin films. The measured and the calculated data refer to the open circles and solid lines, respectively.

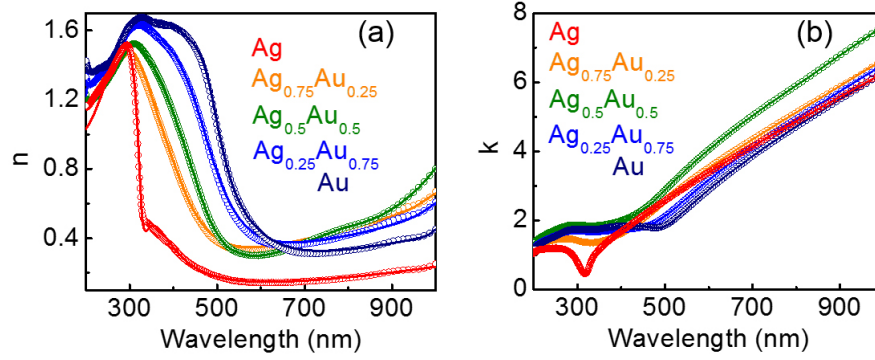


Figure 3.7: (a) Real n and (b) imaginary k components of the index of refraction for $\text{Ag}_x\text{Au}_{1-x}$ thin films measured by ellipsometry (open circles) and fit obtained using the multi-coefficient material model (solid lines).

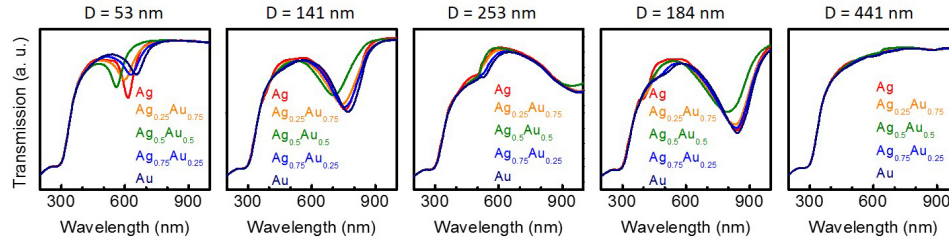


Figure 3.8: Calculated transmission as a function of NP size for $\text{Ag}_x\text{Au}_{1-x}$. The NP diameter (D) and spatial distribution used in the calculations were obtained from experimental data (Table 3.1). The dielectric function is experimentally determined (from Figure 3.7).

Also, we observe a similar red shift on the LSPR from pure Ag to pure Au through the scattering and absorption efficiencies of perfectly spherical NPs using the Mie Scattering Theory, see Figure 3.10. Here the scattering efficiency Q_{scat} and the absorption efficiency Q_{abs} are defined as:

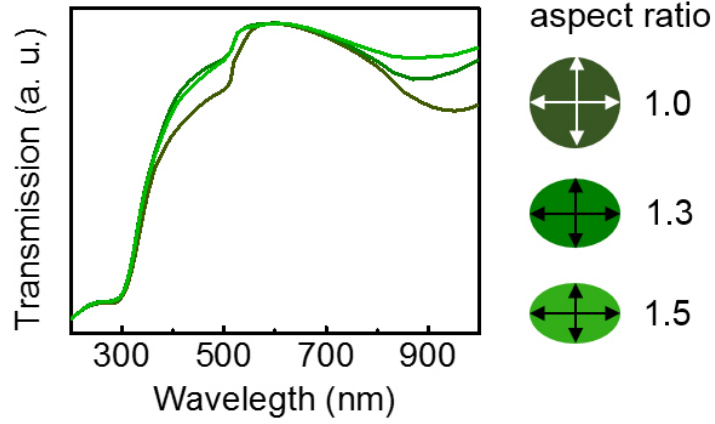


Figure 3.9: Calculated transmission spectra for $\text{Ag}_{0.5}\text{Au}_{0.5}$ NPs with different aspect ratio. Major axis = 253 nm.

$$Q_{scat} = \frac{\sigma_{scat}}{\pi r^2} \quad (3.1)$$

and

$$Q_{abs} = \frac{\sigma_{abs}}{\pi r^2} \quad (3.2)$$

where, σ_{scat} and σ_{abs} are the scattering and the absorption cross-sections, respectively, and r is the radius of the particle. The absence of a transmission peak for the pure Au sample is due to the very low density of NPs; because the peak shift of pure Au NPs has been extensively studied [108] it is not the focus of this work.

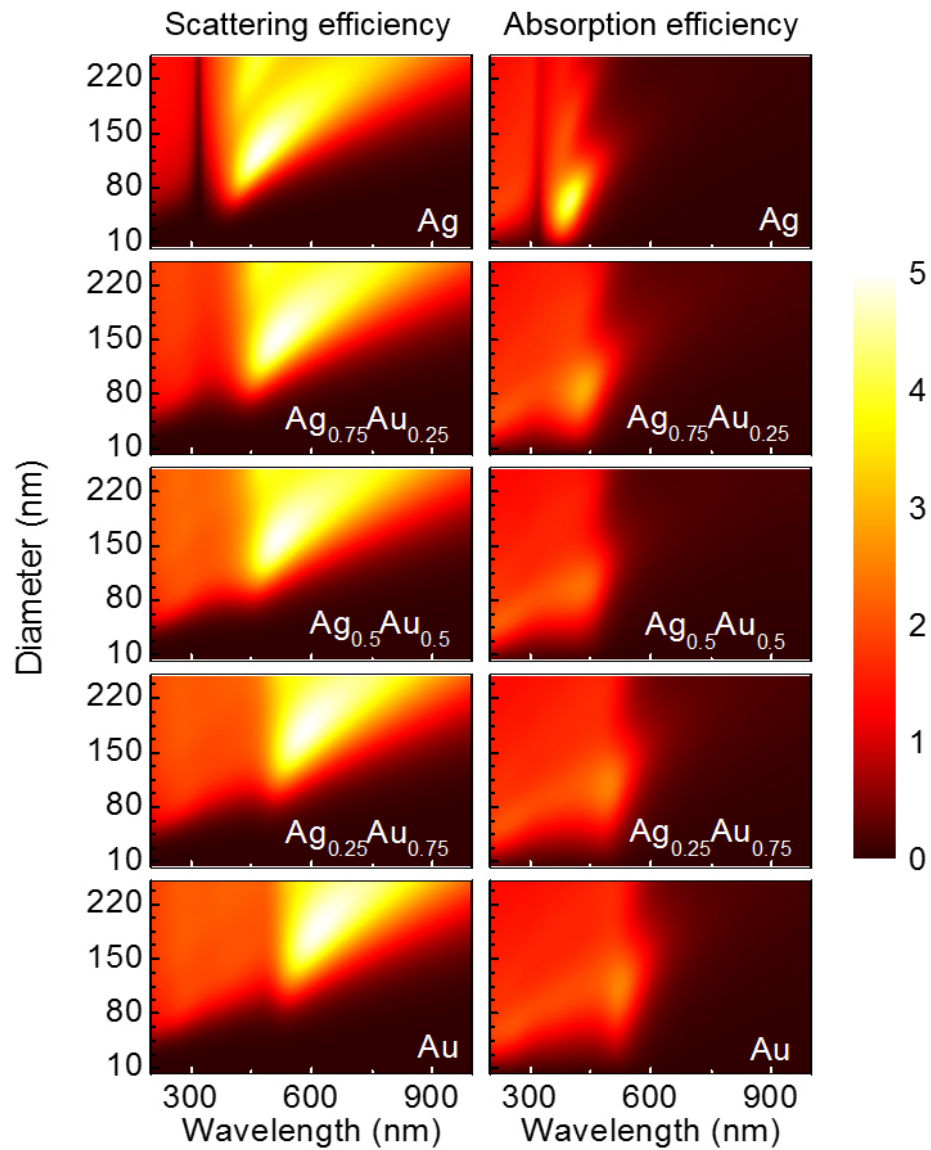


Figure 3.10: Scattering and absorption efficiencies calculated through Mie Scattering Theory for $\text{Ag}_x\text{Au}_{1-x}$ spherical nanoparticles showing a progressive red shift of the LSPR from Ag to Au.

To further evaluate if the fabrication method implemented here provides fully alloyed nanostructures, we perform energy-dispersive X-ray spectroscopy (EDS) elemental mapping on the $\text{Ag}_{0.5}\text{Au}_{0.5}$ sample, as shown in Figure 3.11a. We first mill the front and back of a representative NP using a Ga^+ focused ion beam (FIB) to minimize background signal from other NPs, see Figure 3.11b. Secondly, as presented in Figure 3.11c-h, we sequentially mill and image the NP to determine the elemental distribution within the structure and to confirm that no material segregation took place during the annealing treatment. A volumetric homogenous distribution of both Ag and Au is detected within the NP, verifying that a solid solution is formed at the nanoscale, in agreement with the phase diagram for $\text{Ag}_x\text{Au}_{1-x}$ system [151]. The amount of Ag and Au per NP is further confirmed by the plan-view EDS analysis of different NPs, which show an average chemical composition of $\text{Ag}_{0.54}\text{Au}_{0.46}$, (see Figures 3.12-3.13 and Table 3.2).

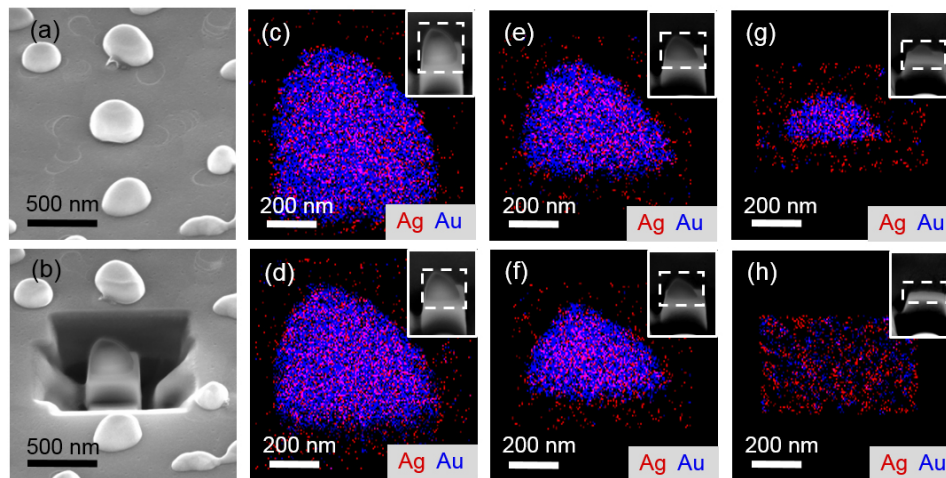


Figure 3.11: SEM images of a representative $\text{Ag}_{0.5}\text{Au}_{0.5}$ NP (a) before and (b) during FIB milling. (c-h) EDS composition maps obtained during serial milling (70 nm slice thickness) of the NP, showing homogenous distribution of Ag and Au throughout their volume, confirming the formation of a solid solution at the nanoscale. Insets: Cross-sectional SEM images of the NP after each milling step.

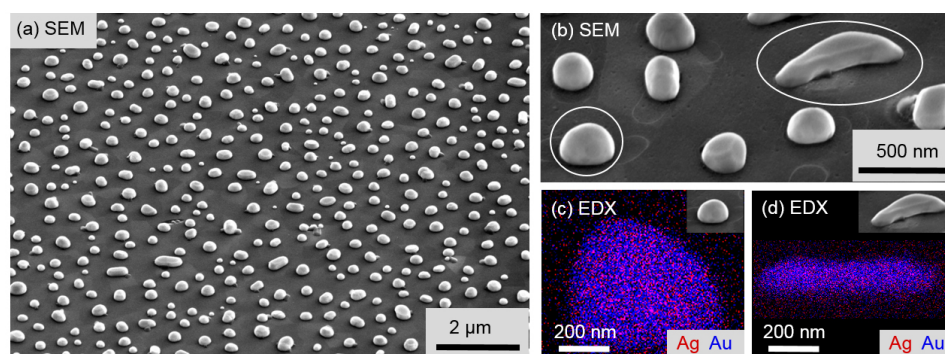


Figure 3.12: SEM image of (a-b) $\text{Ag}_{0.5}\text{Au}_{0.5}$ NPs (tilt: 52 degrees). (c-d) Cross-section EDX mapping of two NPs [marked in (b)] with very distinct size and shape, showing uniform distribution of Ag and Au.

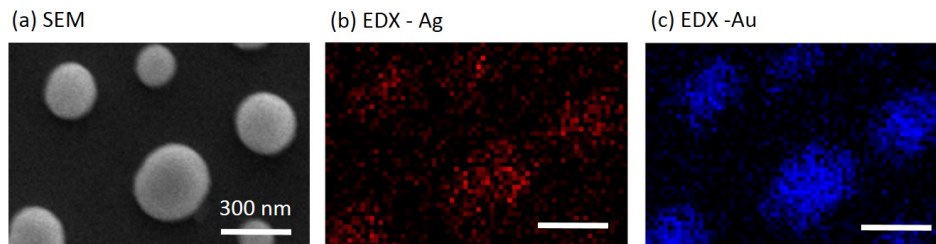


Figure 3.13: (a) SEM image of $\text{Ag}_{0.5}\text{Au}_{0.5}$ NPs sample. EDS mapping of (b) Ag and (c) Au on the same the area, showing metals uniform chemical distribution.

Table 3.2: Chemical composition obtained from EDS point measurements on nine representative NPs for the $\text{Ag}_{0.5}\text{Au}_{0.5}$ sample, showing average composition of $\text{Ag}_{0.54}\text{Au}_{0.46}$.

NP number	Ag (fraction)	Au (fraction)
1	0.56	0.44
2	0.57	0.49
3	0.51	0.49
4	0.49	0.51
5	0.57	0.43
6	0.52	0.48
7	0.56	0.44
8	0.54	0.46
9	0.55	0.45
Average	0.54	0.46

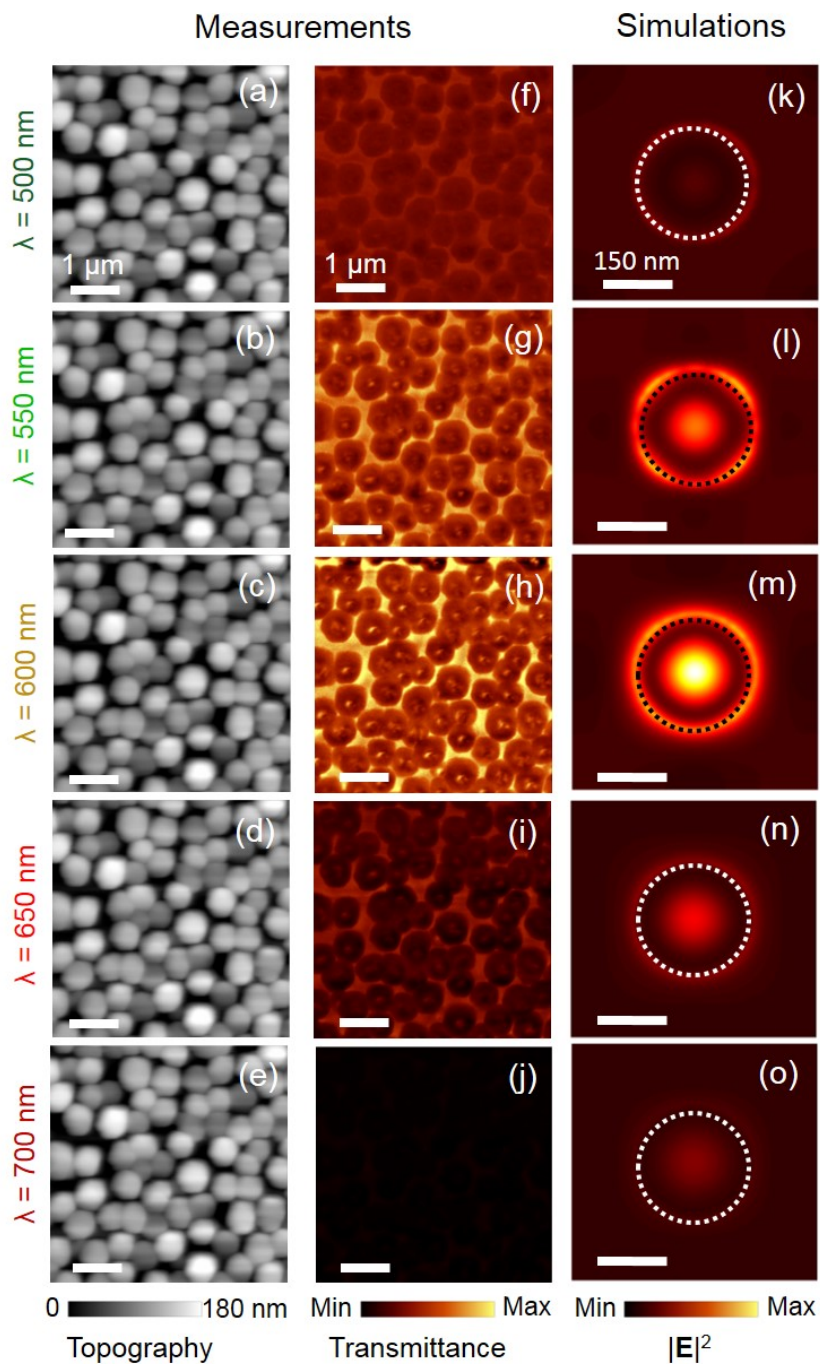


Figure 3.14: (a-e) Topography and (f-j) NSOM transmittance measurements for representative $\text{Ag}_{0.5}\text{Au}_{0.5}$ NPs showing strong spectral dependence. (k-o) FDTD simulation of the square modulus of the electric field ($|E|^2$) profile as a function of wavelength, where the dashed circles refer to the NP position. Illumination conditions: unpolarized point dipole located at the top of the NP.

3.3 Near-field Optical Response: Experiments and Simulations

We probe the near-field optical response of the fully alloyed $\text{Ag}_{0.5}\text{Au}_{0.5}$ NPs sample by spectrally dependent NSOM measurements in illumination mode. Here, an Al-coated Si cantilever with a hollow SiO_2 pyramid tip with ~ 60 nm aperture is scanned across the sample surface and the transmission signal is detected at the far-field with a $60\times$ objective lens located 0.3 mm underneath the sample. The topography and transmission signals are acquired simultaneously. As shown in Figure 3.14a-e, the NPs are well resolved throughout all measurements, indicating no significant tip changes during the scans. Figure 3.14f-j displays the spectral dependence of the transmittance for the NPs within the visible range of the spectrum, from 500 nm to 700 nm. We observe high transmittance features irrespective of the illumination wavelength, both underneath and around the edges of the NPs (see Figure 3.15 for more details). Nevertheless, there is a remarkable higher local transmission at 600 nm, compared to the scans acquired at other wavelengths. This singular characteristic results from the electric field enhancement caused by the particles LSPR at 600 nm. In fact, the shape of the macroscopic transmission (see Figure 3.4) follows the same behavior revealed by the wavelength dependent NSOM scans, caused by the LSPR. As expected, the bare ITO shows high transmittance between 500 nm and 700 nm. Figure 3.14k-o shows simulated maps of the square modulus of the electric field ($|\mathbf{E}|^2$) underneath a hemispherical $\text{Ag}_{0.5}\text{Au}_{0.5}$ NP on ITO/glass

substrate, using an unpolarized point dipole at the top of the NP as the illumination source [120], where the dashed lines refer to the NP size. Our simulations are in excellent agreement with the NSOM measurements: at 600 nm the $|E|^2$ is extremely high just below the NPs, at its center and around its edges. The $|E|^2$ is very low on the ITO layer due to the fact that the simulations are performed using a dipole light source, instead of multiple ones throughout the simulation space.

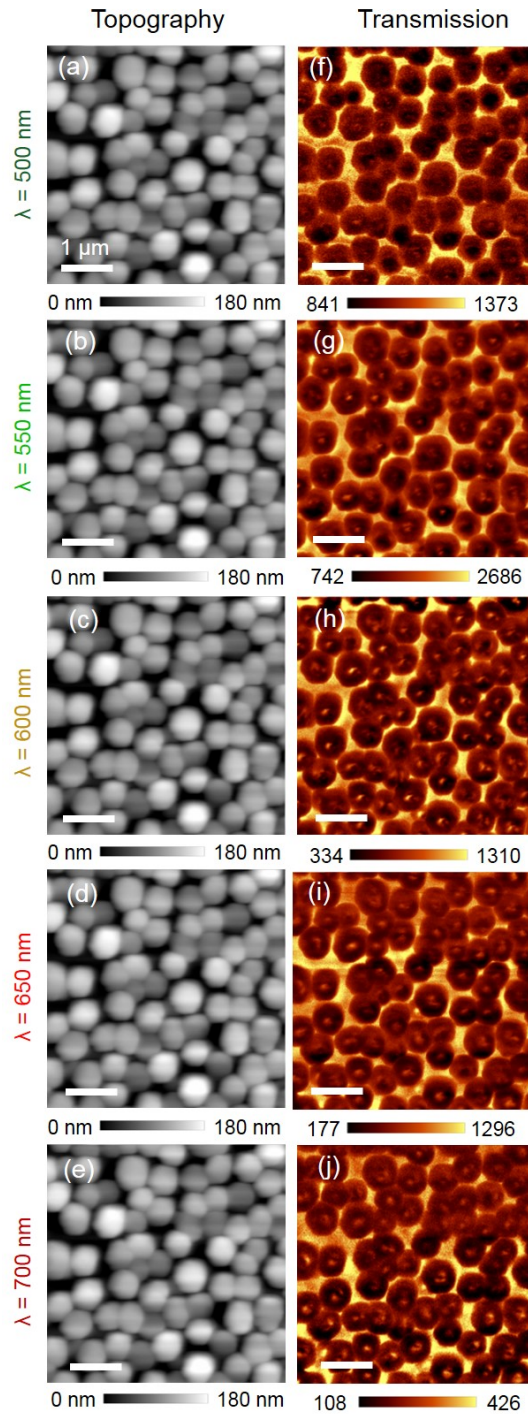


Figure 3.15: (a-e) Topography and (h-j) NSOM transmission measurements for the $\text{Ag}_{0.5}\text{Au}_{0.5}$ NPs sample as a function of wavelength, where the counts refer to the number of transmitted photons. For the transmission measurements: incident power from 500 nm to 700 nm equal to 149 μW , 132 μW , 52 μW , 96 μW , and 230 μW , respectively.

To acquire the full picture of the near-field light-NPs interactions taking place, we simulate the cross-section electric field $|E|^2$ decay as a function of wavelength. Figure 3.16 shows $|E|^2$ across a 253 nm hemispherical $\text{Ag}_{0.5}\text{Au}_{0.5}$ NP on top of a 70 nm ITO and 500 nm glass substrate. Due to the LSPR, the intensity of the electric field at 600 nm is enhanced 30 times around the NP, in the ITO layer. Conversely, at 500 nm and 700 nm this effect is almost fully suppressed, and the field intensity in the substrate gradually diminishes. The overall decrease of the electric field intensity at 500 nm is not as strong as at 700 nm due to the proximity with the quadrupole LSPR, as shown by the transmission spectra in Figure 3.4. Moreover, at 700 nm a large fraction of the incident light is reflected by the NP, the electric field is screened, resulting in low transmittance. The calculated field profile agrees very well with the NSOM measurements, Figure 3.14f-j, which also shows a maximum transmittance at 600 nm, assisted by the LSPR.

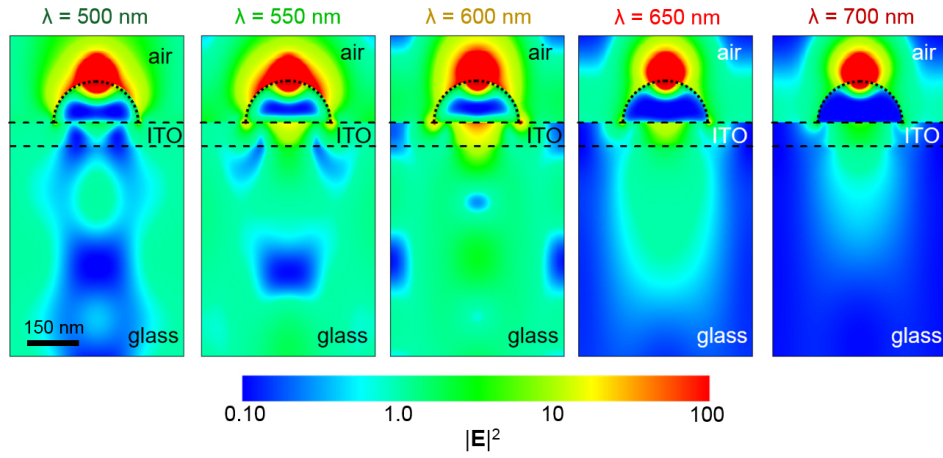


Figure 3.16: Cross-section profile of the square modulus of the electric field $|E|^2$ for a 253 nm hemispherical $\text{Ag}_{0.5}\text{Au}_{0.5}$ nanoparticle on a 70 nm ITO / 500 nm glass substrate as a function of wavelength. Illumination conditions: unpolarized point dipole at the top of the nanoparticle ($\lambda = 500$ nm, 550 nm, 600 nm, 650 nm and 700 nm).

3.4 Experimental Methods

3.4.1 Fabrication of Alloyed Nanostructures

Alloyed thin films were fabricated via the co-sputtering deposition of pure Ag (99.99%) and Au (99.99%) at room temperature, with deposition rates calibrated to reach different nominal chemical compositions, ranging from Ag, $\text{Ag}_{0.75}\text{Au}_{0.25}$, $\text{Ag}_{0.5}\text{Au}_{0.5}$, $\text{Ag}_{0.25}\text{Au}_{0.75}$ to Au. During deposition, the sample stage was rotated at 8 rpm to ensure uniform elemental distribution within each thin-film sample. The thin films were deposited onto 1×1 in² ITO (70 nm)/glass substrates that were previously cleaned with acetone and DI water, then dried with N_2 . The as-obtained thin films were annealed at 600 °C for 1 hour in N_2 flow of 1 atm to form the alloyed

nanostructures.

3.4.2 Macroscopic Transmission Measurements

The transmission measurements were performed using an ellipsometer (200-1000 nm) at normal incidence, where the base line was air.

3.4.3 Chemical Composition Analysis

Surface and cross-sectional energy dispersive x-ray spectroscopy (EDS) was performed using a dual-beam focused ion beam/scanning electron microscope, equipped with an EDS detector. Cross sections of the NPs were milled with a Ga⁺ ion beam current of approximately 1 pA. Because the resolution of the EDS analysis is limited by the electron interaction volume (rather than by the beam size), probing thin sections of the NPs ensured a reliable analysis, with high spatial resolution. The relative composition of the particles was determined using the Au-M and Ag-L α X-ray lines (at characteristic energies of 2.120 and 2.984 keV, respectively), excited using a primary electron beam with a 10 kV accelerating voltage, \sim 2 nA current, and a 100 μ s dwell time.

3.5 Conclusions

In summary, we have investigated the optical properties of fully alloyed Ag_xAu_{1-x} NPs at the macro- and nano-scale. Making use of a scalable and low-cost process, random and fully alloyed NPs were produced by the dewetting of alloyed thin films,

with chemical composition ranging from pure Ag to pure Au. We found that the NPs spatial distribution heavily depends on the original chemical composition of the thin film, instead of its thickness. As confirmed by EDS measurements, a uniform elemental distribution of Ag and Au was obtained for the $\text{Ag}_{0.5}\text{Au}_{0.5}$ sample demonstrating that a solid solution is formed at the nanoscale. We revealed the near-field effect of the LSPR in the alloyed NPs through spectrally dependent NSOM measurements. High local transmittance was observed both underneath and around the edges of the nanostructures. These measurements were in excellent agreement with our FDTD simulations, which showed that the $|\mathbf{E}|^2$ in the vicinity of and within the particles strongly varies as a function of wavelength. Our results open the possibility to explore an additional knob to tune the LSPR in metallic nanostructures fabricated by a scalable physical approach: their chemical composition. By using different substrates, with distinct wettability, one could implement the method presented here to realize self-assembled alloyed nanostructures with a variety of chemical compositions and optical responses extended to a broader range of the spectrum. For instance, Al-based alloys could expand the functionality of some optoelectronic devices that operate in the visible into the UV range of the spectrum.

Chapter 4: Band Structure Engineering by Alloying for Plasmonics

Summary: SPP enables the subwavelength confinement of an electromagnetic field, which in turn can be used in optical devices ranging from sensors to nanolasers. However, the intrinsic band structure of metals severely limits its occurrence in photonic devices. Here, we introduce the strategy of engineering the band structure of metallic materials by alloying. We experimentally and theoretically establish the control of the dispersion relation by varying the film chemical composition.

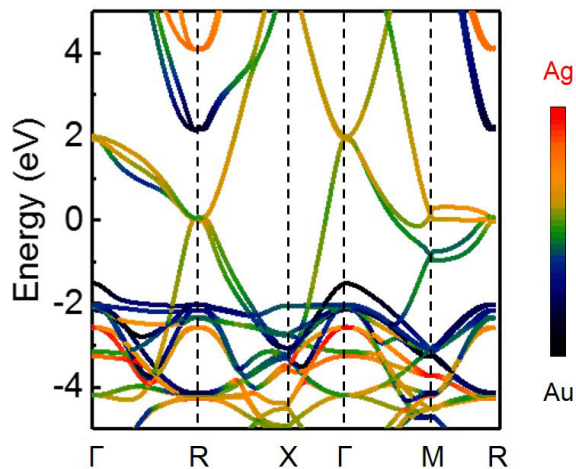


Figure 4.1: Band structure of Ag-Au alloy.

We study the valence band spectra (VBS) of Ag-Au alloys. Our density functional theory calculations of the alloys' band structure predict the same variation of the threshold of the interband transition, which is in very good agreement with our optical and VBS results. By achieving Ag-Au alloys with tunable dispersion relation and by elucidating the correlation between its optical behavior and band structure, we anticipate the fine control of the optical properties of metallic materials beyond pure metals. In turn, our results will likely enable the further development of new material options for plasmonics, including other metal alloy combinations with engineered chemical composition. This chapter is adapted from a manuscript that is currently under review.

4.1 Introduction

SPPs are defined as travelling electromagnetic waves at the interface between a metal and a dielectric, resulting from a waveguiding effect that occurs when the wave vector of both the photons and the surface plasmons match. The subsequent electromagnetic field propagates along the metal-dielectric interface with a much smaller wavelength than the incident light [5]. These characteristics give rise to a strong electric field confinement near the surface, which allows for the manipulation of light at deep sub-wavelengths [152], leading to a variety of applications including nanolasers [153], sensors [154], bio-imaging [155], surface-enhanced Raman spectroscopy [123, 156], color displays [157], and others [158–161].

To improve the performance of today's photonic systems, researchers have extensively investigated the fundamental relation between the wave vector and energy of an SPP wave - named dispersion relation. This quantity describes the propagation of light within a material (*i.e.* medium), extremely relevant for the abovementioned optical devices. Therefore, understanding the dispersion relation can allow the design of optical materials with superior response, ranging from 2D van der Waals to oxides and metals. Concerning 2D materials, it can uncover the origin of tunable polaritons in hyperbolic metamaterials based on graphene and hexagonal boron nitride (h-BN), which is due to the hybridization of SPP and surface phonon polaritons [162]. As another example, by utilizing the band-edge mode of the dispersion relation in metallic nanocavities [153], lasing with a 200 times enhancement of the spontaneous emission rate of the dye has been reached [163].

As one of the emerging photonic materials, noble metal alloys with permittivity not achievable by pure metals [11,158], have been proposed as alternative candidates for plasmonics [130,161,164,165] because of their tunable dielectric functions, which make it possible to engineer the alloy composition to attain optical properties that will meet desired resonances. In turn, this tunability could be used to improve the performance of devices for a variety of applications, such as perfect absorbers [97], photovoltaics [133], metallurgy [166], catalysis [167], and electrocatalysis [168–170]. However, in contrast to the well-investigated dispersion relation of pure noble metals (Ag and Au) [171–176], the dispersion of SPPs for Ag-Au alloys has rarely been explored [177]. Additionally, the correlations between the effect of alloying on the optical dispersion relation, the threshold of the interband transition, and the new materials band structure are still not well understood.

Here, we experimentally and theoretically demonstrate the SPP dispersion relations of Ag-Au alloyed thin films ($\text{Ag}_x\text{Au}_{1-x}$) and explain the origin of their behavior by combining optical and X-ray photoelectron spectroscopy (XPS) measurements with density functional theory (DFT) calculations of band structure. The $\text{Ag}_x\text{Au}_{1-x}$ alloy represents an ideal model system to establish the correlation between the material dispersion relations and its electronic band structure as a solid solution is formed for the entire chemical composition range [64]. We map the reflectivity as a function of wavelength and angle of incidence for $\text{Ag}_x\text{Au}_{1-x}$ films using the Kretschmann configuration [178], and find that the dispersion relations can be engineered by changing the alloy chemical composition. The physical origin of the observed optical response is correlated to the valence band spectra (VBS) obtained

by XPS measurements. In particular, the VBS in conjunction with partial density-of-states (DOS) calculations reveal a dependence of the binding energy onset of the d band and the corresponding energy of the transmission resonance peak for a given alloy. This dependence indicates the relation between the threshold of the interband transition and the energy of the d band. To underpin this relation, we further calculate the band structure for each alloy by DFT to assess the regions in reciprocal space where optical transitions occur. A similar change for the interband transition is determined, agreeing remarkably well with our optical and XPS measurements. Further, we reveal the non-linear specific contribution of each metal to the band structure of the alloys. Overall, our results provide fundamental insight into the origin of the surface plasmon modes in $\text{Ag}_x\text{Au}_{1-x}$ alloys and show that the dispersion relation can be tuned upon changing the alloys chemical composition. We anticipate the combined experimental + computational approach presented here to be extended to other materials, including non-metallic ones. Ultimately, their optical behavior is influenced by the electronic properties (*e.g.* density of carriers), which urgently requires a combined analysis. When merged with a combinatorial materials screening, this paradigm can offer a library of emerging materials for photonics.

4.2 Tunable Dispersion Relations

We fabricate the alloyed metallic thin films by co-sputtering Ag and Au onto glass microscope slides. The samples are rotated during deposition to ensure uniform chemical composition, confirmed by EDS as shown in Table 4.1. To evaluate the

macroscopic optical properties, we measure transmission spectra for each sample, as shown in Figure 4.2. The experimental transmission peaks in Figure 4.2a reveal the surface plasmon resonances of the films. These peaks shift from 325 nm (pure Ag), to 375 nm ($\text{Ag}_{0.75}\text{Au}_{0.25}$), to 425 nm ($\text{Ag}_{0.50}\text{Au}_{0.50}$), to 480 nm ($\text{Ag}_{0.25}\text{Au}_{0.75}$), to 510 nm (pure Au), indicating the change of the optical response upon varying the chemical composition. These measurements agree with the color change of the sample (see photographs in Figure 4.2b). Further, we use the Fresnel equations [179] to calculate the transmission of the thin films. The spectra in Figure 4.2c show excellent agreement between our calculations and the experimentally determined values. Here the permittivity (see Figure 4.3) and the film thicknesses (inputs of our calculation) are determined by ellipsometry measurements .

Table 4.1: Chemical and optical properties of $\text{Ag}_x\text{Au}_{1-x}$ thin films.

Sample	Average EDS of 3 locations	Thickness from Ellipsometry (nm)
Ag	N/A	50.11
$\text{Ag}_{0.75}\text{Au}_{0.25}$	$\text{Ag}_{0.77}\text{Au}_{0.23}$	51.42
$\text{Ag}_{0.50}\text{Au}_{0.50}$	$\text{Ag}_{0.52}\text{Au}_{0.48}$	49.66
$\text{Ag}_{0.25}\text{Au}_{0.75}$	$\text{Ag}_{0.23}\text{Au}_{0.77}$	49.85
Au	N/A	49.85

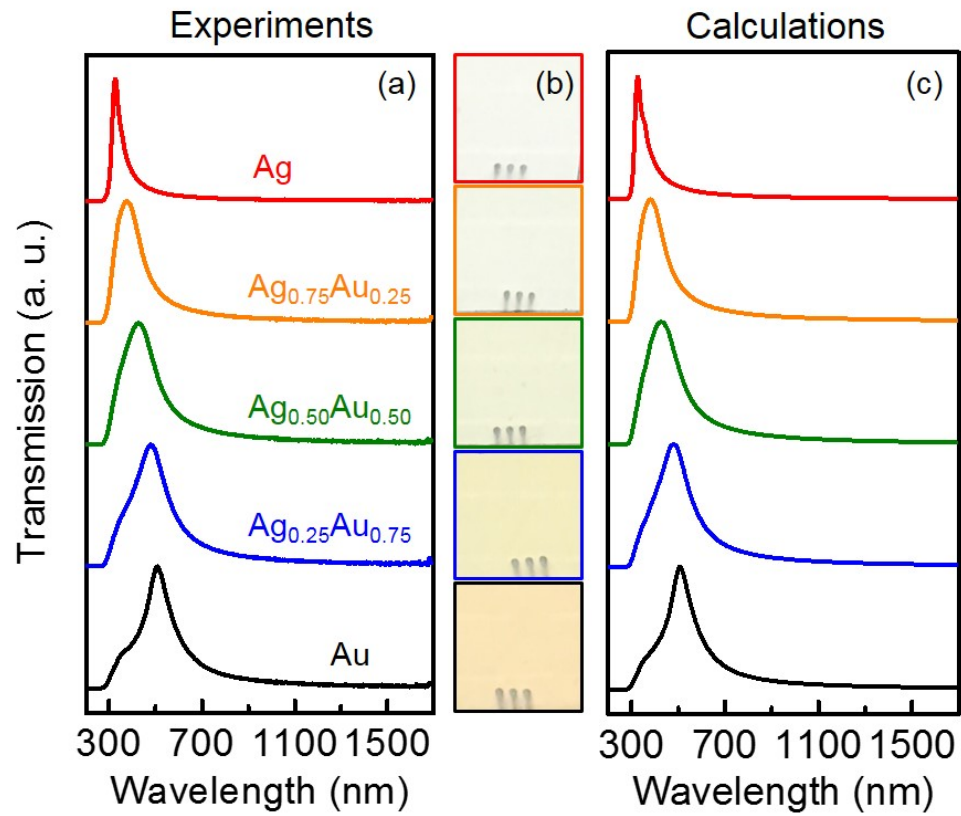


Figure 4.2: (a) Measured transmission spectra of Ag_xAu_{1-x} alloyed thin films. (b) Photographs of the alloyed films on glass substrates. (c) Calculated transmission spectra using Fresnel equations. Film nominal thickness: 50 nm. Sample size: $2.54 \times 2.54 \text{ cm}^2$.

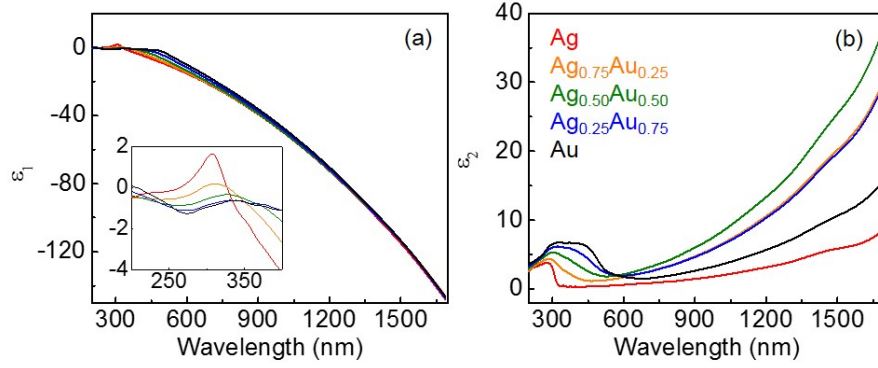


Figure 4.3: (a) Real (ϵ_1) and (b) imaginary (ϵ_2) part of the permittivity for $\text{Ag}_x\text{Au}_{1-x}$ thin films. Inset: zoom-in of ϵ_1 for the ultraviolet region of the spectrum.

One approach to assess the dispersion relations of the SPP for the $\text{Ag}_x\text{Au}_{1-x}$ alloys is by measuring the reflectivity of the films. Here, we use the Kretschmann configuration [178] to provide sufficient momentum to excite SPPs [118]. In our setup, the laser passes through a fused silica prism, which is attached to the glass substrate using an index matching liquid. The ratio of the reflected power to the incident power is then recorded at each wavelength and incident angle to obtain the reflectivity. Figure 4.4 displays the reflectivity maps for all $\text{Ag}_x\text{Au}_{1-x}$ alloyed thin films. The blue narrow band in Figure 4.4a-e shows reflectivity damping originating from the excitation of leaky modes due to destructive interference of reflected and transmitted light when using prism coupling [180]. Our measurements shows that as the Au content increases, the SPP band broadens. For example, at 600 nm the full-width-half-maximum of the band is 0.5 degrees for pure Ag and 1.9 degrees for pure Au. The change of the bandwidth for SPP modes provides a tunable optical

sensitivity while the chemical stability is kept by the use of Ag-Au alloys [181]. In addition, our experiment has excellent agreement with the theoretical calculations using the transfer matrix method [182], as shown in Figure 4.4f-j. The position and intensity of the band, as well as the critical angle (corresponding to the max reflection), match well between the measurements and calculations. To optimize for the largest attenuation of reflection power the films are fabricated with a 50 nm nominal thickness as per critical coupling when using the Kretschmann configuration [118].

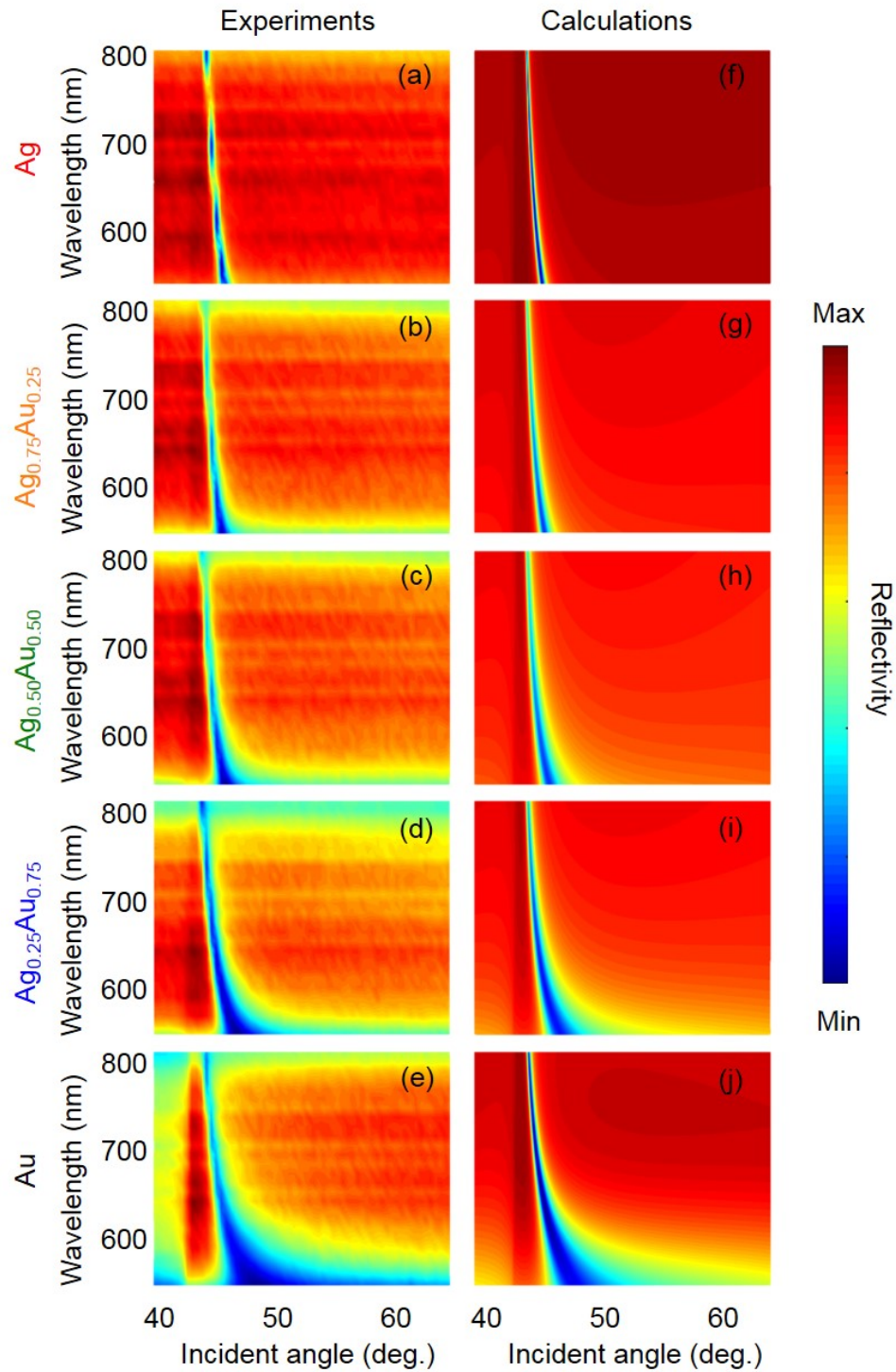


Figure 4.4: (a-e) Measured and (f-j) calculated reflectivity maps for $\text{Ag}_x\text{Au}_{1-x}$ alloyed thin films. The reflectivity is recorded by dividing the reflected power over the power of the incident light. Transfer matrix method is adopted using the experimentally determined permittivity and thickness for each metal and alloy as the inputs.

Figure 4.5 provides the dispersion relations for the $\text{Ag}_x\text{Au}_{1-x}$ alloys obtained from the SPP reflectivity measurements. The wavelength of the light and the incident angle are converted to energy and wave vector, respectively, using the following equations:

$$E = \frac{hc}{\lambda} \quad (4.1)$$

$$k = \sqrt{\epsilon_{prism}} \frac{f}{c} \sin\theta \quad (4.2)$$

where E is the energy of the incident light, h is Planck's constant, c is the speed of the light in vacuum, λ is the wavelength of the incident light, k is the wave vector, ϵ_{prism} is the permittivity of the fused silica prism [183], f is the frequency, and θ is the incident angle. The intensity in the dispersion map corresponds to the reflectivity at each λ and θ . Figure 4.5a shows the measured dispersion relation of pure Ag with the anti-symmetric plasmon mode resolved [184]. The symmetric mode requires wave vector larger than the prism coupling configuration could offer, thus not accessible [5]. We find that the dispersion relation varies from Ag to Au and it bends towards a lower frequency region for Au-rich alloy ($\text{Ag}_{0.25}\text{Au}_{0.75}$), which established the control of the dispersion relation by changing the film chemical composition. To corroborate our experiment, we use the experimentally determined permittivity (see Figure 4.3) to calculate the dispersion maps, as shown in Figure 4.5f-j. An excellent agreement is achieved between the experiments and calculations, validating our approach to resolve the dispersion.

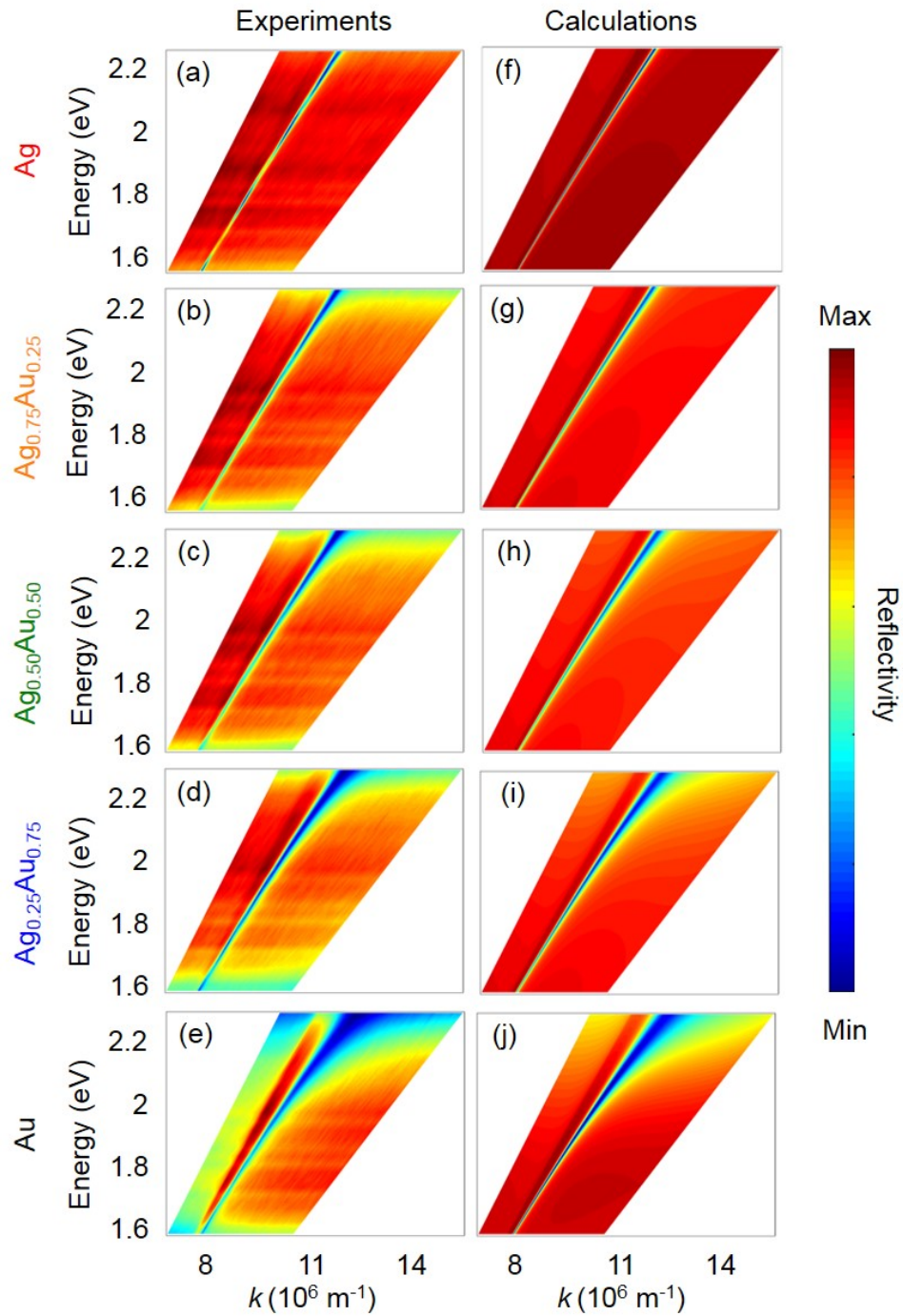


Figure 4.5: (a-e) Measured and (f-j) calculated dispersion relation for Ag_xAu_{1-x} alloys. The color refers to the reflectivity at each wave vector k and energy. The minimum reflectivity corresponds to the excitation of surface plasmon polaritons (SPP).

4.3 Electronic Band Structures for Metallic Alloys

We experimentally determine the VBS for the alloys with XPS measurements to understand the underlying physics responsible for the change of the surface plasmon resonance, as shown in Figure 4.6. The overall shape of the VBS for $\text{Ag}_x\text{Au}_{1-x}$ (Figure 4.6a) agrees with what has been previously reported in the literature [185, 186]. Because the electrons of the d band are responsible for the electronic transitions within the visible range, we extract both the $d_{5/2}$ peak, and its corresponding split-off $d_{3/2}$ by fitting Gaussian functions to the raw spectra after a Shirley background subtraction. Figure 4.7 displays the fitting results. From the fitting analysis, a third contributing peak is found along with the $d_{5/2}$ and $d_{3/2}$ components, as evidenced by a shoulder on the lower binding energy side for each alloy. Therefore, the $d_{5/2}$ does not appear at the center of the lower energy peak in the VBS. The three fitted curves changed position with alloy composition (see Figure 4.7). Based on the partial DOS calculation (Figure 4.8), the three peaks are primarily represented by the d band component (*i.e.*, largest fractional contribution) at binding energies greater than ~ 1 eV for each metal or alloy. During the fitting, the peak splitting is variable, and we find that the separation between the $d_{3/2}$ and $d_{5/2}$ bands increases non-linearly (Figure 4.6b) as the Au content rises [187]. The width of the d bands has been attributed to several material characteristics [185, 186], but since the overall band structure contains information about additional populated states (*i.e.*, the shoulder peak) care must be taken when identifying the relaxed energy of excited electrons, and ascribing changes in VBS to specific properties.

The onset binding energy of the $d_{5/2}$ band is specifically investigated because it corresponds to the minimum energy needed for an optical excitation. We define the onset as the lower energy value at 5% of the peak height in order to distinguish the emergence of the peak from the background signal. Figure 4.6c reveals that this onset aligns well with the transmission measurement (also see Figure 4.9). For instance, the onset of $d_{5/2}$ for $\text{Ag}_{0.50}\text{Au}_{0.5}$ is at 2.05 eV and the transmission peak is at 2.40 eV (see Table 4.2), indicating the origin of the tunability for the interband transition is from the energy shift of the d band.

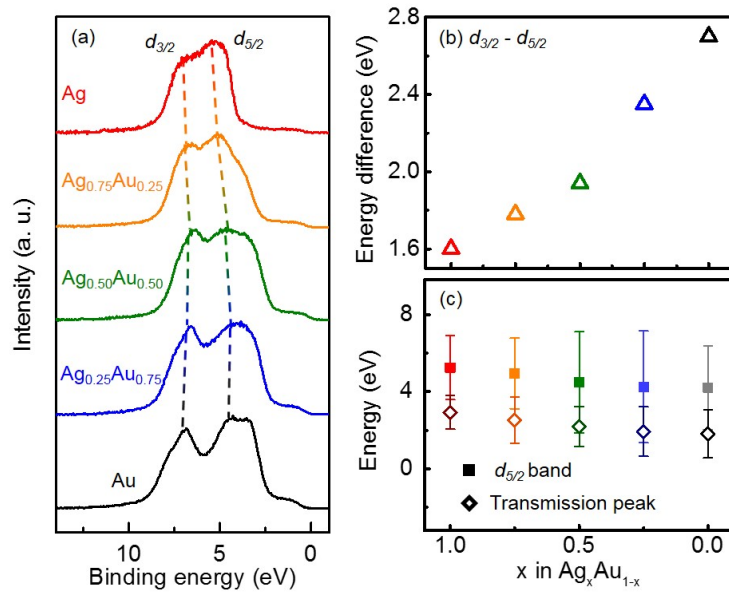


Figure 4.6: (a) Valence band spectra of $\text{Ag}_x\text{Au}_{1-x}$ alloyed thin films obtained by XPS. Dashed lines show the peak shift for $d_{3/2}$ and $d_{5/2}$, where the $d_{3/2}$ and $d_{5/2}$ peaks are fit by Gaussian functions. (b) Energy difference between $d_{3/2}$ and $d_{5/2}$ for each alloy. (c) Peak energy of $d_{5/2}$ band (solid squares) and transmission measurements (hollow diamonds). The error bars refer to bandwidth of $d_{5/2}$ and transmission peak, which is determined by the lower and higher energy values at 5% of its height.

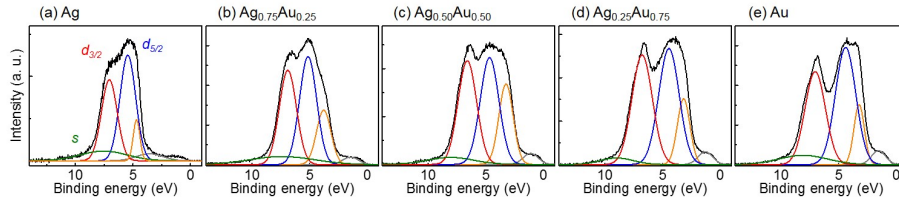


Figure 4.7: (a-e) Measured valence band spectra (black) and the Gaussian fittings (in color) of $\text{Ag}_x\text{Au}_{1-x}$ thin films.

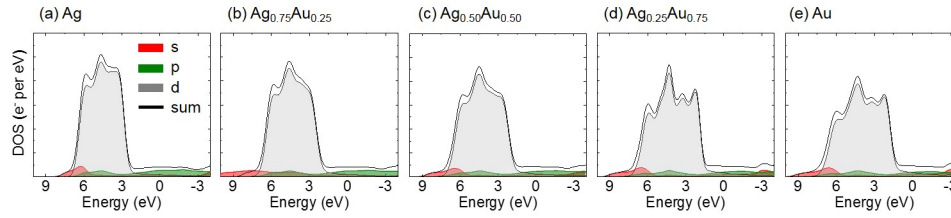


Figure 4.8: (a-e) Calculated partial density of states (DOS) at 0 Kelvin (solid line) of $\text{Ag}_x\text{Au}_{1-x}$ bulk cells using density functional theory. The contribution from s (red), p (green), d (grey) band to the overall partial DOS is shown.

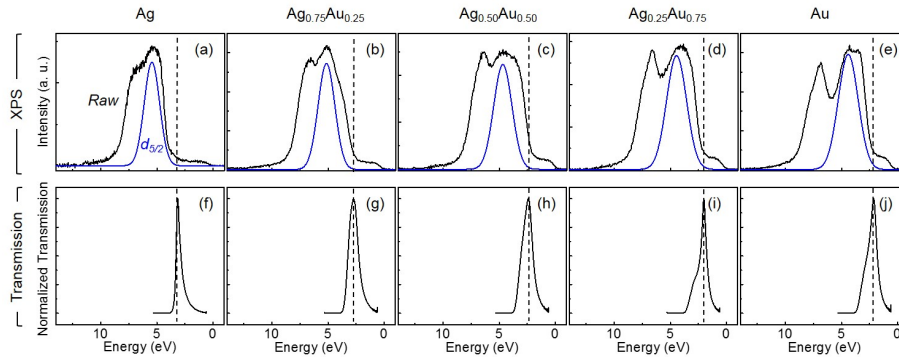


Figure 4.9: (a-e) Valence band spectra from XPS measurements for the $\text{Ag}_x\text{Au}_{1-x}$ alloyed thin films, only showing the raw spectra (black, top row) and the $d_{5/2}$ component (blue). (f-j) Normalized transmission spectra for the alloyed thin films. The dashed lines show the position of the transmission peak aligned with the onset of the $d_{5/2}$ band.

Table 4.2: Peak position extracted from valence band spectra for the $\text{Ag}_x\text{Au}_{1-x}$ thin films. The width is determined by the lower and higher energy value at 5% of the peak height.

Sample	$d_{5/2}$ (eV)	$d_{5/2}$ band width (eV)	Transmission peak (eV)	Transmission band width (eV)
Ag	5.45	3.34	3.13	1.78
$\text{Ag}_{0.75}\text{Au}_{0.25}$	5.15	3.66	2.72	2.40
$\text{Ag}_{0.50}\text{Au}_{0.50}$	4.68	5.26	2.40	2.06
$\text{Ag}_{0.25}\text{Au}_{0.75}$	4.45	5.80	2.13	2.56
Ag	4.41	4.34	2.01	2.50

To further investigate the electronic properties of $\text{Ag}_x\text{Au}_{1-x}$ alloys, we calculate its band structure using DFT [188], as shown in Figure 4.10. Figure 4.10a-e displays the band structure of $\text{Ag}_x\text{Au}_{1-x}$ alloys with the states from the d band (below the Fermi level) and the empty states (above the Fermi level). Here we model all alloys and pure metals as occupying sites in a cubic lattice containing four atoms per unit cell, providing a consistent picture of the unit cells. Because $\text{Ag}_x\text{Au}_{1-x}$ forms a solid solution [64], and the lattice constant remains roughly the same across the whole chemical composition range [115], four atoms are sufficient to fully describe the unit cells. While the important transitions within the visible range occur in the X-point, which was commonly defined, due to the folding of the bands, the critical point corresponds to Γ point in a 4-atom cubic cell [106]. Our computational study predicts that at the Γ point the position of the d band moves closer to the Fermi level as the Ag content is reduced, leading to a decrease of the energy gap between d band and empty state. This reduction indicates that the threshold of the interband transition for $\text{Ag}_x\text{Au}_{1-x}$ alloys should shift to longer wavelength regions as the Au content rises, agreeing with our optical and VBS measurements (see Figure 4.6c).

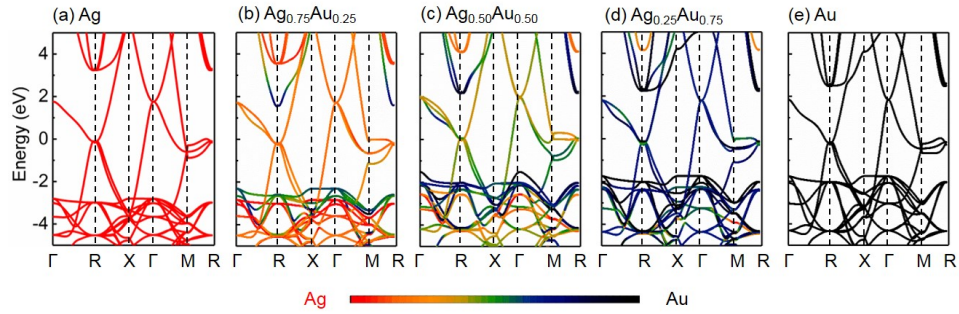


Figure 4.10: (a-e) Density functional theory band structure of $\text{Ag}_x\text{Au}_{1-x}$ alloys, showing empty states (> 0 eV) and the d bands (< 0 eV). The color scale refers to the weighted contribution of Ag (red) and Au (black) to each state.

Moreover, we identify the contribution of each metal to the overall band structures: the color scale in Figure 4.10 represents the weight of the pure constituents on each k -dependent electronic state. For example, in $\text{Ag}_{0.50}\text{Au}_{0.50}$ alloy Au dominates most of the high-energy states in the d band from -2 to -3 eV, see Figure 4.10c, while Ag and Au have comparable contributions on other states across all the critical points of the Brillouin Zone (reference to Figure 4.11 for the positions of Γ , R, X, and M). This non-linear behavior is a direct consequence of the fact that the energy of the d band of Au is ~ 1.6 eV higher than Ag.

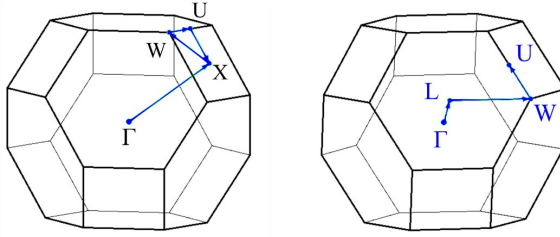


Figure 4.11: Illustration of critical points and the symmetric paths (blue) in the Brillouin zone along which the band structures were calculated using density functional theory.

Here, we report a class of metallic materials based on $\text{Ag}_x\text{Au}_{1-x}$ with tunable optical response, where we vary the alloy chemical composition to engineer its optical dispersion relation. We attribute the tuning of the SPP dispersion relations to a change of the band structure resulting from alloying, which is theoretically confirmed by DFT calculations. Valence band analysis reveals that the optical resonance variation is directly related to a shift of the d band position, which is tuned by varying the chemical composition. Note that our combined analysis can be expanded to other binary mixtures of metals, such as Au-Cu and Al-Mg, for low-loss optical devices that operate in the near-infrared and ultraviolet-visible range of the electromagnetic spectrum, respectively. By calculating the band structure of combined metallic elements, one can establish a library of possible mixtures with predictive optical/electronic response that are currently not available. In turn, this data could be used as a guideline for identifying the ideal combination of metals for applications ranging from (photo)electrocatalysts to superabsorbers and hot carrier devices [168, 189–191].

4.4 Experimental Methods

4.4.1 Sample Fabrication

The metallic alloyed thin films were fabricated by cosputtering of Ag (99.99%) and Au (99.99%). Before the deposition, the glass substrates were cleaned with acetone, isopropanol, and de-ionized water, and then dried with N₂. The samples were rotating at 8 rpm during deposition to ensure uniform chemical composition across the entire glass substrate.

4.4.2 Energy-dispersive X-ray Spectroscopy

The chemical composition of the Ag_xAu_{1-x} films was analyzed by energy-dispersive X-ray spectroscopy (EDS). The results presented in Table 4.1 are the average of three representative point measurements, each acquired on a 20 × 20 μm² area of the sample.

4.4.3 Reflection and Transmission Spectra

The reflection and transmission spectra were acquired by a variable-angle spectroscopic ellipsometer. We recorded the reflection spectra at the incident angles (with respect to the surface normal) of 55, 60, 65, 70, and 75°, respectively. For transmission measurements, air was used as the baseline. We utilized a B-spline model to fit both reflection and transmission simultaneously to extract the permittivity for each pure metal and the metallic alloys. We determined the film thicknesses

by fitting it as a variable during the ellipsometry modeling, see Table 4.1 for the results. The transmission spectra were calculated using Fresnel equations.

4.4.4 Reflectivity Maps

The reflectivity of the films was measured using the Kretschmann configuration. A supercontinuum laser was used as the light source and the laser passed through a half-wave plate to select the *p*-polarized light. A fused silica prism was attached to the glass substrate using an index matching liquid, and placed on a rotation stage. The reflection power was then recorded using a silicon photodiode at each wavelength and incident angle and divided by the corresponding power of the incident light to determine the reflectivity.

4.4.5 Valence Band Measurement

X-ray photoelectron spectroscopy (XPS) was used to acquire the valence band spectra (VBS) of Ag-Au alloyed samples of various compositions using a monochromated Al-K α X-ray source (1486.6 eV), and all scans were performed with a 45° take-off angle. The surfaces of all samples were neutralized with a combination of a barium oxide electron neutralizer, and a low voltage (10 V) argon ion beam in neutralization mode. High resolution elemental transition scans were performed with a 100 μ m X-ray beam size, with a power of 25 W, and a pass energy of 55.0 eV. Relative sensitivity factors were calibrated with Ag, Au, and Cu standards prior to testing [192]. All spectra were shifted based on the adventitious carbon C1s transition set to a binding energy of 284.8 eV. Also, all spectra were averaged over two

cycles per scan region. VBS fitting was performed with commercial software. A Shirley background was subtracted in each region to remove noise signal and peaks were fit using Gaussian shape factors. The valence region was fit with Gaussian curves with the peak locations and fit parameters of the remainder being regarded as residual non-physical information.

4.4.6 Density of States Calculation

Plane-wave density of functional theory (DFT) calculations were carried out using the CASTEP code [193]. Geometry optimizations were performed with the BFGS minimization algorithm for $2\times 2\times 2$ supercells of Ag, Au and different Ag-Au combinations [194]. The Perdew-Becke-Ernzerhof (PBE) functional in the generalized gradient approximation (GGA) was adopted with a relativistic and spin-unrestricted formalism [195]. For all calculations, ultrasoft Ag and Au pseudopotentials were employed with a plane-wave basis energy cut-off of 360 eV. The electronic minimization was achieved with a Pulay density mixing scheme and converging the total energy per atom to less than 5×10^{-7} eV. The Monkhorst-Pack scheme was utilized with a $10\times 10\times 10$ k -point grid size for Brillouin Zone sampling [196]. The total and partial projected DOS were obtained for all optimized supercells for both gaussian smearing and eigenvalue interpolation. The eigenvalues and partial weights were interpolated onto a k -point grid of $200\times 200\times 200$ with instrumental broadening of 0.1-0.3 eV.

4.4.7 Element-projected Band Structure Calculations

DFT calculations using SIESTA [188] were performed on a 4-atom supercell for $\text{Ag}_x\text{Au}_{1-x}$ with $x=0, 0.25, 0.50, 0.75, 1.00$. For all calculations the PBE flavor of GGA was used for the exchange and correlation potential. Norm conserving relativistic pseudopotentials, a real space mesh with an energy cutoff of 400 Ry, and up to 30 k points in each direction within the Monkhorst Pack scheme were employed throughout. Albeit those transitions are not well described by ground state DFT, the position of the occupied d orbitals with respect to the Fermi level are well characterized in the case of noble metals such as Au and Ag.

4.5 Conclusions

In conclusion, we experimentally and theoretically mapped the optical dispersion for $\text{Ag}_x\text{Au}_{1-x}$ alloyed thin films. By varying the content of Ag and Au, the SPP properties of this metallic material were finely tuned in the visible range of the electromagnetic spectrum. To corroborate our results, we collected the VBS through XPS measurements and deconvoluted the contribution from the d band to the DOS. We found that the shift in energy of the d band aligns very well with the transmission peak of the alloy. The degeneracy of the $d_{5/2}$ and $d_{3/2}$ bands is broken as we increase the content of Au in the film. Further, the band structure calculated by DFT is in good agreement with optical and VBS results when determining the threshold of the interband transition, showing a shift to longer wavelength of the interband transition when Au content increases. Overall, our results helped ex-

plaining the electronic and optical properties of new metallic materials and provide the potential for the fabrication of scalable, low-cost thin films for surface dispersion engineering. Given that a thorough understanding of the band structure and the optical response allows a systematic method to obtaining metallic materials with tunable optical response, we foresee that our work will be useful to advance materials selection for a wide range of applications including, but not limited to, photoelectrochemical water splitting [197], superabsorbers [97], metasurfaces [198], and active plasmonic devices [199].

Chapter 5: Al-Cu/Si for Lithography-free Thin-film Superabsorbers

Summary: Superabsorbers based on metasurfaces have recently enabled the control of light at the nanoscale in unprecedented ways. Nevertheless, the subwavelength features needed to modify the absorption band usually require the implementation of complex fabrication methods, imposing severe constraints to their practical applications.

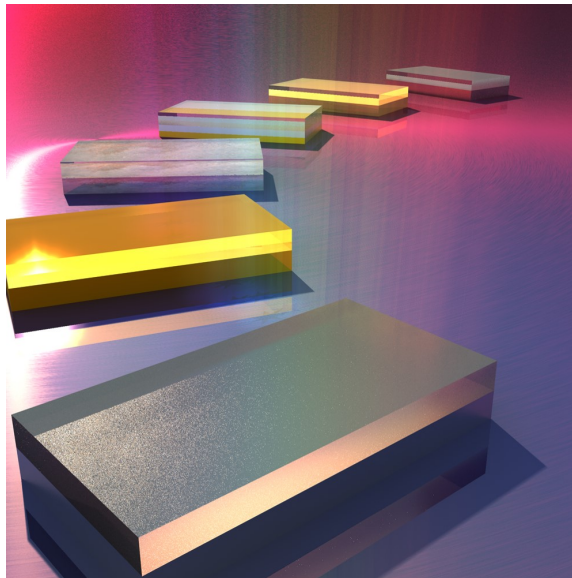


Figure 5.1: Illustration of thin film superabsorbers.

To overcome the scalability limitations associated with the fabrication of metallic nanostructures, we propose to engineer the optical response of superabsorbers by metal alloying, instead of tuning the geometry/size of the nanoscale building blocks. We numerically demonstrate the superior performance of thin film AlCu alloys as the metallic component of planar bilayer superabsorbers. Our calculation presents a Si/AlCu structure with $> 99\%$ absorption at selected wavelength ranging from the visible to the NIR regions of the spectrum, depending on the thickness of the semiconductor layer. Additionally, we validate our findings by fabricating and testing a-Si/AlCu superabsorbers, where we find good agreement between the numerically and experimentally determined optical response. The system investigated here is relevant for integration in complementary metaloxide semiconductor (CMOS) technologies. This chapter is adapted from the following reference [97].

5.1 Introduction

Building blocks that perfectly absorb electromagnetic radiation from UV to radio frequency (RF) have direct applications in thermal emission and detection [200, 201], thermoelectronics and thermophotovoltaics [202–204], sensors [26], and radar and stealth technology [205, 206]. Superabsorbers (also termed perfect absorbers) are artificially constructed materials (or metamaterials) that present a resonance that corresponds to near unity absorbance over a single, multiple, or broadband frequency of the electromagnetic spectrum. The ultra-high light absorption is obtained due to an impedance match between the material and the medium [30]. Here, the electric and magnetic resonances are designed so that the bulk effective impedance is equal to the one of the free space (air or vacuum). As a result, most of the incident light is absorbed and the reflection is negligible. Salisbury [207] and Dallenbach [208] first idealized classical absorbers to operate in the microwave range of the electromagnetic spectrum. The former included a resistive layer located at a quarter wavelength from a metallic substrate while the latter consisted of a dielectric layer on top of a metallic substrate.

In the past two decades, advances in nanofabrication have given rise to nanostructures with controlled geometry, recently inspiring the design of metamaterials and metasurfaces for superabsorbers [209]. With the flexibility of tuning nanostructures geometry and periodicity, such absorbers have been demonstrated in the visible [210, 211], NIR [212], mid-infrared (MIR) [213] and far-infrared (FIR) [214, 215] frequency ranges, proving to be a powerful approach for producing optical responses

that are not feasible by any conventional material. However, the cost of the current fabrication methods limits their commercial applications. For instance, metasurfaces consisting of arrays of nanostructures on a dielectric surface are difficult to manufacture through physical deposition approaches in large scale even by using state-of-the-art bottom-up nanolithography methods.

To overcome the scalability constraints of the fabrication methods currently implemented for metasurfaces, the use of thin films in superabsorbers has been explored for a broad range of the spectrum, extending from visible to the FIR [99, 101, 216–223]. The Dallenbach configuration provides significant benefits regarding the fabrication of ultrathin, planar, omnidirectional and polarization independent structures with very high absorption. Recently, it was reported that more than 98% of the normally incident light could be absorbed in an ultrathin layer of Ge on top of Ag at a wavelength (λ) of 625 nm, decreasing to 80% for incident angles up to 66 degrees for both polarizations [101]. In addition, highly doped Si has been used as a metallic-like substrate under a thin Ge layer to absorb light in the MIR, where the doping concentration in Si was the knob to engineer its dielectric function [221]. Further, GaAs on Au has been experimentally reported to absorb 96% of incident light at $\lambda = 38$ m [222].

To control the range of operation of metallic thin films and nanostructures for nanophotonics, alternative materials and geometries have been recently considered, such as metal alloys, transparent conducting oxides, transition metal nitrides, yttrium hydride, semiconductors, among others [11, 96, 128, 130, 224, 225]. Specifically, the alloying of metals has allowed materials with optical responses unachievable

by the individual metal components [11]. Imminent material options for on-chip nanophotonics rely on metals like Al and Cu due to their fully CMOS compatibility and low-cost/earth abundance. These metals have well-defined permittivity with absorption at $\lambda = 460$ nm and $\lambda = 600$ nm, respectively. Therefore, mixing them could provide thin films with adjustable permittivity that complement the thin semiconductor layer for near-unity absorption in the thin film configuration.

Here, we demonstrate by analytic calculations and numerical simulations that near-unity absorption ($> 99\%$) is achieved in a bilayer planar configuration superabsorber composed of an alloyed metallic layer (with nominal composition of $\text{Al}_{0.5}\text{Cu}_{0.5}$ or AlCu) and a semiconductor (Si, Ge, and GaAs). Using the transfer matrix method (TMM), we perform a quantitative and comparative analysis of the optical response of different metals, including Ag, Au, Cr, Al, Cu, and AlCu. We find that AlCu substantially outperforms those pure metals commonly used in photonics. The Si/AlCu system supports Brewster modes, where the high absorption resonance peak can be finely tuned from the visible to the NIR by simply varying the thickness of the semiconductor layer. Furthermore, we find that the planar structure of Si/AlCu is a dual-band superabsorber with the first and second modes in the NIR and the visible regions of the electromagnetic spectrum, respectively. As desired, the high absorption is independent of the polarization and spans a large oblique angle of the incident light. Additionally, by increasing the value of the index of refraction of the surrounding medium, the absorption maxima blue shifts while changing between optical modes. Finally, as a proof of concept, we fabricate a-Si/AlCu thin film superabsorbers and demonstrate that a single and dual-band near-unity ab-

sorption is obtained by adjusting the semiconductor thickness, in agreement with our simulations. Our results reveal the potential of thin film metal alloys in future nanophotonic applications, spanning from integrated optical circuits to sensing devices and thermophotovoltaics.

5.2 Materials Selection for Near-unity Absorption

A schematic illustration of the thin film superabsorbers investigated here is presented in the top row of Figure 5.2. The thin film thicknesses considered are d (variable) and $h = 100$ nm for the Si top and the metallic bottom layers, respectively. Here, we choose Si as the semiconductor because of its CMOS compatibility. Also, the band gap energy of Si (at 1117 nm) lies in the NIR, enabling us to access the optical response of the absorber stack for energies lower than the semiconductors band gap, where light is absorbed by the metal alloy (a process that is assisted by the refractive index contrast between Si and AlCu). We first compare the absorption profile of superabsorbers with adjustable Si thickness and using Ag, Au, Cr, Al, Cu, as well as AlCu. The permittivity (see Figure 5.3) of all metals is obtained experimentally by ellipsometry measurements from thin film samples fabricated by sputtering. Figure 5.4 shows the raw data of ellipsometry measurements and Table 5.1 displays the chemical composition analysis of the AlCu film. To minimize the contribution of metal oxidation due to air exposure, we perform the ellipsometry measurements immediately after the deposition of the thin films.

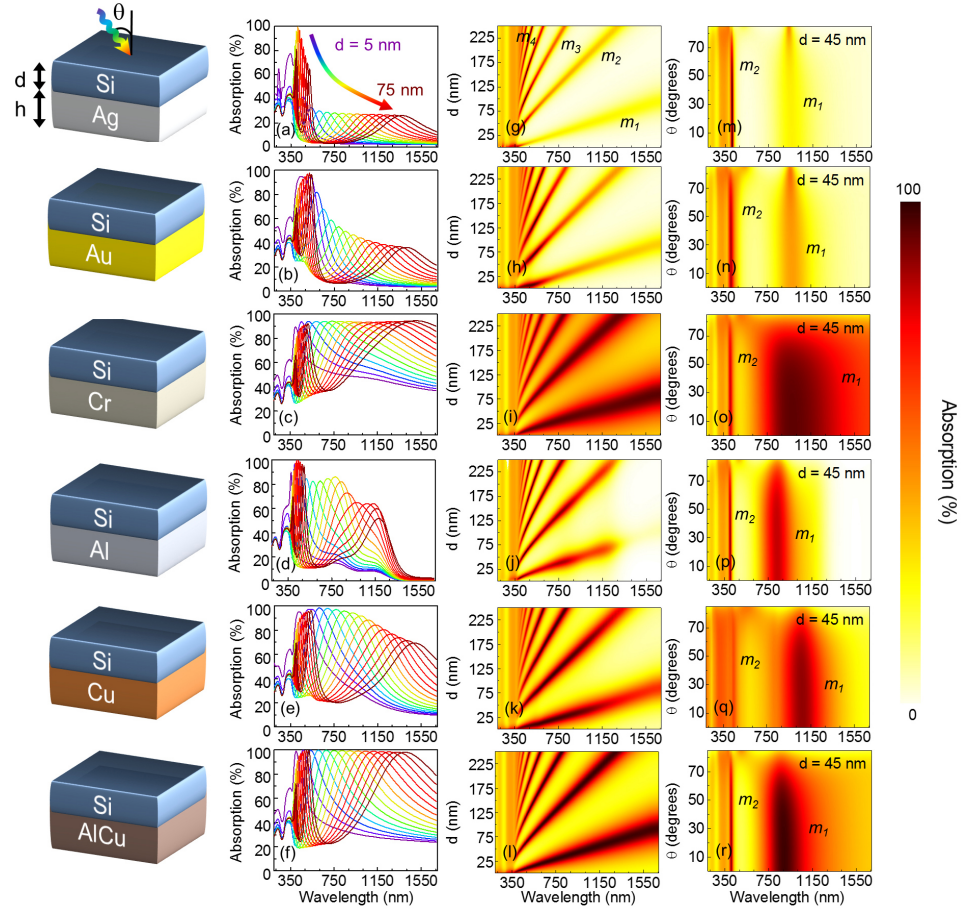


Figure 5.2: Top row: schematic of the bilayer structure, where $h = 100$ nm and d are the thicknesses of the metallic thin film (Ag, Au, Cr, Al, Cu, AlCu) and the Si layer, respectively. θ is the angle of the incident light from the air. (a-f) Calculated normal incidence absorption spectra as a function of d (color-coded). (g-l) Calculated normal incidence absorption maps as a function of d showing optical modes (m_i). (m-r) Calculated absorption maps as a function of θ (here, $d = 45$ nm).

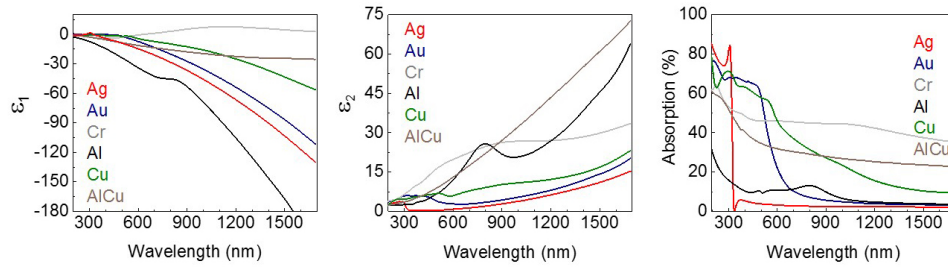


Figure 5.3: (Left) Real (ϵ_1) and (middle) imaginary (ϵ_2) parts of the permittivity, obtained by ellipsometry measurements. (right) Absorption spectra of silver (Ag), gold (Au), chromium (Cr), aluminum (Al), copper (Cu), and AlCu alloy, calculated with thickness of 100 nm.

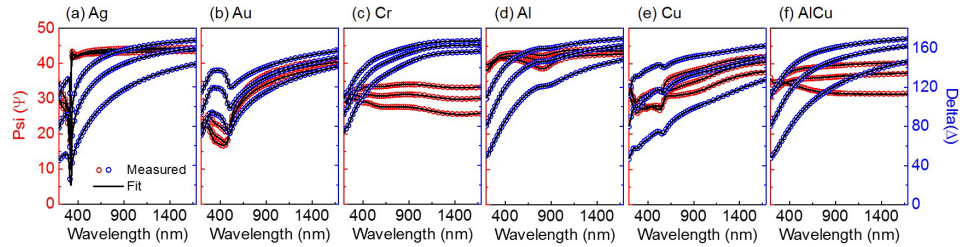


Figure 5.4: (a-f) Raw ellipsometry measurements for metallic thin films. Here, Psi (Ψ), open red circles and Delta (Δ), open blue circles, were obtained from combined transmission (when applicable) and reflection measurements at 60, 65 and 70 degrees. The solid lines correspond to their fit, obtained by a B-spline model enforcing Kramers-Kronig relation. Film thickness: 40 nm. Substrate: glass.

Table 5.1: Chemical composition obtained from EDS point measurements on 3 representative regions for the AlCu thin film.

Location	Al (at%)	Cu (at%)
1	55	45
2	55	45
3	55	45
Average	55	45

The absorber with the alloyed metallic layer outperforms all stacks containing pure metals with a remarkably higher absorption peak for a broad range of Si thicknesses, as displayed in Figure 5.2a-f. Then we compare the absorption using both the experimentally obtained permittivity and Paliks data (see Figure 5.5). The absorption profile within the semiconductor/metal alloy stack is presented in Figure 5.6, and shows strong light absorption in the AlCu layer, beyond the bandgap of Si, as expected. For the analysis of the first absorption resonant mode (m_1), we consider the normal incidence absorption spectra as a function of $d = 5$ to 75 nm (color-coded). In all cases, m_i redshifts as the film thickness d increases. Au has an absorption maximum of 94.85% for $d = 10$ nm. The overall absorption of the noble metals lowers in the NIR range of the spectrum for thicker Si films (> 40 nm). For Cr, the absorption peak of the superabsorber slightly increases in the NIR, reaching its maximum value (94.56%) at $d = 75$ nm. Despite the fact that Si does not absorb beyond its band gap, its n value allows a resonance due to the non-trivial

phase shift at the interface between Si and Cr, enhancing the overall absorption of the stack [226]. Pure Al and pure Cu present an absorption maximum of 97.07% and 98.50% in the visible range of the spectrum for $d = 10$ nm and 15 nm, respectively, see Figure 5.2d and 5.2e. The superabsorber containing AlCu clearly holds the maximum absorption over a wide range of the electromagnetic spectrum. From $d = 5$ nm to 75 nm, $> 98.16\%$ of the light is absorbed, spanning visible to NIR wavelengths - as shown in Figure 5.2f. We attribute the unique optical response of the AlCu alloy in the NIR to a change in the band structure of the material [227]. In addition, it is likely that the small grains composing the film and their boundaries lead to increased absorption [228, 229]. Thus, as a consequence, the permittivity's imaginary part presents a higher value than the pure metals (see Figure 5.3).

Figure 5.2g-l presents the normal incidence absorption maps as a function of d , where four distinct modes (m_i , $i = 1$ to 4) are identified. As expected, for Au and Ag all modes with high absorption values are restricted to the visible range of the electromagnetic spectrum while decaying drastically over the NIR. Cr extends its high absorption response of m_1 and m_2 from the visible to the NIR (see Figure 5.2i). Al and Cu present a comparable behavior to noble metals in the visible while decaying modestly in the NIR. Figure 5.7 shows a quantitative comparison between the absorption maps of bare Si and the Si/metal stacks. Note that AlCu and Cr have similar characteristics: both extend their high absorption responses of m_1 and m_2 from the visible to the NIR (Figure 5.2l and 5.2i). Nevertheless, AlCu retains near-unity absorption ($> 99\%$) from $\lambda = 409$ nm ($d = 5.5$ nm) to $\lambda = 1016$ nm ($d = 47.6$ nm). Moreover, for d between 60 nm and 75 nm both

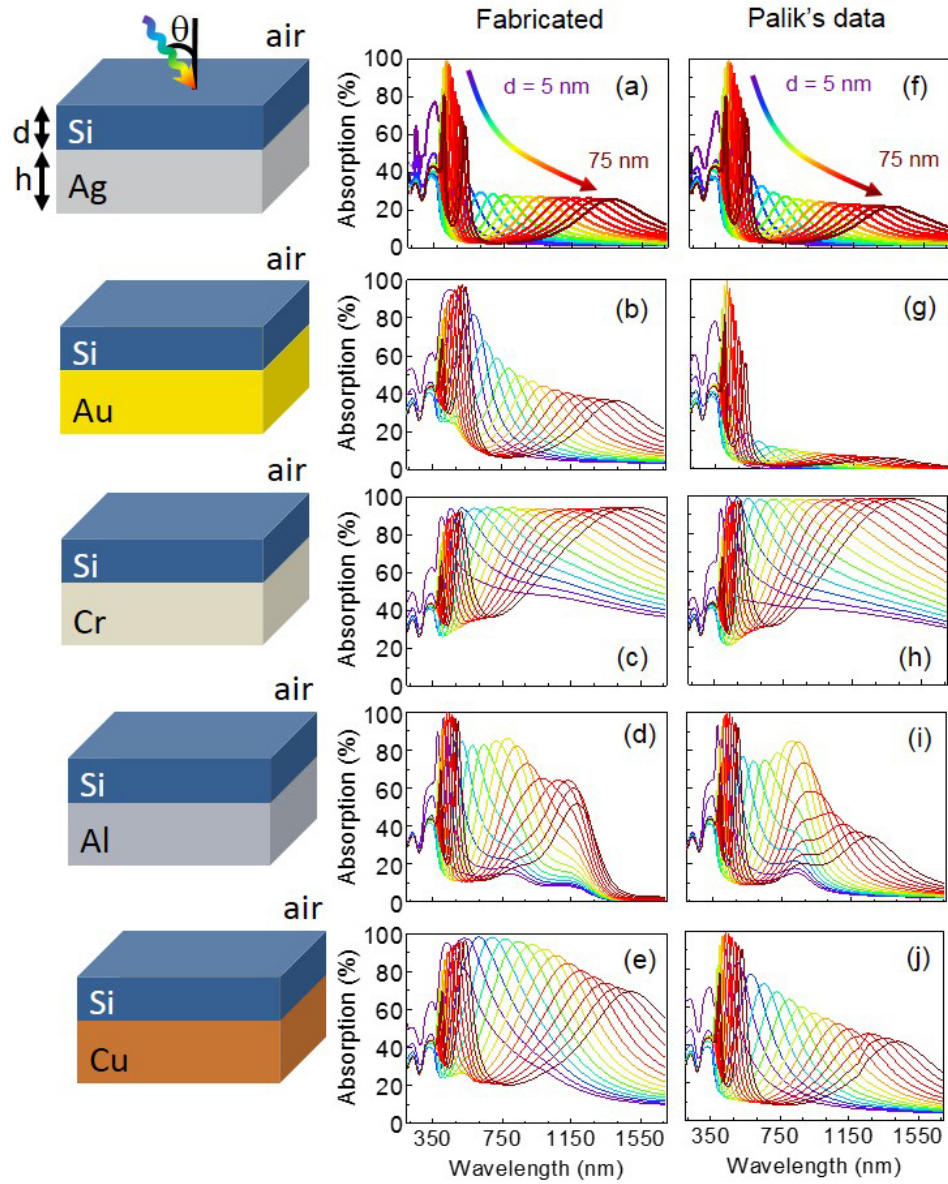


Figure 5.5: Calculated absorption spectra for Si/metal superabsorbers as a function of d . (a, f) Ag, (b, g) Au, (c, h) Cr, (d, i) Al, and (e, j) Cu metallic layer, using experimentally determined permittivity for the metals (fabricated) and Paliks data.

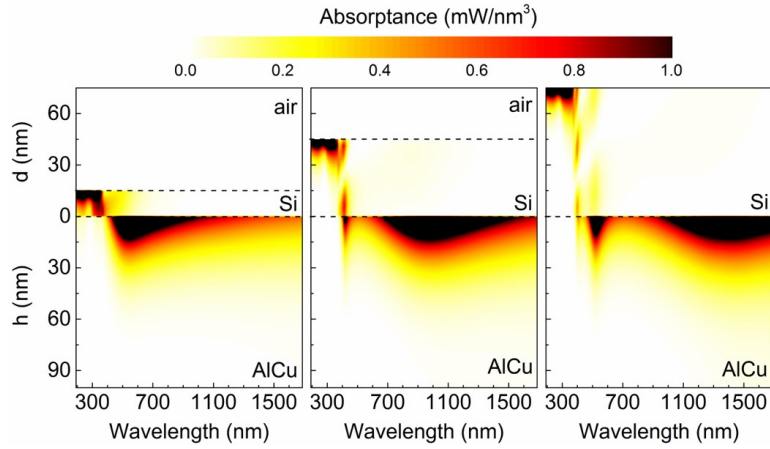


Figure 5.6: Cross-section profile simulations of normal incidence absorptance for a 100 nm AlCu film underneath a Si layer with thickness d equal to 15 nm, 45 nm, and 75 nm.

modes, m_1 and m_2 , have its absorption $> 98.60\%$, making this structure a dual-band superabsorber with one peak in the visible and another in the NIR. Similarly, for Ge and GaAs, near-unity absorption can also be obtained (see Figures 5.8, 5.9, 5.10, 5.11 and 5.12). Commonly, a dual-band absorber is achieved by designing arrays of nanostructures [230]. The origin of the optical response of AlCu lies on both real (ϵ_1) and imaginary (ϵ_2) parts of the permittivity. The low magnitude of $|\epsilon_1|$ over the entire spectrum is responsible for the strength of dynamical screening effects which, in combination with the large value of ϵ_2 (especially in the NIR), leads to a high absorption of AlCu. One advantage of the planar configuration for superabsorbers is the wide oblique angular tolerance of its resonant peak [209]. Figure 5.2m-r displays the absorption maps as a function of the incident angle (θ) of an unpolarized light for $d = 45$ nm. Ag and Au have an inferior response for the mode m_1 , absorbing $< 45\%$ of light in the NIR. However, for the mode m_2 , \sim

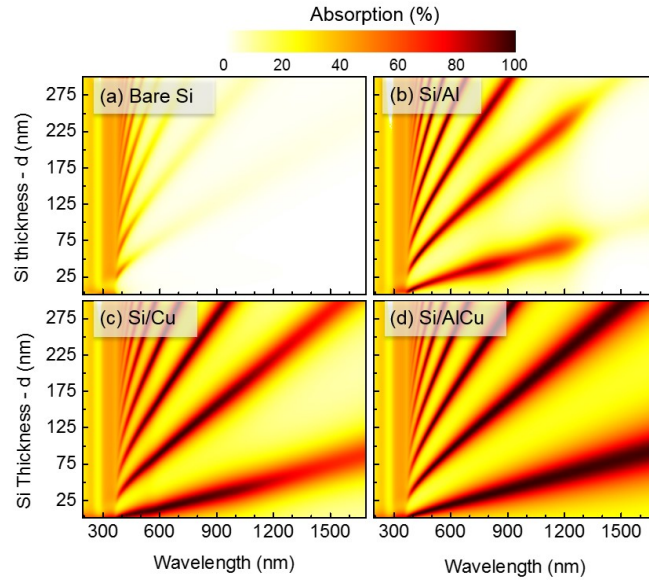


Figure 5.7: Calculated normal incidence absorption maps as a function of the top layer thickness (d) and incident wavelength for (a) bare Si and 100 nm of (b) Al, (c) Cu and (d) AlCu underneath Si.

98% and $\sim 84\%$ is absorbed in the visible for Ag and Au, respectively. The angle dependent maps for Cr, Al, Cu, and AlCu show that the characteristic peaks m_1 and m_2 remain high for a large θ (≥ 70 degrees). The superior performance of the system containing the AlCu alloy strongly indicates its potential application in CMOS-compatible superabsorbers.

We quantitatively compare the absorption maps of Si/metal stacks with an arbitrary index of refraction

$$\tilde{n} = n + ik \quad (5.1)$$

for the metal; see Figure 5.13, where the selected wavelengths refer to the maximum absorption for the Si/AlCu stack with different semiconductor thickness shown in Figure 5.2a-f. We find that the stack with the AlCu alloy outperforms the ones

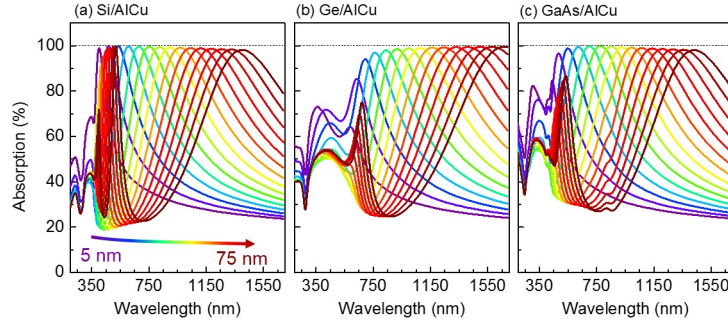


Figure 5.8: Calculated absorption spectra of thin film superabsorbers formed by (a) Si, (b) Ge, and (c) GaAs, with a 100 nm AlCu bottom layer. The thickness of the semiconductor varies from 5 to 75 nm, as color-coded.

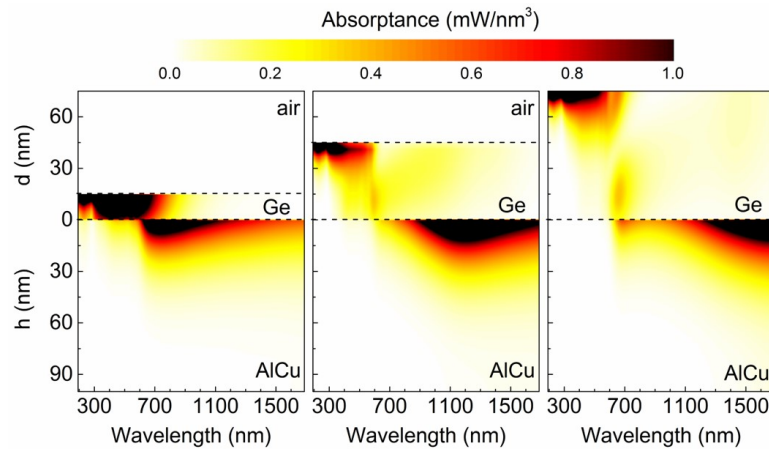


Figure 5.9: Cross-section profile simulations of normal incident absorptance for a 100 nm AlCu film underneath a Ge layer with thickness d equal to 15 nm, 45 nm, and 75 nm.

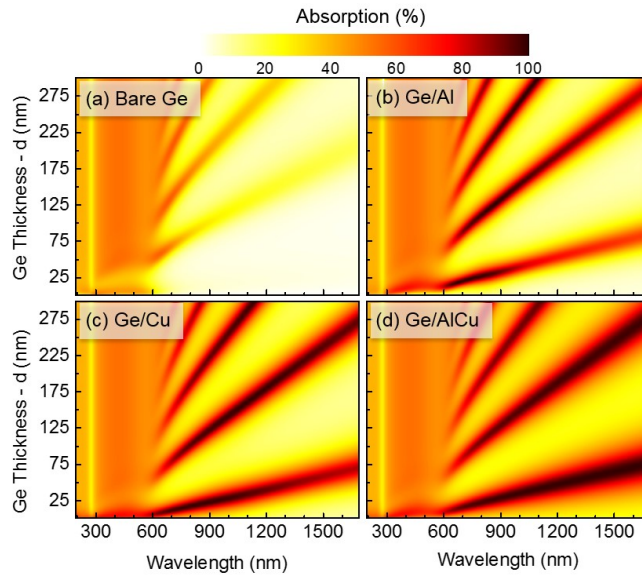


Figure 5.10: Calculated normal incident absorption maps as a function of the top layer thickness (d) and incident wavelength for (a) bare Ge and 100 nm of (b) Al, (c) Cu, and (d) AlCu underneath Ge.

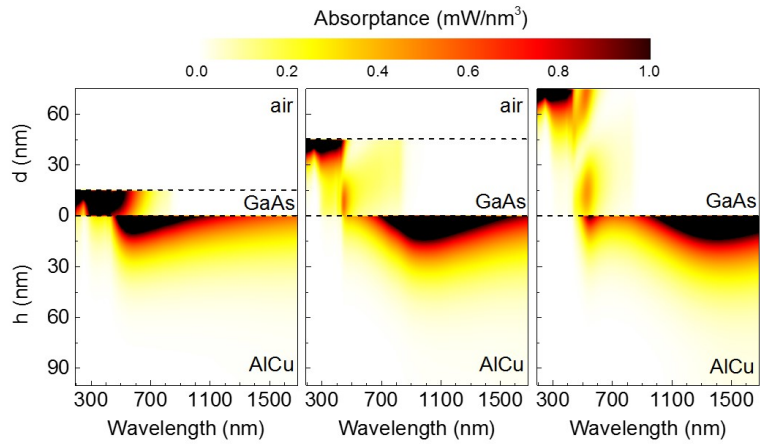


Figure 5.11: Cross-section profile simulations of normal incident absorptance for a 100 nm AlCu film underneath a GaAs layer with thickness d equal to 15 nm, 45 nm, and 75 nm.

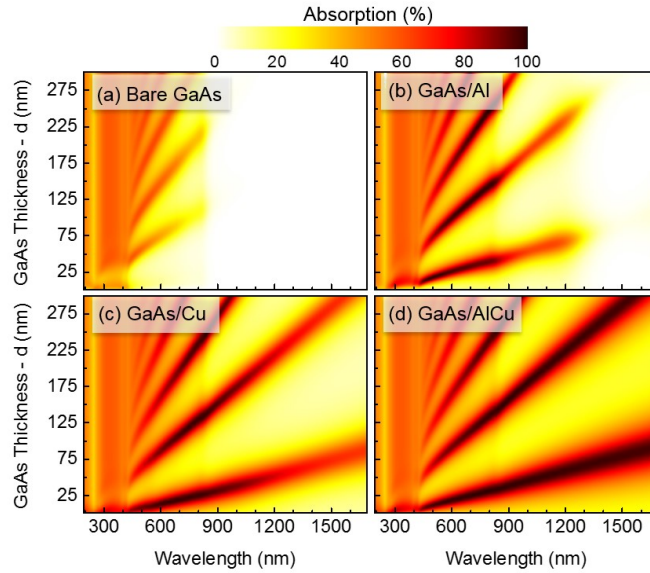


Figure 5.12: Calculated normal incident absorption maps as a function of the top layer thickness (d) and incident wavelength for (a) bare GaAs and 100 nm of (b) Al, (c) Cu and (d) AlCu underneath GaAs.

formed by pure metals whenever the thickness of the semiconductor is ≥ 15 nm. The symbols in Figure 5.13 correspond to the refractive indices of Ag, Au, Cr, Al, Cu, and AlCu. In our calculations we consider an optimal thickness of $h = 100$ nm for the metallic layer in order to eliminate the transmission signal of the system (see Figures 5.14 and 5.15 for details); thus, the performance of each metal can be independently evaluated. For all cases, AlCu offers the best alternative from all metals investigated. Figure 5.16 displays the performance of potentially CMOS-compatible metals in a Si/metal stack. Figure 5.13a presents the results for a Si film thickness $d = 5$ nm at wavelength $\lambda = 400$ nm. Here, AlCu is the only material that fulfills the condition of near-unity absorption, where the maximum absorption is 98.99%. Figure 5.13b corresponds to $d = 15$ nm at $\lambda = 536$ nm with

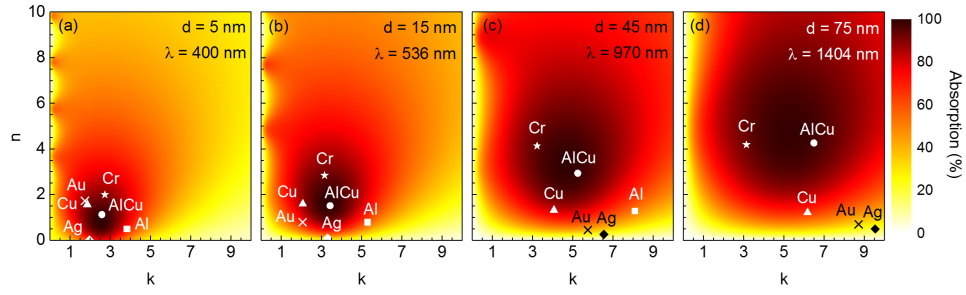


Figure 5.13: The performance of Ag, Au, Cr, Al, Cu, and AlCu are represented by a given symbol. The top Si layer has a variable thickness d of (a) 5 nm, (b) 15 nm, (c) 45 nm, and (d) 75 nm. The bottom layer is fixed at 100 nm. The selected wavelengths refer to the maximum absorption of the Si/AlCu for each semiconductor thickness.

an absorption maximum of 99.74%. Likewise, for $d = 45$ nm at $\lambda = 970$ nm, AlCu presents maximum absorption of 99.13% (Figure 5.13c). Finally, for $d = 75$ nm at $\lambda = 1404$ nm, AlCu (98.16%) and Cr (92.92%) present comparable performance with high values for the absorption, as shown in Figure 5.13d.

5.3 Superabsorbers: Simulation and Experiment

To assess the possible effects of angle and light polarization on the optical response of the Si/AlCu system, we deconvolute these parameters by calculating the absorption profile for three different Si thicknesses. The planar configuration containing AlCu exhibits near-unity absorption that is insensitive to the incident angle and polarization, a desired feature for emitters and sensors. Figure 5.17 displays the absorption maps as a function of θ and λ for $d = 15$ nm (Figure 5.17a-c), 45 nm (Figure 5.17d-f), and 75 nm (Figure 5.17g-i). In all cases, the absorption peak corresponding to m_1 remains high over a large incident angle range. At ~ 50

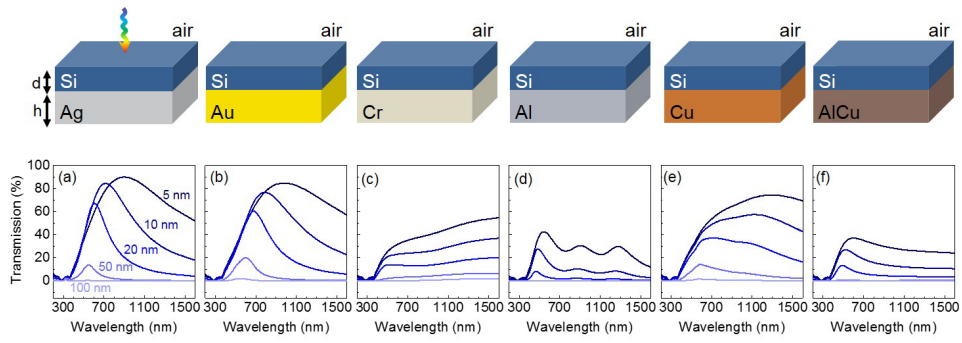


Figure 5.14: (a-f) Calculated normal incidence transmission spectra of Si/metal superabsorbers. Metallic film thicknesses: $h = 5, 10, 20, 50,$ and 100 nm. Si thickness $d = 15$ nm. Note that the transmission completely vanishes for $h = 100$ nm.

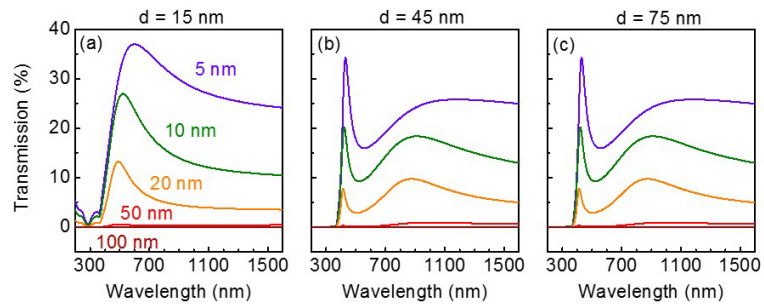


Figure 5.15: Calculated normal incidence transmission spectra of Si/AlCu thin film with Si thickness d equal to (a) 15 nm, (b) 45 nm, and (c) 75 nm. The thickness of AlCu is $h = 5, 10, 20, 50,$ and 100 nm.

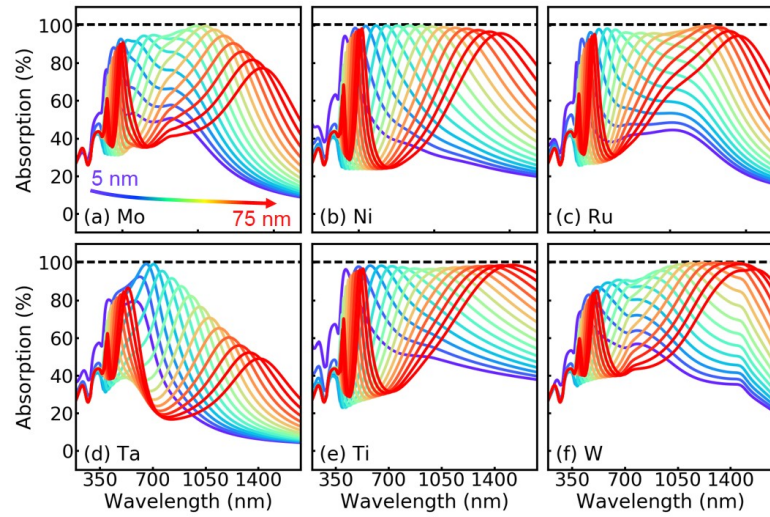


Figure 5.16: Calculated absorption spectra of thin film superabsorbers formed by Si on top of a 100 nm (a) Mo, (b) Ni (c) Ru, (d) Ta, (e) Ti, and (f) W layer, all potentially CMOS-compatible metals. The thickness of the semiconductor varies from 5 to 75 nm, as color-coded. Paliks data was used for the permittivity of Si, Mo, Ni, Ru, Ti and W. Data from CRC handbook of Chemistry and Physics was used for Ta.

degrees, 95% of the unpolarized light continues to be absorbed, decreasing slightly to 80% at ~ 70 degrees (Figure 5.17a, d, and g).

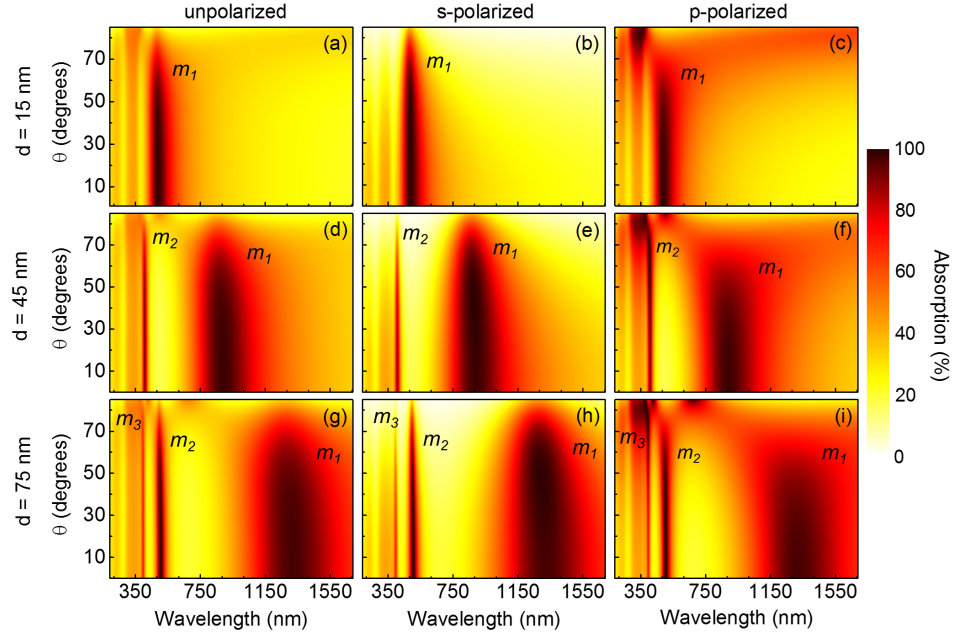


Figure 5.17: Polarization dependent absorption maps calculated as a function of incident angle θ and wavelength for 100 nm AlCu metallic film coated with (a-c) 15 nm, (d-f) 45 nm, and (g-h) 75 nm Si films.

For oblique incidence, the *s*- and *p*-polarized light exhibit different responses. For *s*-polarized light, the mode m_1 presents $> 95\%$ absorption for θ up to ~ 60 degrees (see Figure 5.17b, e, and h, respectively). For *p*-polarized light, the features are considerably different for the three Si thicknesses considered. Figure 5.17c corresponds to $d = 15$ nm, where the absorption of m_1 persists high for θ up to 41 degrees ($> 95\%$) while for $\theta > 81$ degrees m_2 ($\lambda \sim 345$ nm) exceeds this value ($> 98\%$). Figure 5.17f shows the characteristics of $d = 45$ nm, where more than 95% of the incident light is absorbed over 35 degrees, while for $\theta \geq 40$ degrees the absorption

maximum blue shifts to m_2 ($\lambda \sim 193$ nm). Finally, Figure 5.17i displays the high absorption for $d = 75$ nm corresponding to m_1 ($\lambda \sim 310$ nm) over 24 degrees, to m_2 up to 50 degrees ($\lambda \sim 504$ nm), and to m_3 for $64 < \theta < 84$ degrees ($\lambda \sim 395$ nm). These results illustrate the effective high performance of the semiconductor/metal alloy model system investigated here, including in situations where incident light is oblique, applicable for thermophotovoltaics and bolometers.

Motivated by the multi-wavelength near-unity absorption behavior of the Si/AlCu system, we discuss in Figure 5.18 the effect of the surrounding media on the absorption characteristics of the superabsorber. For all semiconductor thicknesses considered, at normal unpolarized incident light, the absorption maximum of Si/AlCu blue shifts while increasing the index of refraction (n), changing from m_1 to m_2 or m_3 . Figure 5.18a shows the near-unity absorption peak gradual shift from the visible range of the electromagnetic spectrum to the UV, from $\lambda \sim 490$ nm (99.04%) to 341 nm (76.36%), for $n = 1.0$ to 2.5, respectively. Similarly, Figure 5.18b presents the absorption maximum changing from $\lambda \sim 895$ nm (98.2%) to 406 nm (99.95%) as n goes from 1.0 to 2.0 when $d = 45$ nm. Lastly, Figure 5.18c shows a transition from a dual- to a single-band superabsorber. For $n = 1$, there are two peaks with extremely high absorption, one at $\lambda \sim 1319$ nm (96.97%) and another at $\lambda \sim 506$ nm (99.93%). As n increases, the absorption peak at $\lambda \sim 397$ nm also increases, reaching a maximum of 97.25% for $n = 2.5$.

As a proof of concept, we fabricate a-Si/AlCu thin film superabsorbers. The superabsorbers surface is smooth (see Figure 5.19) and the measured transmission is at zero (see Figure 5.20). Figure 5.21 shows the measured and calculated absorption

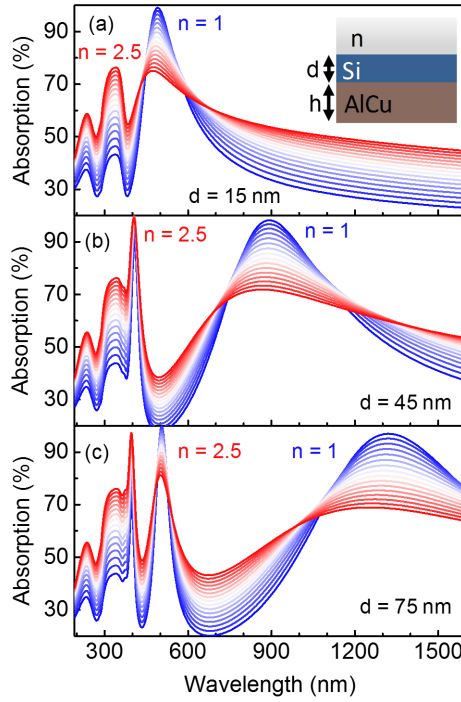


Figure 5.18: Calculated normal incidence absorption spectra of Si/AlCu with a semiconductor layer of $d =$ (a) 15 nm, (b) 45 nm, and (c) 75 nm. The index of refraction of the surrounding medium (n) varies from 1 (blue) to 2.5 (red). The inset in (a) displays a schematic of the superabsorber; out of scale for clarity.

maps as a function of θ and λ for 95 nm AlCu metallic films coated with 6 nm, 53 nm, and 94 nm a-Si. The resonant peak redshifts as the thickness of the semiconductor increases. For all cases presented here, the multi-wavelength near-unity absorption of the a-Si/AlCu system is $> 85\%$ for a wide angle of incidence. In particular for $d = 6$ nm the mode m_1 at $\lambda \sim 216$ nm spans over 40 degrees (Figure 5.21a). Likewise, for $d = 53$ nm at $\lambda \sim 645$ nm the maximum absorption goes up to 70 degrees (Figure 5.21c). For the sample with $d = 94$ nm, we obtain a dual-band superabsorber, where an absorption $> 85\%$ is maintained up to 70 degrees for the two modes ($\lambda \sim 451$

nm and $\lambda \sim 1062.3$ nm). Our experimental results are in good agreement with the calculations, where peak position, intensity and maximum angle of incidence match.

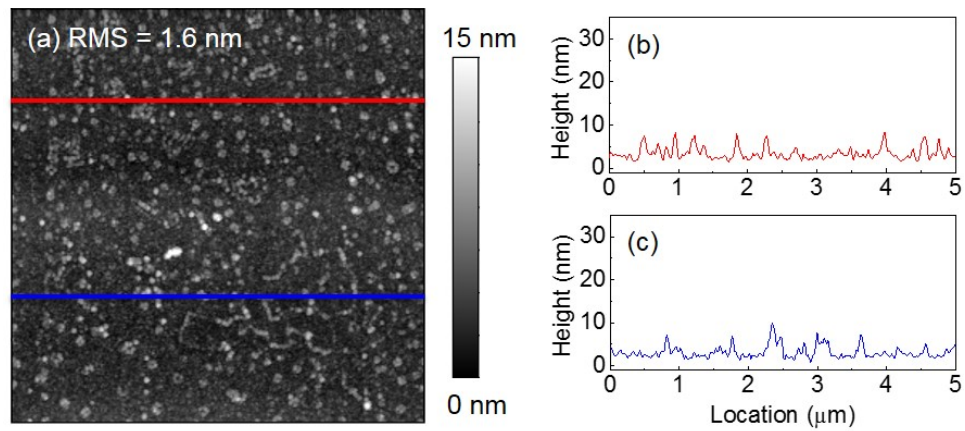


Figure 5.19: (a) AFM image and (b, c) two line profiles for 53 nm a-Si/95 nm AlCu sample showing very smooth surface.

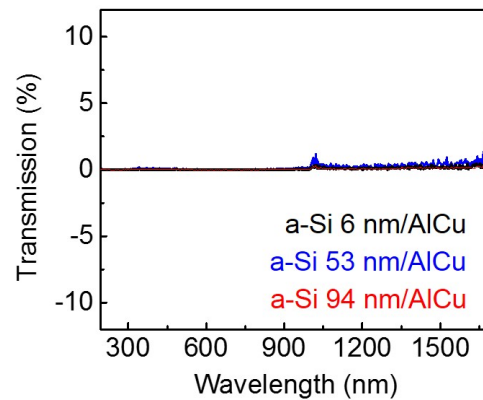


Figure 5.20: Measured transmission spectra for a-Si/AlCu samples with variable thicknesses of a-Si, and 95 nm of AlCu.

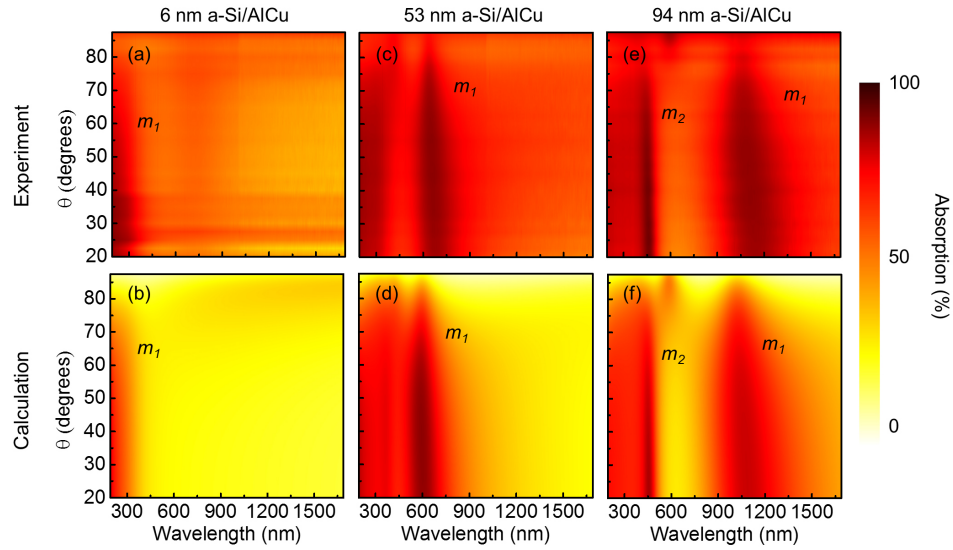


Figure 5.21: Measured and calculated absorption maps as a function of incident angle θ and wavelength for 95 nm AlCu metallic films coated with (a, b) 6 nm, (c, d) 53 nm, and (ef) 94 nm of Si.

Here, we provide a guide for obtaining superabsorption through a lithography-free, CMOS-compatible approach that can be easily scaled up. We show numerical and experimental evidence that the alloying of Al and Cu metals yields a unique permittivity, not obtained by its pure counterparts. When combined with a thin film semiconductor layer this alloy enables near-unity and multi-wavelength absorption. According to the phase diagram of Al-Cu [231], we speculate that our AlCu could be a disordered material, with lower electron mean free path when compared to both pure Al and Cu [232]. In turn, this leads to a higher value of the imaginary part of the permittivity in the NIR region for the alloy (see Figure 5.3). Thus, the combination of the strength of the polarization generated by an external electric field (small $|\epsilon_1|$) and the losses in the metal (large ϵ_2) provides the ideal condition

for tuning the wavelength of the near-unity absorption ($> 99\%$) ranging from the visible to the NIR.

5.4 Experimental Methods

5.4.1 Sample Fabrication

Ag, Au, Al, Cu, AlCu thin films were deposited by sputtering/cosputtering and Cr was deposited through thermal evaporation on glass substrates, which were cleaned with deionized water, acetone and dried with N_2 before the deposition step. The deposition rate was 5.5 nm/min for Al, Cu, and AlCu, 53 nm/min for Ag, 38 nm/min for Au, and 6 nm/min for Cr. All deposition rates were calibrated by adjusting the power of each metal source based on the film thickness determined by ellipsometry. During the deposition, the glass substrate was rotated at 8 rpm to obtain a uniform chemical composition for the thin films. Note that the fabricated Cr sample is metallic in the visible despite the presence of Cr oxide that commonly results from thin film deposition. For the superabsorber samples, a-Si was deposited on AlCu alloyed thin film and glass by e-beam evaporation at a rate of 1.5 Å/second. The sample holder was rotated at a speed of 50 rpm during the deposition. The a-Si thickness and permittivity were determined using ellipsometry.

5.4.2 Dielectric Function Model

The ellipsometry measurements were performed using a J. A. Woollam spectroscopic ellipsometer (wavelength range: 193-1680 nm) to record both reflection

and transmission spectra. The reflection measurements were acquired at 60, 65, and 70 degrees and the transmission was performed at 0 degrees (from the normal incidence). A B-spline model was applied to extract the dielectric function for each metallic thin film. For all metallic films, the mean square error (MSE) of all fits was < 6 . Ellipsometry was used to determine the thickness of the sample less than 100 nm, otherwise the thicknesses were obtained by profilometer.

5.4.3 Absorption Maps

The absorption maps were obtained based on the reflection maps by considering zero transmission for Si/AlCu stack (Figure 5.14), which were measured by ellipsometry. Baseline measurements were performed at each incident angle using a standard 25 nm SiO₂/Si wafer.

5.4.4 Elemental Analysis

The elemental analysis for the AlCu alloyed thin film was performed by X-ray dispersive spectroscopy (EDS) in a SEM system (see Table 5.1). These measurements were acquired on three $20 \times 20 \mu\text{m}^2$ representative regions of the sample, and showed a chemical composition of Al_{0.55}Cu_{0.45}. To determine the atomic ratio between Al and Cu, the quantification was performed for each location after acquiring the signals for 2 minutes and 40 seconds.

5.4.5 Transfer Matrix Method

The transfer matrix method (TMM) was used to calculate the transmission (T) and reflection (R) coefficients of an incident plane wave propagating along the z -axis through a thin layer of semiconductor on top of a metal substrate. Therefore, light absorption (A) was computed as $A = 1 - R - T$. For an optically thick film $T = 0$; and $A = 1 - R$. In this stack configuration, the field within one layer can be represented as the superposition of left- and right-traveling electromagnetic waves. Applying the proper boundary conditions, one can describe the propagation of the waves in the matrix form as:

$$\begin{pmatrix} E_{i0} + E_{r0} \\ (E_{i0} - E_{r0})\gamma_0 \end{pmatrix} = M_1 \cdot M_2 \cdot \dots \cdot M_N \begin{pmatrix} E_t \\ \gamma_t E_t \end{pmatrix} = M_{tot} \begin{pmatrix} E_N \\ \gamma_N E_N \end{pmatrix} = \begin{pmatrix} m_{11} & m_{12} \\ m_{21} & m_{22} \end{pmatrix} \begin{pmatrix} E_N \\ \gamma_N E_N \end{pmatrix} \quad (5.2)$$

where E_{i0} , E_{r0} and E_t are the incident, reflected and transmitted electric fields for a system containing N layers. For each layer j the transfer matrix is given by

$$M_j = \begin{pmatrix} \cos\delta_j & \frac{i\sin\delta_j}{\gamma_j} \\ i\gamma_j\sin\delta_j & \cos\delta_j \end{pmatrix} \quad (5.3)$$

with

$$\delta_j = \omega\tilde{n}_j d_j \cos\theta_j / c \quad (5.4)$$

$$\cos\theta_j = \tilde{n}_j^{-1} \sqrt{\tilde{n}_j^2 - \tilde{n}_0^2 \cos^2\theta_0} \quad (5.5)$$

and for TE polarization,

$$\gamma_j = \tilde{n}_j \cos\theta_j \quad (5.6)$$

and for TM polarization,

$$\gamma_j = \tilde{n}_j / \cos\theta_j \quad (5.7)$$

Thus, the reflection (r) and transmitted (t) amplitudes are written as:

$$r = \frac{\gamma_0 m_{11} + \gamma_0 \gamma_t m_{12} - m_{21} - \gamma_t m_{22}}{\gamma_0 m_{11} + \gamma_0 \gamma_t m_{12} + m_{21} + \gamma_t m_{22}} \quad (5.8)$$

$$t = \frac{2\gamma_0}{\gamma_0 m_{11} + \gamma_0 \gamma_t m_{12} + m_{21} + \gamma_t m_{22}} \quad (5.9)$$

where

$$R = |r|^2 \quad (5.10)$$

$$T = |t|^2 k_t / k_i \quad (5.11)$$

k_t and k_i are the transmitted and incident wave numbers.

5.4.6 Numerical Simulations

We used the finite-difference time-domain (FDTD) method to simulate the 3D full-field light-matter interactions, with a normally incident plane wave as the light source. A thin layer of semiconductor on top of a metal was used in the simulation space. Perfect matched layer (PML) boundary conditions were applied in the z -direction while periodic boundary conditions were used in the x - and y -in-plane directions. The broadband radiation of the plane wave light source was propagated from air into the stack with the semiconductor on the front, as shown in the

schematic of Figure 5.2. For all simulations presented here, the index of refraction of Ag, Au, Cr, Al, Cu, AlCu and a-Si was modeled through the multi-coefficient material model using transmission and reflection ellipsometry measurements of thin films as the input data. For Si, Ge, and GaAs we used data from Palik [7]. The cross-section distribution profiles of the absorptance were calculated as a function of wavelength for each simulation.

5.5 Conclusions

In conclusion, we presented a multi-wavelength, polarization-independent and wide-angle near-unity superabsorber formed by a semiconductor/AlCu metal-alloyed thin film stack. For the metallic material, we designed an alloy of Al and Cu that outperforms pure metals. A complete description of the light absorption within the stack, using TMM and numerical simulations demonstrated that ultra-high absorption ($> 99\%$) arose from the Si/AlCu system, where the peak could be finely tuned from visible to NIR by increasing the thickness of the semiconductor layer. Absorption maps of the incident angle for an unpolarized light confirmed its omnidirectionality, where 95% of light was absorbed within 50 degrees from the normal incidence angle and decreasing slightly to 80% at 70 degrees. The index of refraction of the surrounding media was found to be an efficient knob to promote the second and third optical modes with maximum absorption. Additionally, we obtained a dual-band superabsorber with a planar Si/AlCu structure, with both peaks presenting absorption $> 98\%$. To validate our predictions, we fabricated a-Si/AlCu

superabsorbers and confirmed that near-unity single- and dual-band responses are achieved by simply changing the thickness of the semiconductor layer. Superabsorbers containing an engineered AlCu metal alloy thin film could have a significant impact in applications such as sensors, photodetectors, optical filters, and radar technologies due to their high performance and straightforward scalability in size, overcoming the current challenges of incorporating nanostructures. Further, the potential compatibility with well-established CMOS fabrication processes could likely enable low-cost, mass production of nanophotonic devices incorporating these earth-abundant metal alloys. We foresee this new material as a promising alternative to modulate the optical response of active components in photonic devices. By varying the chemical composition of the alloyed metals, one can reach responses not obtained by pure elements.

Part II

All-solid-state Batteries

Chapter 6: Aluminum for All-solid-state Li-ion Batteries

Summary: The further development of all-solid-state batteries is still limited by the understanding/engineering of the interfaces formed upon cycling. Here, we correlate the morphological, chemical, and electrical changes of the surface of thin-film devices with Al negative electrodes. The stable Al-Li-O alloy formed at the stress-free surface of the electrode causes rapid capacity fade, from 48.0 to 41.5 $\mu\text{h}/\text{cm}^2$ in two cycles. Surprisingly, the addition of a Cu capping layer is insufficient to prevent the device degradation.

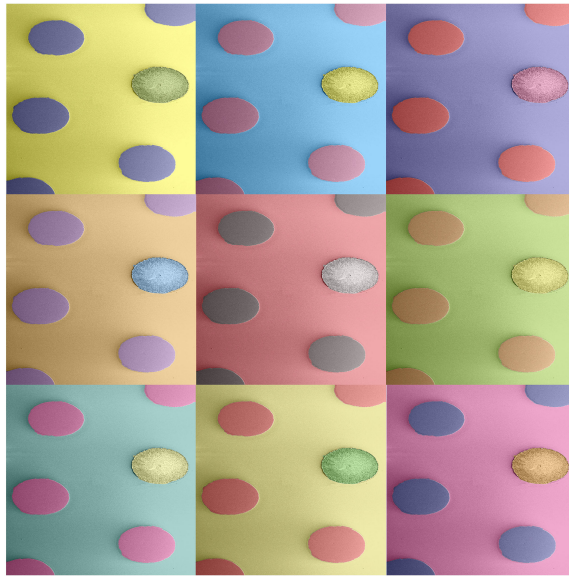


Figure 6.1: Illustration of thin-film all-solid-state batteries.

Nevertheless, Si electrodes present extremely stable cycling, maintaining > 92% of its capacity after 100 cycles, with average Coulombic efficiency of 98%. This chapter is adapted from the following reference [\[77\]](#).

6.1 Introduction

In today's society, rechargeable battery technologies with improved performance are urgently needed to address the growing power and energy demands of electric and hybrid vehicles and mobile devices [233, 234]. A promising alternative to conventional liquid electrolyte cells is the all-solid-state Li-ion battery (SSLIB), which provides (i) high power density (> 250 W/kg), (ii) long cycle life, (iii) inherent safety, due to the absence of an organic liquid electrolyte that can cause leakage and fire, (iv) lightweight and possible compact packaging, and (v) allows for a variety of materials to be implemented as the electrodes including those with higher operating voltages [78, 79, 235]. As in liquid electrolyte LIBs, in all-solid-state batteries the processes at the negative electrode (commonly denoted as the anode) during the charging step can be classified into essentially 3 different types of reaction: intercalation, conversion, or alloying [73, 236, 237]. Alloying reactions usually take place between Li and certain metals or semiconductors used as negative electrodes, as: $M + xLi^+ + xe^- \rightleftharpoons Li_xM$, where M refers to Si, Ge, Sn, Al, and their alloys. These reactions are accompanied by substantial volume changes, which can lead to pulverization and the electrical isolation of the active layer, limiting the lifetime of the device under repeated charge/discharge cycles. Therefore, while these materials represent an attractive class of negative electrodes due to their high theoretical capacity, provided that the large strains that accompany Li alloying can be accommodated, it is crucial to engineer the interfaces between the active layers of the devices to prevent undesirable irreversible reactions.

Extensive work has been realized quantifying the volume expansion/contraction during charging/discharging (lithiation/delithiation) of electrode materials in nanoscale devices [92, 237, 238], as well as determining the morphological changes that occur during charging due to stress/strain accumulation resulting from Li alloying [239–243]. In particular, *in situ* transmission electron microscopy (TEM) experiments have been implemented to probe atomic scale processes in real time that take place during the battery charging and discharging [241, 244, 245]. Further, structural [92] and chemical characterization [245] tools have been combined to demonstrate scenarios where lithiation is irreversible. However, there is still a pressing need to identify how the negative electrode chemical composition changes upon lithiation, because it is closely related to the reversibility of the electrochemical reactions.

Aluminum, low-cost, non-toxic, and earth abundant, is a promising alternative for ultra-lightweight negative electrodes for portable devices, with theoretical capacity equal to 993 mAh/g for lithium storage [246, 247]. Al metal electrodes have recently presented extremely high-rate capability (charging time of 1 minute, with current density of $\sim 4,000$ mA/g), with specific capacity of about 70 mAh/g, resulting from the intercalation/de-intercalation of chloroaluminate anions from the liquid electrolyte into the cathode [248]. Nevertheless, in all-solid-state devices, the alloying reaction between Al and Li leads to the formation of a very stable AlLi alloy ($Al + Li^+ + e^- \rightleftharpoons AlLi$), with consequent pulverization of the negative electrode and rapid loss in capacity in nanoscale devices [246, 249]. However, many details of the degradation mechanism, particularly in thin-film micron-size batteries remain unclear, including the effects of an intrinsic Al_2O_3 layer which covers the

negative electrode surface. This oxide layer is present even when fabricating/testing the battery under high-vacuum conditions (10 Å of Al₂O₃ forms in < 15 min at 10⁻⁴ Torr) [250].

Here we combine X-ray photoelectron spectroscopy (XPS) with local electrical conductivity measurements to characterize the processes that occur on the Al negative electrode outer surface during lithiation in thin-film batteries with the aim of gaining deeper understanding for the rapid loss in capacity. We hypothesize that a few-monolayer thick Al-Li-O compound forms on top of the Al electrode, substantially increasing the electrical resistance at its surface, thus hindering surface-bound charge transport processes and degrading the battery's overall performance. We also demonstrate that coating the Al electrode with a Cu film without breaking vacuum does not resolve the rapid capacity loss. Finally we show that similar SSLIBs fabricated with thin-film Si negative electrodes capped with Cu exhibit remarkably stable performance, retaining > 92% of their discharge capacity after 100 cycles, with an average Coulombic efficiency equal to 98%.

6.2 Effect of Surface Reactions on the Electrochemical Performance

Thin-film SSLIBs were fabricated by sputtering 300 nm of LiCoO₂ as the positive electrode (140 mAh/g), 365 nm of LiPON for the electrolyte (3×10^{-6} S/cm), and 400 nm of Al (993 mAh/g) as the negative electrode and the current collector, as shown in Figure 6.2a. Figures 6.2b-d show scanning electron microscopy

(SEM) images of the morphology of the Al negative electrode surface before (pristine sample) and after cycling the battery under ultra-high vacuum (8.5×10^{-11} Torr). The as-deposited Al surface is smooth, with roughness < 20 nm. The lithiation of the Al layer, accompanied by the volume expansion of the negative electrode, results in the formation of $\sim 1 \mu\text{m}$ diameter mounds distributed on its surface and composed principally of AlLi alloy, as previously determined - see Figure 6.2e for a cross-section SEM image of all the active layers of the device (with a protective Pt capping layer deposited during the FIB process) [240]. AlLi does not form in the bulk of the Al electrode, nor at the LiPON/Al interface; its formation is confined to the outer surface where the large ($\sim 100\%$) volumetric strain can be best accommodated. The surface segregation of AlLi, however, does not in itself explain the rapid loss in capacity, as shown in Figure 6.2f.

Previously, we postulated that formation of the AlLi mounds occurred mainly by surface or grain boundary mediated diffusion, because bulk diffusion coefficients for both Li and Al are very low. Further, we suggested that loss of electrical contact with the negative electrode outer surface segregated AlLi phase did not substantially contribute to the capacity loss, because the mounds remained physically attached to the bulk Al. Because the chemical transformations that accompany charge transfer in SSLIBs with Al negative electrodes occur predominantly on the top surface and because surface diffusion paths for Al and Li are needed for cycling the battery, we have reasoned that loss of surface conductivity could degrade the battery performance. To test this hypothesis, we use conductive atomic force microscopy (c-AFM) to measure the effects of electrochemical cycling on the surface electrical conduc-

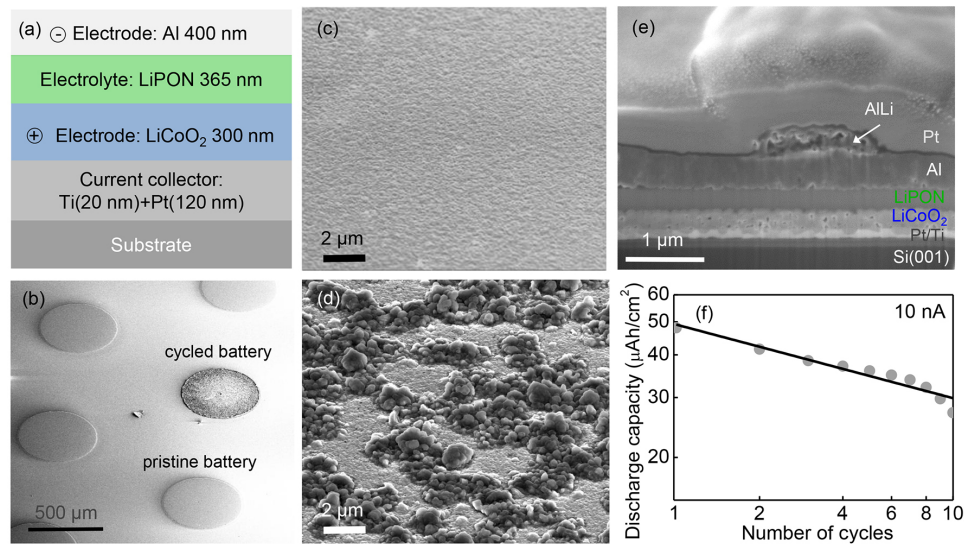


Figure 6.2: (a) Schematic of all-solid-state batteries with Al negative electrodes. (b) SEM of micron-scale devices showing morphology changes upon cycling. SEM of Al surface for (c) pristine and (d) cycled devices shown in (b). (e) Cross-section SEM image of Al electrode after 10 charging cycles, tilt = 45°. The Pt layer is added uniquely to protect the surface of the battery during the ion milling process and is not an active layer of the device. (f) Discharge capacity as a function of the number of cycles for 10 nA.

tivity of the negative electrode, as shown in Figure 6.3. Prior to lithiation the Al layer is highly conductive. Although the Al outer surface is covered with an intrinsic Al₂O₃ layer (Figure 6.3a-b), the oxide is sufficiently thin (~ 3 nm) to allow electron tunneling during the c-AFM measurements. Following 10 charge/discharge cycles at 30 nA, the electrode surface becomes insulating throughout and irrespective of morphology, indicating the formation of a thicker, uniformly distributed insulating layer (Figure 6.3c-d). The possible presence of an insulating layer on top of the Al and AlLi layers can substantially hinder the charging and discharging processes because these must be accompanied by electron flow in and out of the negative

electrode, respectively.

The c-AFM and XPS measurements both suggest that cycling of the SSLIB with Al negative electrodes leads to formation of an insulating surface oxide, which could contribute to capacity loss by preventing electron flow to the surface layers where AlLi alloy is formed. Given that additional oxygen (*i.e.* oxygen not present as native Al₂O₃ prior to cycling) must come from the surrounding environment, we can hypothesize that an electrically conducting film which does not easily oxidize on top of the Al surface would increase the battery cycle life by preventing, or at least slowing the rate of Al-Li-O growth. To test this idea, we evaporated a 400 nm thick Cu capping layer immediately after the Al deposition without exposing the samples to the ambient. As shown in Figure 6.4, the Cu overlayer does not increase the cycle life of the batteries. This result is not entirely surprising given that diffusivity of O in Cu at room temperature is $\sim 10^{-12}$ cm²/s [251], which implies that it would take ~ 1600 s for oxygen to diffuse through the 400 nm thick Cu layer. This new result suggests that capacity fade is likely due to a combination of reasons, which include loss of surface diffusion paths for the Li in the porous AlLi alloy once the surface is oxidized, as well as loss in electrical conductivity. It is interesting to note that from the charge/discharge curves (see Figure 6.5), the charge cycle of the Al/Cu battery does not show a local maximum at 3.8 V compared with that of the uncapped Al-based device, strongly indicating that the existence of the Cu capping layer has altered the electrochemical reactions taking place at the negative electrode and could be another reason for the capacity fade.

Our proposed mechanism implies that if bulk Li diffusion were faster so as

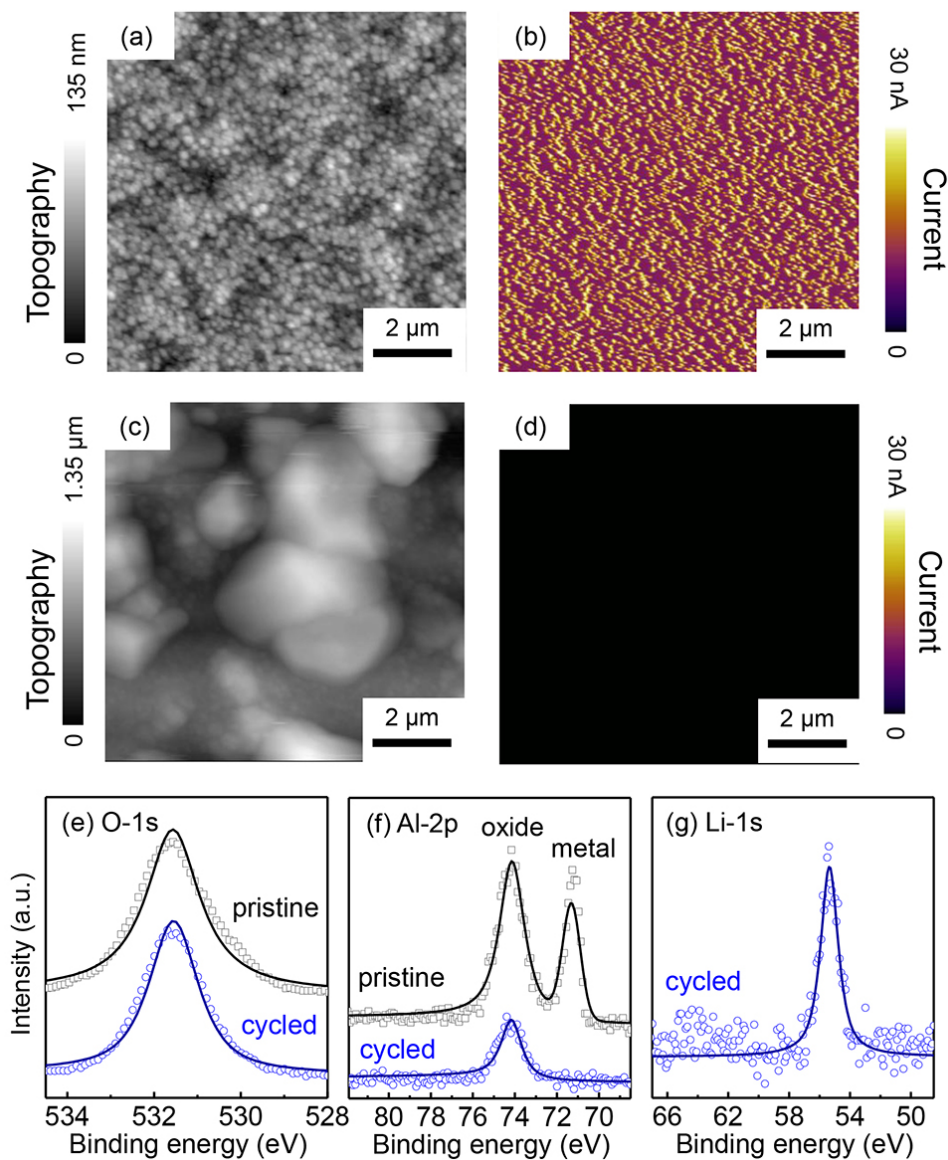


Figure 6.3: Topography and conductive atomic force microscopy scans for (a, b) pristine and (c, d) cycled Al-based batteries, respectively, showing complete loss in electronic conductivity upon cycling. XPS of Al negative electrode for pristine and cycled batteries showing (e) oxygen peaks, (f) Al metal and oxide peaks, and (g) Li peak for the cycled device.

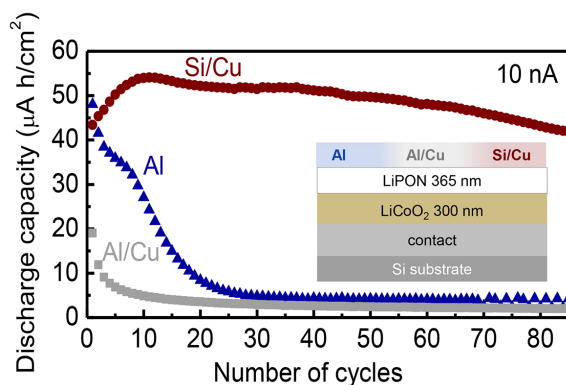


Figure 6.4: Discharge capacity for 400 nm Al, 400 nm Al / 400 nm Cu, and 50 nm Si / 400 nm Cu negative electrodes, for batteries charged at 10 nA in ultra-high vacuum, under identical conditions. Inset: schematic of solid-state devices (out of scale for clarity).

not to depend on surface diffusion, capacity retention could be improved. To test this point, we fabricated similar batteries with 50 nm thick Si negative electrodes [252,253] covered with 400 nm thick Cu. Like Al, Si also rapidly forms an insulating surface oxide; however, Li diffusion is ~ 10 orders of magnitude faster in Si compared to Al [254] and therefore does not depend on surface diffusion mechanism. The SSLIBs with Si electrodes are tested using exactly the same procedure as used with SSLIBs with Al. As shown in Figure 6.6, these batteries retained over 92% of their capacity after 90 cycles.

6.3 Excellent Cycling Performance of Silicon Anode

Figure 6.6 shows the morphology and the electrical analysis of the Si negative electrode after cycling the battery in ultra high vacuum and its electrochemical profile. After cycling the device, the interface between the electrolyte and the Si

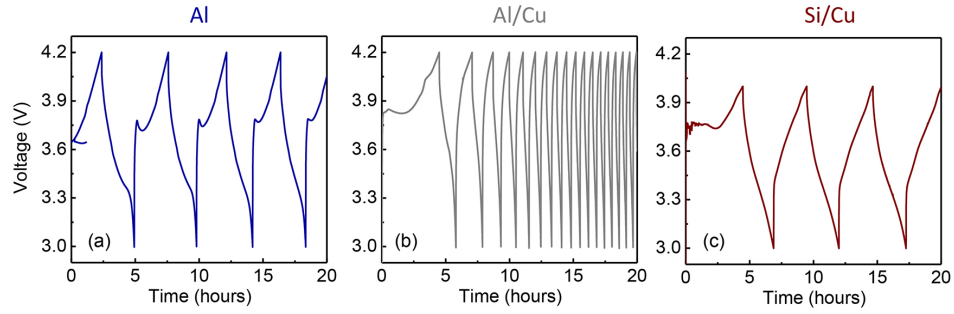


Figure 6.5: Cycling curves for thin-film solid-state batteries with (a) Al, (b) Al/Cu, and (c) Si/Cu negative electrodes, charged at 10 nA.

does not present any accumulation of Li [255], as shown in the cross-section SEM image of Figure 6.6b. *c*-AFM measurements show that the electrical properties of the Si/Cu layer are unaltered upon cycling the battery (see Figure 6.6c-f). The Si/Cu battery shows an excellent performance, with discharge capacity of ~ 15 mAh/cm² after 100 cycles at 30 nA (Figure 6.6g). As a consequence, the Coulombic efficiency of the device is near 100%. This remarkable improvement in performance is due to the fact that Li diffuses almost 10 orders of magnitude faster in Si than it does in Al [254], and thus the formation of the surface mounds and the associated trapped Li does not occur in Si (or at a much lower level). Additionally, an insulating compound analogous to the Al-O-Li, *i.e.* Si-O-Li does not seem to form on the Si electrode surface (see Figure 6.7). The SSLIB with Si has an electrochemical performance similar to micron- and nano-scale size electrodes [117,256], with high cycling stability despite the large volume change that takes place during lithiation. Furthermore, given the same Cu capping layer, the Si-based SSLIB still outperforms the Al/Cu system regarding the capacity retention after long-time cycling. One possible reason

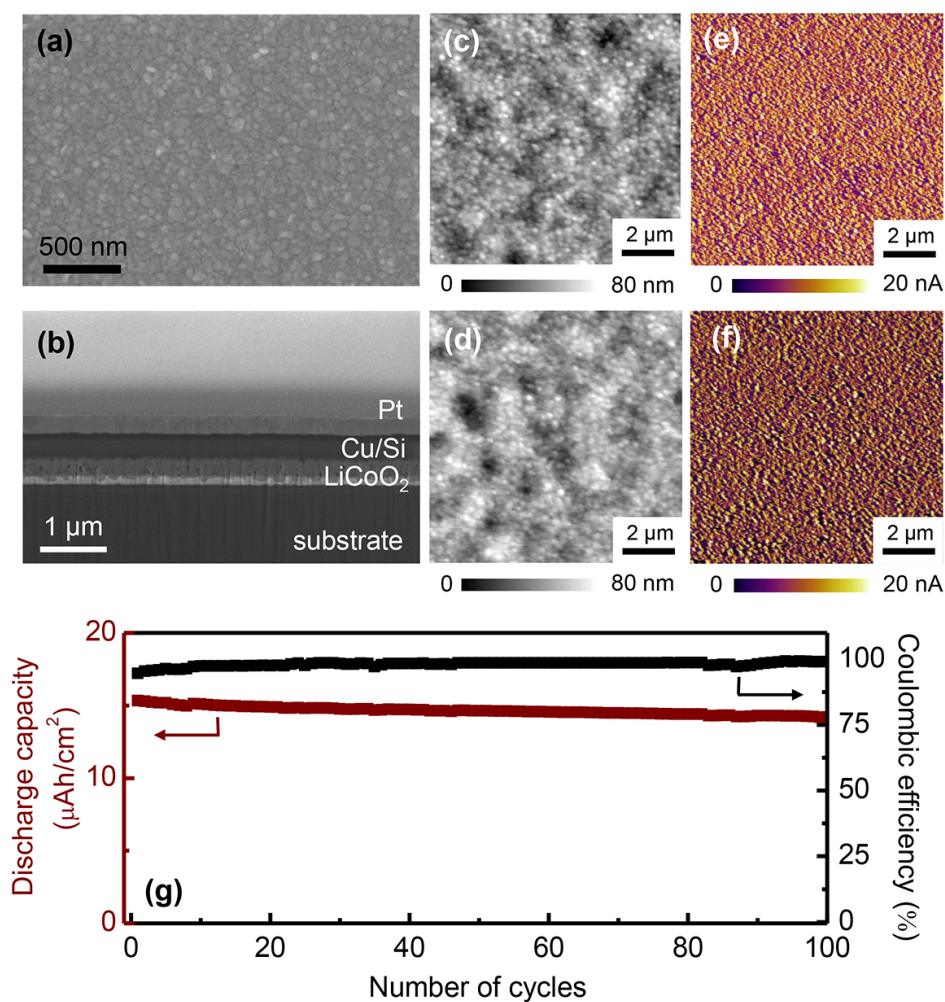


Figure 6.6: (a) Plan-view and (b) cross-section SEM images of Si/Cu negative electrode after 10 charging cycles at 30 nA. A 2 μm thick Pt layer was added to prevent the damage of the Cu/Si top surface during the ion milling process for cross-sectional imaging. Topography and conductive atomic force microscopy scans for (c, e) pristine and (d, f) cycled battery, respectively, showing uniform and constant conductivity upon cycling. (g) Discharge capacity as a function of number of cycles. Capacity retention > 92%, with average Coulombic efficiency = 98%.

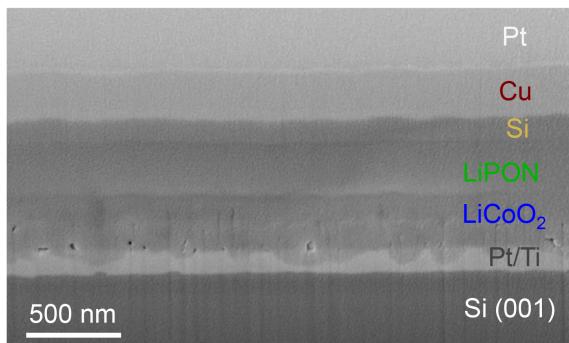
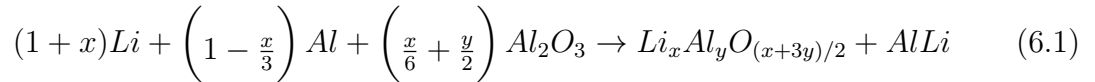


Figure 6.7: Cross-section SEM image of Si-based thin-film all-solid-state battery after 10 cycles at 30 nA, showing smooth interface between the active layers of the device. The Pt layer was added uniquely to protect the surface of the battery during the ion milling process and is not an active layer of the device. SEM settings: 5 kV, 0.10 nA, detector: secondary electron (SE), image tilt = 52 °.

for the limited performance of the Al/Cu battery is that the diffusion of Cu into Al may lead to the loss of lithium diffusion path along the Al grain boundaries that constitute the negative electrode, because Cu does not react with lithium ion at low electrical potential [257]. Moreover, as mentioned before, Li diffusion is much faster in Si than in Al, therefore the potential loss of diffusion path along the grain boundaries in the Si film may not have a significant effect on its electrochemical performance. More detailed studies as to how much each factor contributes to the battery overall performance, such as probing a SSLIB with a thick layer of Al_2O_3 and using a current collector with a substantially different coefficient of thermal expansion as the Al, is planned for the near future.

Our systematic study revealed that the Al/ Al_2O_3 is the limiting interface for the Li reversible diffusion in SSLIB, instead of the electrolyte/electrode interface. Previously, a *P*-Si interdiffused layer has been observed at the LiPON/Si elec-

trolyte/negative electrode interface during nano-battery over-charging [241]. However, for the micron-scale devices like the ones probed here, the effect of this interface is negligible compared to the total volume of the negative electrode. For the thin-film SSLIB containing Al, the surface of the material substantially changes upon cycling, forming a new material (Al-Li-O) that traps Li, according to the following chemical reaction:



This alloy substantially reduces the surface diffusion paths for the Li in the porous AlLi. Further, even after discharging the batteries, the Al-Li-O is still stuck at the surface of the electrode, indicating that this material is thermodynamically stable and that the alloying reaction with Li is not reversible.

6.4 Experimental Methods

6.4.1 All-solid-state Battery Fabrication

The samples were fabricated on a Si (001) substrate with a 100 nm thick SiO₂ layer. 20 nm of Ti and 120 nm of Pt were used as the bottom contact for current collection. 300 nm of crystalline LiCoO₂ (cathode) was deposited by sputtering in the same chamber and without exposure to air. The sample was then annealed in ambient oxygen at 700 °C for 2 hours to smooth the cathode layer. Following the heat treatment, the sample was sputter coated with 365 nm of LiPON (electrolyte) and finally Al, Al/Cu, and Si/Cu negative electrode. Batteries with 0.51 mm in

diameter were fabricated by using a steel mask for the top electrode deposition. All solid-state Li-ion batteries were cycled under ultra-high vacuum, at 8.5×10^{-11} Torr, to prevent any undesired chemical reactions of lithium on the top surface of the negative electrode, and to exclude the possible influence of humidity on the device degradation.

6.4.2 High-resolution XPS Measurements

The XPS data were collected using a 12 kV monochromated Al $K\alpha$ X-ray source (1486.6 eV), and the analyzer was in hybrid lens mode for survey spectra. High-resolution spectra were collected in the same mode using a step size of 0.1 eV and pass energy of 20 eV. For all measurements, the analysis spot size was $220 \mu\text{m}$ in diameter as defined by the instrument electron optics. The charge neutralization system was used and all spectra were calibrated to the C 1s hydrocarbon peak at 284.8 eV.

6.4.3 Conductive AFM Measurements

The c-AFM measurements were carried out at room temperature using a diamond-coated probe with 83 ± 17 nm in diameter and a cantilever with force constant of 2.8 N/m, at ambient environment. During the measurements, the c-AFM probe was in contact with the negative electrode top surface and the current collector located underneath the positive electrode was grounded. The current pathway was then across all the active layers of the thin-film solid-state-battery. Scans were acquired by using a piezo scanner in closed loop, at 0.4 sec/line. The topogra-

phy and current signals were acquired simultaneously, in contact mode, under 10 V bias applied to the probe (see Figure 6.8).

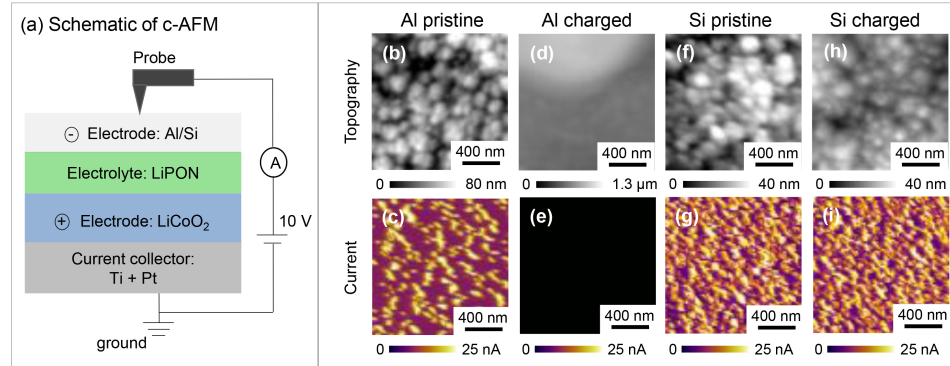


Figure 6.8: (a) Illustration of *c*-AFM measurements performed on thin-film all-solid-state batteries. The measurements were carried out at room temperature using a diamond-coated probe with 83 ± 17 nm in diameter and a cantilever with force constant of 2.8 N/m, at ambient environment. During the measurements, the *c*-AFM probe was in contact with the negative electrode top surface, and the current collector located underneath the positive electrode was grounded. The current pathway was then across all the active layers of the thin-film solid-state-battery. Scans were acquired by using a piezo scanner in closed loop. The topography and current signals were acquired simultaneously, in contact mode, while 10 V was applied to the probe. (b-i) Topography and current maps for thin-film batteries with Al and Si negative electrodes.

6.4.4 Cross-section SEM Imaging of Batteries

2 μm thick film of electron-beam and ion-beam Pt was initially deposited to protect the negative electrode surface during the milling process for cross-sectional imaging. Then, the samples were milled by Ga focused ion beam (FIB), using low current to minimize sample damage (9.3 and 0.8 nA).

6.5 Conclusions

Summarizing, we investigated the degradation of SSLIBs with Al and Si negative electrodes and identified substantial Li accumulation at the top surface of the Al electrode, accompanied by morphological and electrical changes. The Al layer showed fast capacity fade possibly caused by the formation of a ternary Al-Li-O alloy at the top surface of the negative electrode, as confirmed by XPS measurements. This ternary alloy is thermodynamically stable, does not decompose upon battery discharging, and forms an insulating barrier at the top surface of the electrode, as indicated by *c*-AFM measurements. The addition of a Cu protective film did not prevent the capacity loss, due to the presence of an Al₂O₃ thin layer between the negative electrode and the Cu layers, and the sufficiently rapid oxygen diffusion in Cu at room temperature. By comparison, thin-film Si electrodes showed excellent performance up to 100 cycles, retaining > 92% of its discharge capacity, with stable Coulombic efficiency of 98%. The results presented here show the importance of electrode surface and current collector/electrode interface reactions in SSLIB, in addition to those occurring at the electrode/electrolyte interfaces, which are typically the focus of investigation in liquid electrolyte LIBs.

Chapter 7: 3D Tomography of Li ions in All-solid-state Batteries

Summary: Determining where Li preferentially accumulates and how it relates to the formation of solid-electrolyte interphases (SEI) is required for the improvement of power performance and long-term cyclability of all-solid-state energy storage devices. Here, we directly map, in 3-dimensions, the Li distribution in all active layers of batteries by implementing time-of-flight secondary ion mass spectroscopy (ToF-SIMS).

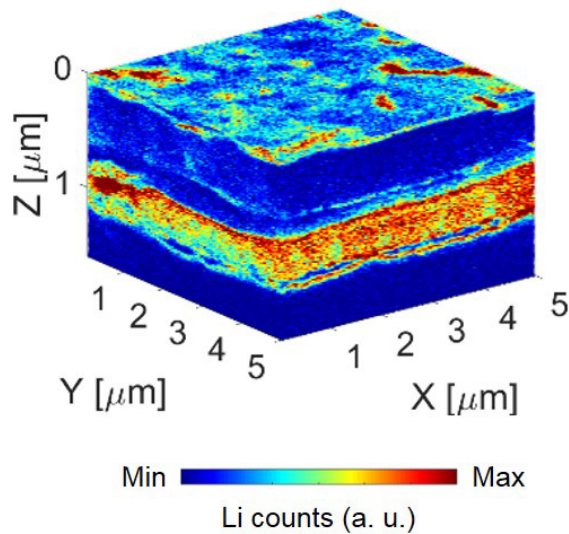


Figure 7.1: 3D tomography of Li ions in all-solid-state batteries.

We deconvolute material diffusion from the chemical changes due to electrochemical processes. We find a remarkable concentration change in Li upon charging, due to the formation of an SEI at the LiPON-LiCoO₂ interface. Resolving Li distribution profile within the battery components is imperative for elucidating the mechanisms of the undesired chemical reactions that currently limits their performance. This chapter is adapted from a manuscript in preparation.

7.1 Introduction

There is currently a pressing need for the development of safe, high-performance battery components for a variety of applications, ranging from portable electronics to electric vehicles [74, 258]. Mobile and small device applications entail volumetric energy density of 1.5 kWh/L for fast charging/discharging [74, 78, 79]. Rechargeable all-solid-state Li-ion batteries (SSLIBs) can potentially meet these demands [240, 259–261]. However, the understanding and control of the mechanisms currently responsible for their limited power and degradation are required for the realization of technologically competitive, long-life energy storage components [262]. For example, reactive interphase (SEI) layer formation between one or both of the electrodes and the solid state electrolyte have been associated with high charge transfer resistance and capacity loss [241, 263]. Methods that can identify such layers by quantitatively measuring the Li distribution can therefore be highly valuable in understanding the operation of the SSLIB and its degradation mechanisms.

Conventional X-ray and electron scattering methods are unsuitable for detecting Li due to its weak scattering efficiency. Surface analysis methods, including X-ray photoelectron spectroscopy (XPS) spectroscopy can be used to determine the chemical composition of Li-ion batteries, but the information obtained is commonly limited to the surface of the material being probed [77]. Band excitation electrochemical strain microscopy, an atomic force microscopy method, has been developed in the past decade to map the spatial variation of Li-ion diffusion paths [264]. Here, the material deformation resulting from the well-known volume expansion that hap-

pens during lithiation has been attributed to Li accumulation within the cathode layer [265–267]. Further, this high spatial resolution measurement (~ 100 nm) revealed the Li diffusion dependence with grain boundaries in promising cathode materials, such as LiCoO_2 [264], LiFePO_4 [265], and $\text{LiNi}_{1/3}\text{Co}_{1/3}\text{Mn}_{1/3}\text{O}_2$ [266]. In situ scanning [240] and transmission [245, 258, 268–270] electron microscopies (S/TEM) have been widely implemented to analyse electrodes in both liquid electrolyte cell and nanoscale all-solid-state devices. These methods, combined with voltammograms, provide a direct correlation between morphological and chemical changes in the battery layers of interest, including the spatial distribution of Li-rich compounds and the formation of SEIs. Electron energy loss spectroscopy (EELS) [241] and glow discharge optical emission spectroscopy [271] have also been proved to enable Li imaging. Depth profiling by neutron scattering has offered valuable insights about the SEI formation in Li half-cells through in-situ non-destructive measurements [272–275].

More recently, time-of-flight secondary ion mass spectroscopy (ToF-SIMS) has been implemented as a diagnosis technique to qualitatively determine the spatial arrangement of Li in liquid cells at different lithiation stages [276]. In ToF-SIMS, a pulsed ion source produces primary ions with a well-defined kinetic energy. These ions are condensed to a focused beam using an electromagnetic lens, which is raster scanned over the sample under investigation, removing and ionizing molecules from the outermost surface. Then, these particles are accelerated into a flight tube and their mass is resolved by determining the time at which they reach the detector (time-of-flight). ToF-SIMS provides elemental and chemical state information of

solid materials, with depth resolution as small as ~ 10 nm [277] and lateral spatial resolution of 100 nm [278], thus, very suitable to investigate the formation of SEIs in Li-ion batteries. To map the elemental distribution within the layers of interest, the devices are usually mounted under a controlled environment and transferred to a SEM/ToF-SIMS in high vacuum for analysis [278]. Despite the very recent use of ToF-SIMS to map the concentration of Li in batteries before and after cycling, this powerful imaging tool has not yet been realized to resolve Li spatial distribution in all the active layers of SSLIBs. Here, we directly resolve the spatial distribution of Li upon lithiation/delithiation processes in SSLIBs with Si and Al anodes, ideal model systems. Using ToF-SIMS we determine, with sub-micron spatial resolution, the concentration of Li within all active layers of the devices at pristine and cycled states of charge, building a 3D tomography of Li ions distribution. The pristine battery with Si anode shows uniform Li distribution within both the cathode (LiCoO_2) and the LiPON electrolyte. We find that, upon the first lithiation, Li is trapped non-uniformly within the Si anode (close to the interface with the electrolyte), causing a Li deficiency in the cathode. After cycling the battery multiple times, we observe that Li does not fully retract from the Si anode upon delithiation, which results from an irreversible lithiation process during cycling. Conversely, the Al anode device experiences substantial volume expansion upon cycling and presents an accumulation of Li ions at the top surface of the anode. Further, it shows a SEI formed at the anode/electrolyte interface for both systems. For polycrystalline and amorphous layers composing solid-state energy storage components, mapping the spatial distribution of ions and the simultaneous formation of SEIs are extremely

valuable to identify undesired chemical reactions that result in capacity fading. The imaging method presented here can be expanded to other solid-state systems, such as Na- and Mg-ion batteries.

7.2 3D Lithium Mapping in All-solid-state Batteries

All battery samples are fabricated on the Si wafer. Briefly, the Pt current collector, LiCoO_2 and LiPON layers are deposited sequentially via sputtering with an annealing process at 700 °C performed after the LiCoO_2 deposition to ensure that the cathode is in the high-temperature phase [262]. The Si anode with the Cu current collector (or the Al anode) are then deposited using electron beam evaporation with a stainless steel shadow mask that defines each SSLIB active area. Then, the devices are cycled to reach different state-of-charge under Ar environment, preventing exposure to moisture and oxygen. Figure 7.2 shows the cross-section SEM image of the Si anode battery, which presents homogeneous morphology and uniform thickness (also see Figure 7.3). The LiPON conformally coats the LiCoO_2 cathode.

To investigate where undesired chemical reaction(s) takes place we spatially resolve the Li distribution within all active layers upon cycling. We perform galvanostatic charging/discharging test and chemical composition analysis by ToF-SIMS. When combined with a focused ion beam (FIB) in a scanning electron microscope, ToF-SIMS provides lateral spatial distribution information, as will be presented later in this chapter. We acquire depth Li concentration information simultaneously by sequentially sputtering the sample using the Ga-ion beam, resulting in

a Li depth profile (red solid line in Figure 7.2). The increase in Li concentration at the LiPON/LiCoO₂ interface likely results from interdiffusion between the two materials.

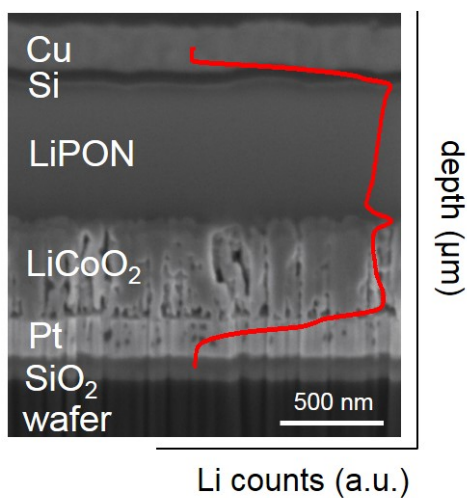


Figure 7.2: Cross-section SEM image of a pristine battery with Si anode overlaid with the Li depth profile obtained from ToF-SIMS. Cu and Pt are used as the anode and cathode current collectors, respectively.

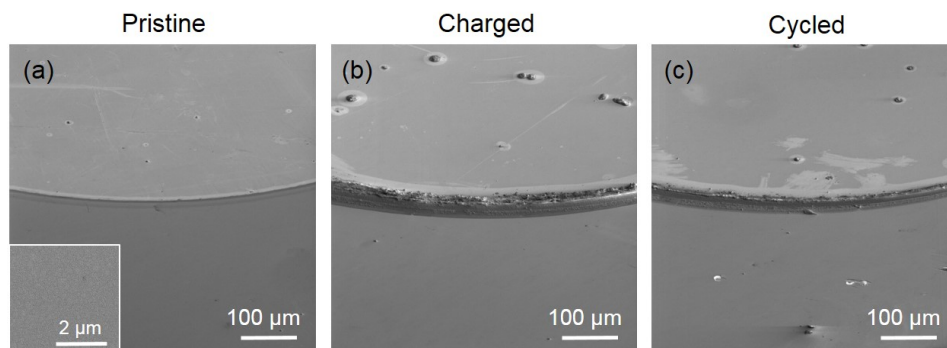


Figure 7.3: SEM images of (a) pristine, (b) charged, and (c) cycled batteries with Si anode (tilt at 55°). Inset: plan-view SEM image for the pristine battery.

Figure 7.4a shows the voltage profile of the cycled Si anode battery, where the colored squares highlight the three different states of charge investigated in this work. The initial capacity loss is due to the irreversible lithiation process [262] of the SSLIBs (see Figures 7.2a). The charged battery is at 4.1 V and another device cycled for four times is left at 3.0 V (at a discharged, cycled state). Figure 7.4b presents the Li depth profiles of these three batteries (fabricated simultaneously for comparison), acquired over a 5 by 5 μm^2 region (see Figure 7.5 for SEM images of the samples after the ToF-SIMS measurements). The Li concentration profile of the pristine battery (red curve) differs from both the charged and cycled devices (blue and black, respectively). First, in the initial ~ 200 s of sputtering time we measure the Cu and Si layers. The presence of Li within the pristine battery only appears very close to the electrolyte layer and is caused by its diffusion during the layers deposition. Second, the higher concentration of Li at shorter sputtering time for the charged device indicates that Li moved to the Si anode during lithiation (compare red and blue curves). The maximum Li concentration at ~ 250 s refers to the Si/LiPON interface, as the Si counts decrease significantly around the same time (see Figure 7.6 and we determine the interface accordingly). Third, the variation in Li concentration that takes place between 600 s and 750 s is likely related to the formation of an SEI, as reported in similar battery systems [241]. The charged battery (blue curve) shows the highest Li concentration at the LiPON/LiCoO₂ interface (in Figure 7.6 the Co signal increases between 600 s and 750 s at the LiPON/LiCoO₂ interface). The cycled sample (in black) presents a similar depth profile, with a modest reduction in the Li content, strongly suggesting that even after delithiation Li preferentially

accumulates at this newly formed SEI. Similar depth profiles are measured among other representative regions for the Si anode SSLIBs (see Figure 7.6). The Li distribution in each layer/interface and where Li is accumulated upon cycling within the SSLIBs are discussed in detail below.

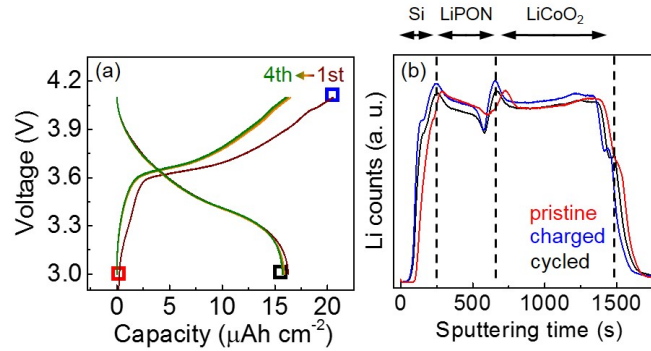


Figure 7.4: (a) Voltage profile for a Si anode all-solid-state battery cycled at 50 nA. (b) Li depth profiles acquired from ToF-SIMS for three batteries at different state-of-charge: pristine (red), charged (blue) and cycled (black).

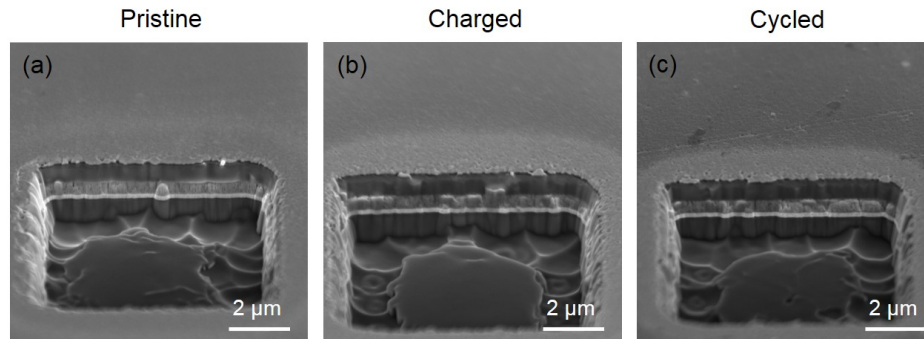


Figure 7.5: SEM images after ToF-SIMS measurements on (a-c) a 7 by 7 μm^2 region for three batteries with Si anode at different state-of-charge: pristine, charged, and cycled. Tilt: 55° . An area of 5 by 5 μm^2 in (a-c) was analyzed for the depth profiles and Li distributions to avoid the edge effect in ToF-SIMS.

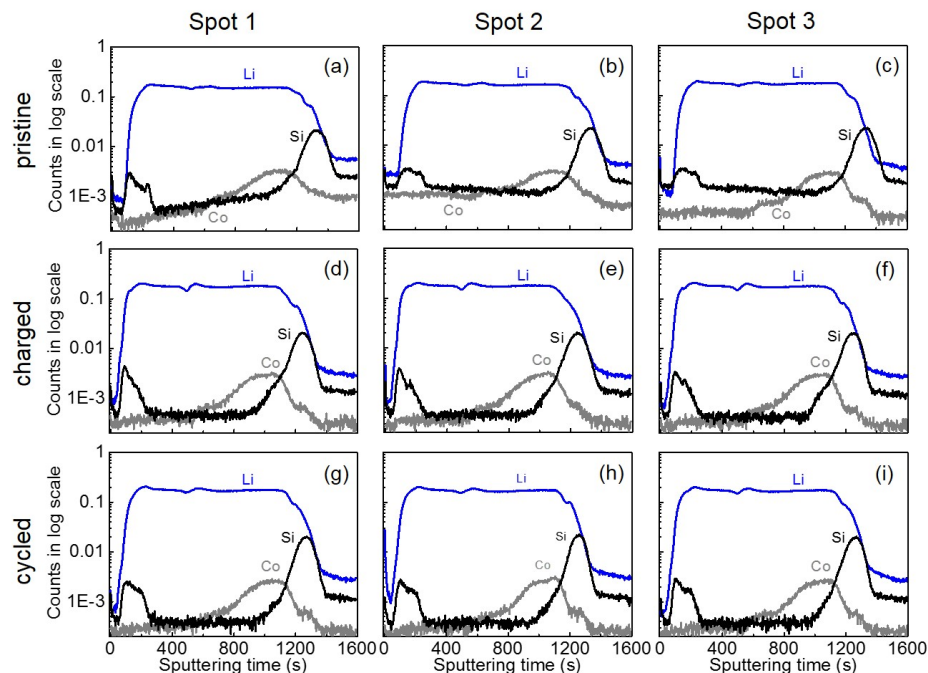


Figure 7.6: Depth profiles for Li (blue), Si (black), and Co (grey) acquired in $5 \text{ by } 5 \mu\text{m}^2$ representative regions (spots 1-3) for (a-c) pristine, (d-f) charged, and (g-i) cycled batteries with Si anode. The count is plotted in log scale for clarity.

To acquire a full picture of Li spatial distribution in each active layer within the SSLIBs and correlate it with lithiation/delithiation processes, we determine its spatial concentration in 3D, with sub-micron spatial resolution. We measure all active layers of the three devices by ToF-SIMS under high vacuum to prevent material contamination. Figure 7.7 shows 3D maps of Li spatial distribution for all samples. The Si surface remains unchanged upon cycling the battery, with no obvious Li accumulation see Figure 7.7a-c. Figure 7.7d-f refers to the Si/LiPON interface where we measure Li trapped upon first charging (Figure 7.7e). Note that Li does not fully retract during delithiation (Figure 7.7f). Thus, both charged and cycled Li maps

present similar concentration. This result is consistent with the capacity loss after the battery's first charging, as shown in Figure 7.8. Figure 7.7g-i corresponds to the LiPON electrolyte, and shows similar Li concentration for all states of charge. The spatial distribution of Li at the LiPON/LiCoO₂ interface is presented in Figure 7.7j-l. Here, the increase in Li concentration upon cycling is likely due to the formation of an SEI. The maps for the LiCoO₂ cathode and the LiCoO₂/Pt interface are displayed in Figures 7.7m-o, and 7.7p-r, respectively. Note the Li depletion within the cathode even when the device is fully discharged, see Figure 7.7r. Moreover, the Li ions cannot fully extract/insert in the Si anode after cycling, as confirmed for multiple representative regions mapped by ToF-SIMS measurements (see Figures 7.9, 7.10, and 7.11 for additional Li concentration maps).

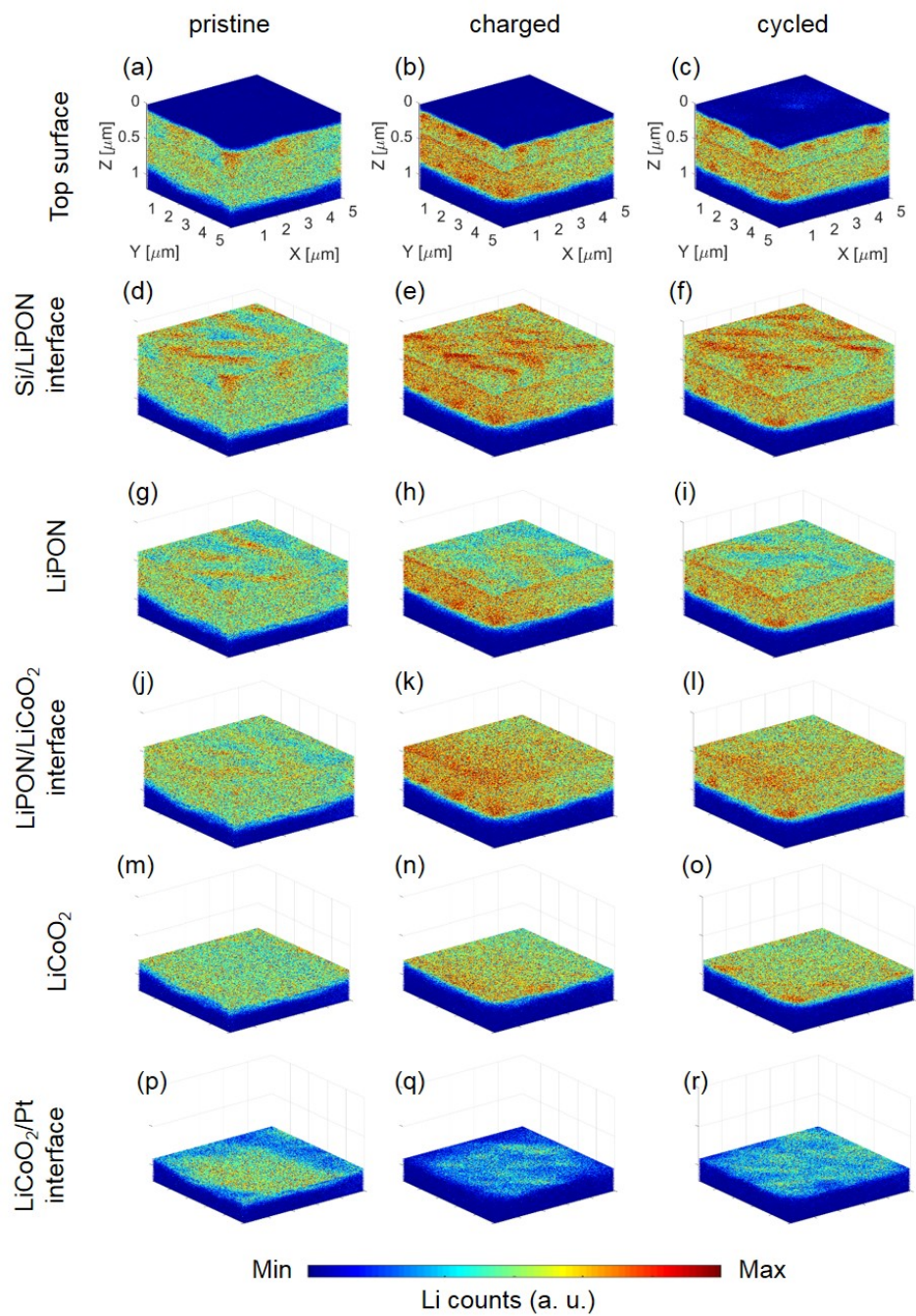


Figure 7.7: Li ions distribution maps for representative regions of pristine, charged, and cycled batteries. (a-c) Top surface, (d-f) Si/LiPON interface, (g-i) within LiPON layer, (j-l) LiPON/LiCoO₂ interface, (m-o) within LiCoO₂ layer, and (p-r) LiCoO₂/Pt interface.

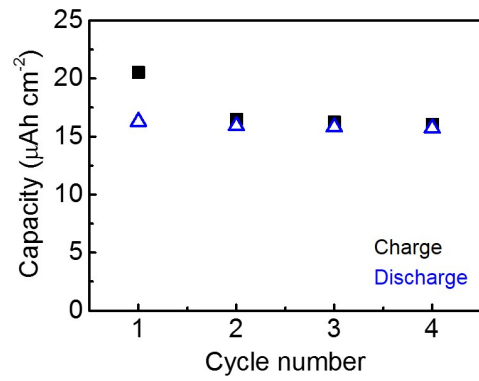


Figure 7.8: Charge/discharge capacity of the cycled Si anode battery (cycling at 50 nA).

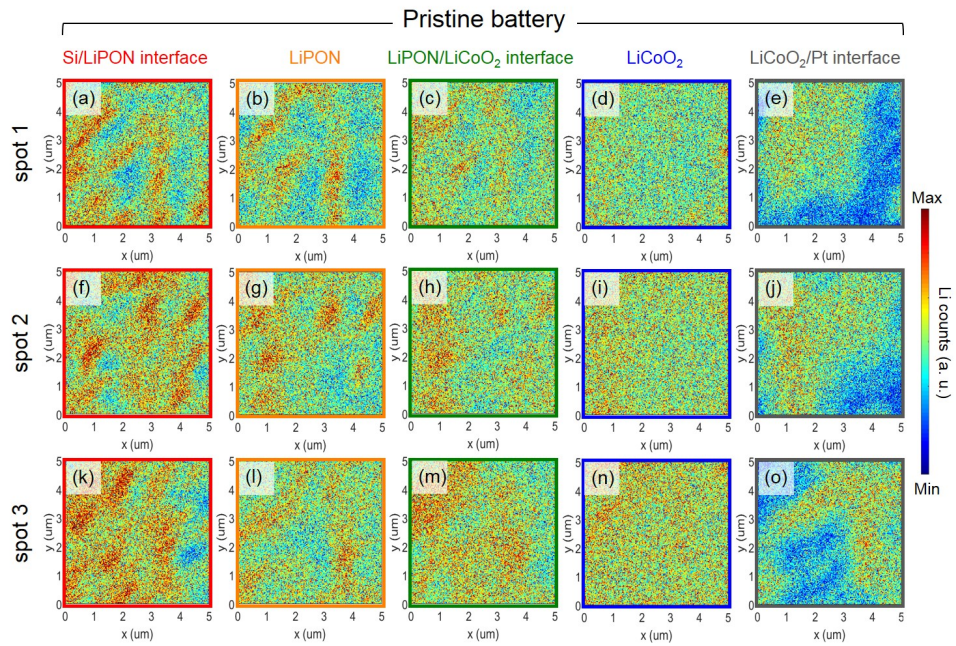


Figure 7.9: Li distribution maps for the pristine battery with Si anode of (a-e) spot 1, (f-j) spot 2, and (k-o) spot 3

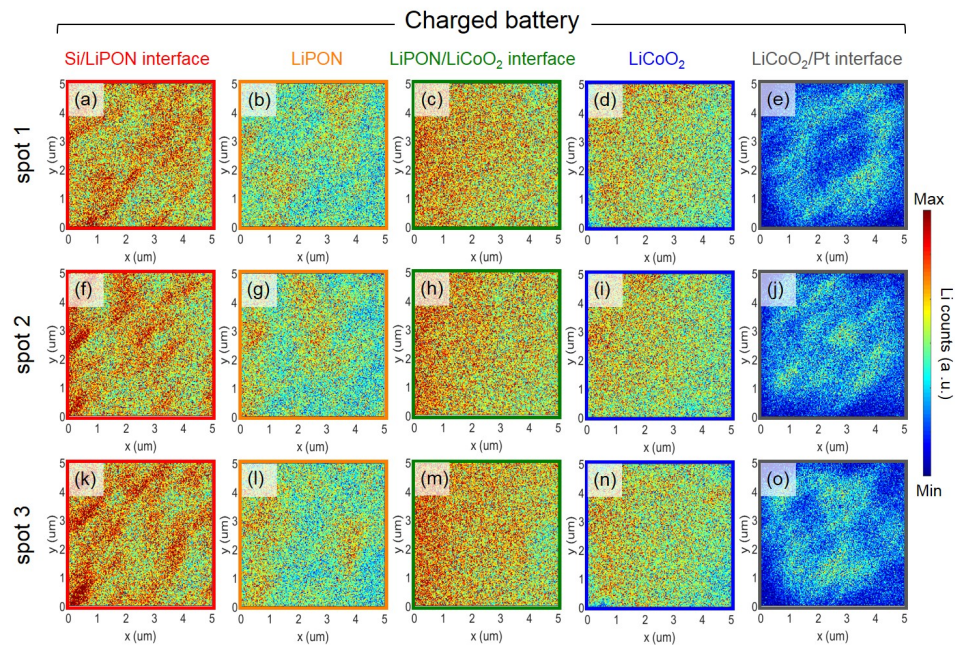


Figure 7.10: Li distribution maps for the charged battery with Si anode of (a-e) spot 1, (f-j) spot 2, and (k-o) spot 3

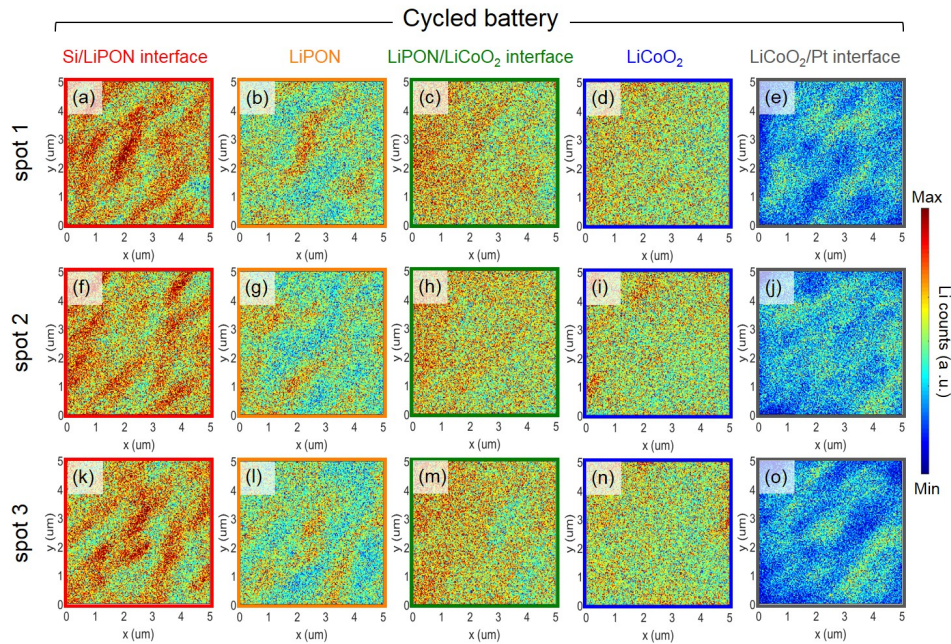


Figure 7.11: Li distribution maps for the cycled battery with Si anode of (a-e) spot 1, (f-j) spot 2, and (k-o) spot 3

7.3 Universality of the Imaging Method

Our 3D imaging method for Li ions can be adapted to other solid-state energy storage device, such as Al anode SSLIBs with the potential ultra-lightweight applications. Figure 7.12a, b shows that Li ions accumulate on the top surface of Al anode after we cycle the battery and its volume expansion results in the different height of the SSLIBs. We also identify a negligible amount of Li within the Al anode before and after cycling, see Figure 7.12c-d. This result agrees with our previous report [77, 240] that after cycling the SSLIB a Li-Al-O layer is irreversibly formed on the top surface. The formation of the Li-Al-O capping layer is thermodynamically stable and it decreases the amount of Li ions for reversible lithi-

ation/delithiation, partially leading to capacity fade (see Figure 7.13). As presented in Figure 7.12e, f, the Li concentration significantly increases at the Al/LiPON interface after cycling. We hypothesize that the SEI formation is responsible for trapping Li at the anode/electrolyte interface. Similarly, we detect a Li depletion within the LiCoO₂ after cycling (see Figure 7.12g, h and Figure 7.14). There is no evidence of Li accumulation at the LiPON/LiCoO₂ interface, differing from the Si anode SSLIB. Further investigation to identify the preferential pathway for lithiation and the reactions at the electrodes/electrolyte interfaces during cycling through in-situ ToF-SIMS measurements are planned for the near future.

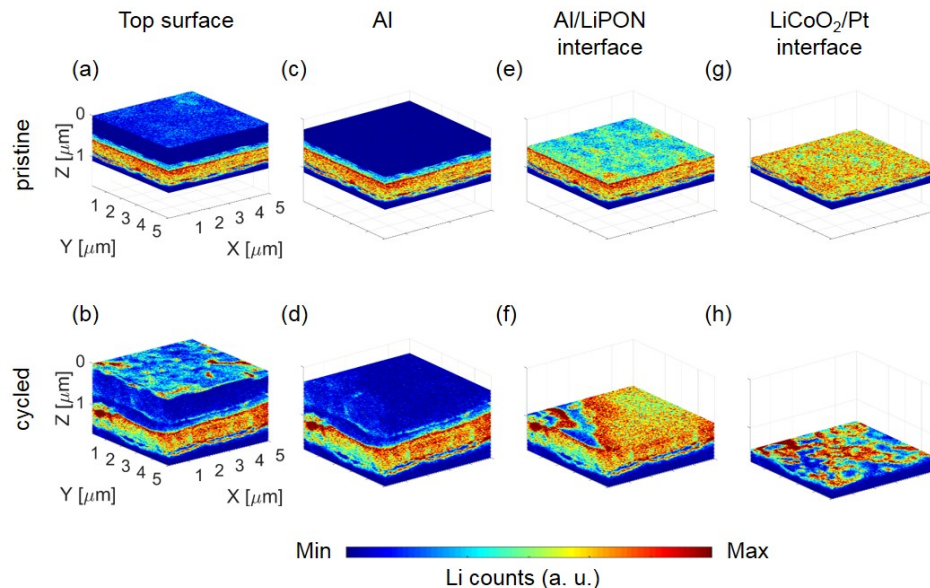


Figure 7.12: 3D Li ions distribution maps for representative regions of pristine and cycled Al anode solid-state batteries. (a, b) Top surface, (c, d) within Al anode, (e, f) Al/LiPON interface, and (g, h) LiCoO₂/Pt interface.

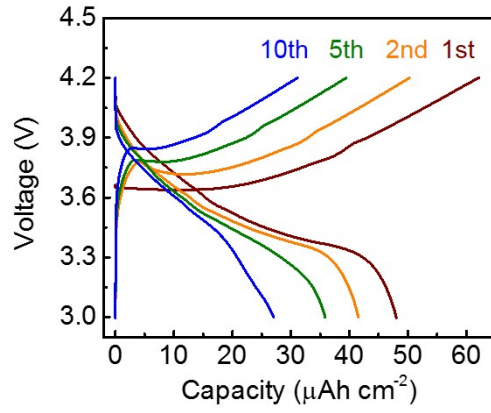


Figure 7.13: Voltage profile of an Al anode all-solid-state battery cycled at 10 nA.

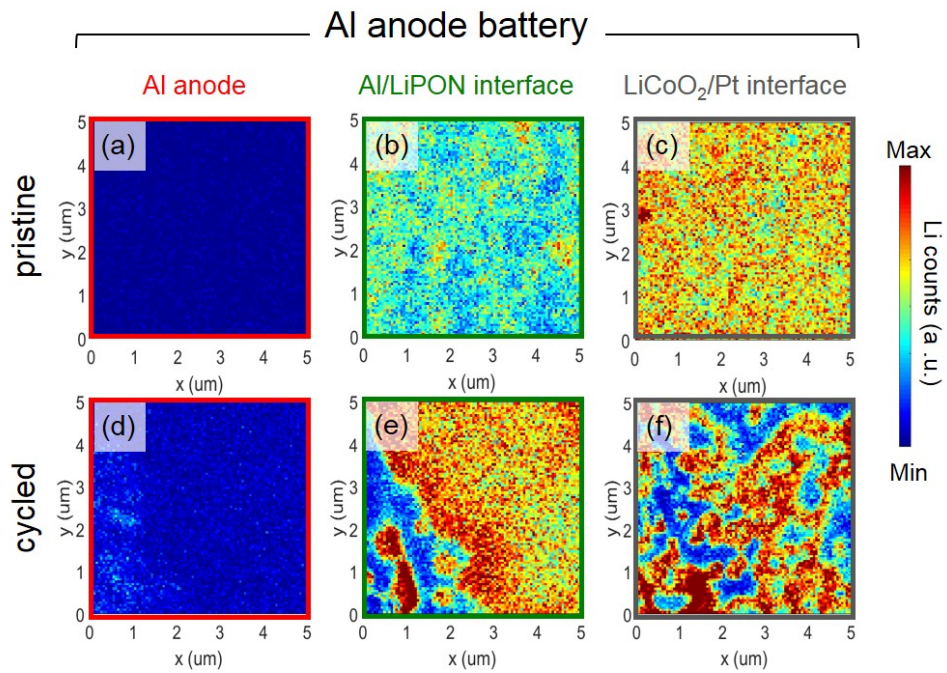


Figure 7.14: Li distribution maps for the cycled battery with Al anode.

In this work we achieve critical information about the electrochemistry of

SSLIBs through direct imaging of Li within all active layers of model system devices. Resolving Li distribution provides insights as to where the undesired chemical reactions take place (irreversible lithiation/delithiation) while cycling the SSLIBs. For batteries with Si anode, the Li trapped in the anode contributes to the irreversible modest capacity loss upon first cycling and the non-uniform Li distribution within LiPON electrolyte strongly suggests that a structural dependent inter-grain diffusion [264, 278] is favored in the system under investigation. Nevertheless, Li ions accumulate and trap at the top surface of Al anode and form a Li-Al-O layer after cycling. This leads to drastic capacity fading, indicating the importance of controlling and engineering the electrochemical reactions at the surface to boost the battery performance. Our results combining galvanostatic charging/discharging and ToF-SIMS imaging support the hypothesis that preferential lithiation paths originate from the structural and chemical properties of the material [240, 278]. We expect ToF-SIMS to become a routine characterization tool to probe Li spatial distribution in a variety of energy storage systems due to: (i) imaging where Li ions accumulate (often results in volume expansion and strain) will help to engineer the microstructure of battery materials to avoid potential cracks and failure of the device, and (ii) building 3D tomography of Li distribution at the electrode/electrolyte interfaces will facilitate the study of electrochemical stability of solid electrolytes by showing how the new interphase alters the Li distribution and migration after cycling. Overall, resolving the driving forces for the irreversible chemical reactions often observed in rechargeable SSLIBs and where Li accumulates will, no doubts, help the solid-state battery community to design and engineer the next-generation

of energy storage devices, with enhanced electrochemical performance and longer lifetime.

7.4 Experimental Methods

7.4.1 Battery Fabrication

Pt is initially sputtered as the cathode current collector on a Si substrate with a SiO₂ layer (100 nm thick). 300 nm thick LiCoO₂ (cathode) was sputtered on top of Pt without air exposure. An annealing process (700 °C for 2 hours in ambient oxygen) was applied to reach high-temperature LiCoO₂ phase, followed by sputtering 500 nm of LiPON (electrolyte) on top of LiCoO₂. Subsequently, 100 nm of Si (anode) with 300 nm of Cu (current collector) or Al were deposited using electron beam evaporation through a steel mask with arrays of 1.65 mm in diameter. The thin-film all-solid-state batteries were cycled under Ar environment in a glove box to prevent any side reactions or possible contaminations from air exposure. Galvanostatic charging/discharging were carried with voltage window from 3.0 to 4.1 V.

7.4.2 ToF-SIMS Imaging

ToF-SIMS maps are acquired using a SEM/FIB dual beam system. Two different cells were charged/cycled at 50 nA for Si anode device and one cell with Al anode were cycled at 10 nA to reach various states of charge. The all-solid-state batteries were then mounted on a sample holder and transferred to the FIB

chamber. The ToF-SIMS measurements were performed using a 20 keV Ga⁺ ion beam scanning across the sample with current at ~ 130 pA. The generated positive secondary ions were analyzed by a ToF-SIMS detector in situ, in the FIB system. Areas of $5 \times 5 \mu\text{m}^2$ were analyzed. During the measurement, the vacuum was kept below 2.7×10^{-2} Pa (2×10^{-4} Torr) at all times.

7.5 Conclusions

In conclusion, we implemented ToF-SIMS to determine the Li spatial distribution within each active layer of SSLIBs with Si and Al anodes at different states of charge. We deconvoluted the depth variations in Li concentration that are due to diffusion and the formation of an SEI upon lithiation. The pristine battery with Si anode showed the presence of Li near the Si/LiPON interface, caused by material diffusion during the films deposition by sputtering. Concurrently, a uniform distribution of Li was found within the cathode. We identified that Li is retained in the Si anode and cannot be fully extracted/inserted upon cycling, resulting in a remarkable spatial variation of the Li concentration within the anode, irrespective of the original distribution of this element, for both charged and cycled batteries. We further extended the 3D tomography of Li distribution to Al anode devices and demonstrated the universality of our imaging method. The direct imaging of Li distribution in all active layers of SSLIBs upon lithiation/delithiation represents a significant step towards resolving the chemical reactions that take place within these devices. The use of ToF-SIMS to directly map Li can be applied to other 3D

configurations, including wire-shaped and scaffold geometries, and to other material systems, such as Na and Mg-ion devices. We foresee the precise determination of where the ions preferentially accumulate upon cycling to elucidate the chemical reactions responsible for the capacity fade that currently limits a variety of rechargeable batteries.

Chapter 8: Conclusions and Outlook

In conclusion, we provided, in the first part of this thesis, a novel class of metallic materials with tunable optical properties by forming binary mixtures of Ag, Au, and Cu. We studied how the chemical composition changes its optical response in both thin films and nanostructures. Further, by implementing a binary mixture of Cu and Al, we demonstrate an Al-Cu/Si stacks with maximum absorption $> 99\%$. In the second part of this thesis, we delivered a comprehensive study of Li-ion distribution in Al and Si anode all-solid-state battery. By resolving where the ions preferentially accumulate and the irreversible reactions take place, our results will help elucidate the degradation mechanism of solid-state energy storage devices.

We fabricated binary noble metal mixture thin films of Ag, Au, and Cu by co-sputtering, which yields an ideal model system to investigate how the chemical composition affects the dielectric functions. By experimentally determining the dielectric functions of each alloyed thin film, we showed the tuning of the optical properties of noble metal mixtures by modifying their chemical composition. Further, we use Ag-Au alloyed nanoparticles as an example to illustrate how alloying can tune the LSPR of metallic nanostructures. We found a localized field enhancement around and within the alloyed nanoparticles, agreeing very well with our calcula-

tions. This part of the thesis builds a platform of metal alloys with tunable optical properties, which make it possible to control the alloy composition to attain optical properties that will meet desired resonances for the applications ranging from nanophotonics to bio-sensing.

We provided the SPP dispersion relations of Ag-Au alloyed thin films and reveal the physical origin of the optical behavior by VBS with DFT calculations of band structures. We found that the dispersion relations can be engineered upon changing the chemical composition of the alloy. The VBS showed a correlation between the binding energy onset of the d band and the corresponding energy of the transmission resonance peak. To further explain how the energy position of the d band determines the threshold of the interband transition (resonance), we investigated the energy position of the d band by calculating the band structure for each alloy by DFT. We confirmed that d band moves to closer to the Fermi level as Au content increases, leading to the change of the interband transition which agrees very well with the optical properties.

By using metallic materials, we obtained a photonic device, namely superabsorbers, with maximum absorption $> 99\%$. The superior performance of Al-Cu/Si thin film absorbers was first demonstrated by calculations and then validated with experiment. We show that the maximum absorption peak (remains $> 99\%$) could be tuned through changing the thickness of Si layer. The multi-wavelength near-unity absorption persists for oblique angle of incidence, up to 70 degrees. Our superabsorber made of Al-Cu/Si stacks was fabricated by co-sputtering, which is lithography-free and capable of scalable and wafer-scale productions.

For energy storage, we used a multi-approach method to study the degradation mechanism of Al anode all-solid-state battery. We disclosed the formation of a Li-Al-O complex on the Al anode surface upon cycling based on c-AFM, XPS, and galvanostatic charging/discharging. The Li-Al-O layer was insulating and prevented the electrons flowing and out of the electrode, leading to the capacity fading. Nevertheless, Si anode presented a stable cycling performance, maintaining > 92% of its initial capacity after 100 cycles. Further, we directly mapped the Li distribution within all layers of all-solid-state batteries. We built a 3D tomography of Li-ion distribution in solid-state batteries and deconvoluted the concentration change of Li that are due to the ion diffusion and the formation of the SEI after cycling. We revealed that Li ions accumulate at the anode/electrolyte interface and cannot fully retract upon cycling, resulting in the irreversible capacity fading. We extended the 3D Li-ion tomography to batteries with different anodes and demonstrated the universality of our imaging tools. We foresee that our imaging method can be used to provide critical insight into the electrochemistry in other systems, such as Na- and Mg-ion batteries.

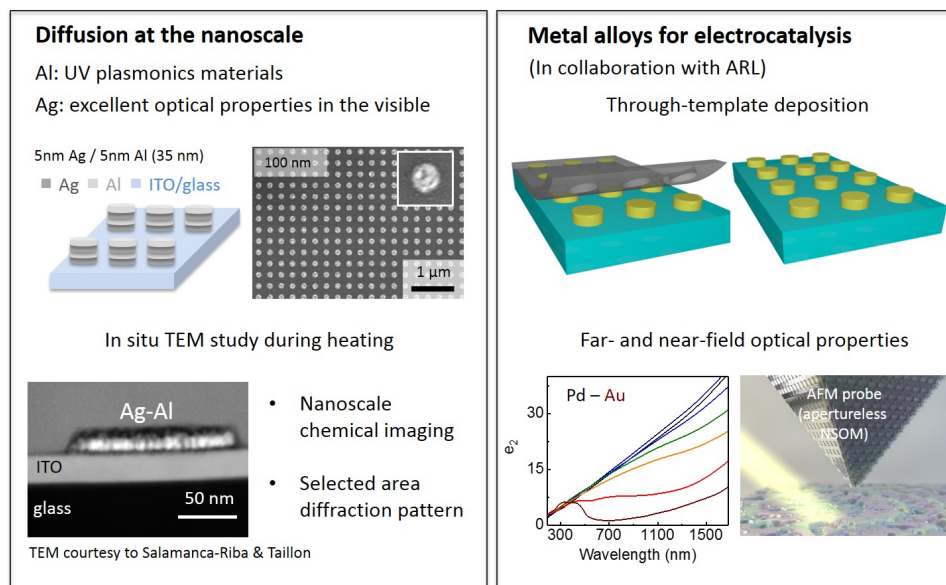


Figure 8.1: Building the library of optical properties for metallic alloy.

The future work is to (i) enrich the library of the metallic alloys to other binary, ternary alloys and study their optical behavior, as shown in Figure 8.1, and (ii) imaging where Li ions are during cycling and building the Li tomography at the solid electrode/electrolyte interface. For the first task, we will use co-sputtering to fabricate alloy thin films, such as Au-Cu, Al-Mg, and Ag-Au-Al for plasmonic materials that operate in the visible and/or UV range of the spectrum. We will study the dielectric function of each alloy. Besides correlating the chemical composition to the dielectric functions, structural information based on X-ray diffraction of the binary and ternary alloys will be added to the library. The long-term goal is to build a relation of the structural, chemical, and optical properties of the novel metallic materials. For the second task, the future work lies in the development of advanced AFM systems to allow *in-situ* characterizations of chemical, electrical,

and electrochemical behaviors of battery materials (adapted from Ref [98]). For this, innovative environmental cell stages and cycling accessories will be integrated into an AFM to scan the sample while cycling. The advantages of *in situ* analysis are both eliminating sample transfer and preventing contamination due to air and/or moisture exposure. It is especially necessary to access the SEI formation and possible degradation, both locally and during cycling, because such information is time-sensitive and often hard to validate in *ex-situ* methods. We also anticipate the combination of chemical and ion diffusion imaging, *e.g.* Tip-Enhanced Raman Spectrum, on the same region, as the relationship between the chemical composition and electrochemistry for multi-component electrodes is still under pursuit. Ultimately, this correlative microscopy approach will describe the intricate relationship between the structural, chemical, and electrochemical properties of materials used in energy storage devices.

Appendix A: Products of This Research

A.1 Awards/Honors

14. The Ann G. Wylie Dissertation Fellowship (2017)
13. The Harry K. Wells Graduate Fellowship (2017)
12. UMD Graduate Student Summer Research Fellowship (2017)
11. Outstanding Reviewer for *Electrochimica Acta*, Elsevier (2017)
10. Outstanding Reviewer for *Optics and Laser Technology*, Elsevier (2017)
9. OSA/SPIE Student Poster Competition, 2nd place (2017)
8. Outstanding Reviewer for *Energy Conversion Management*, Elsevier (2016)
7. Outstanding Reviewer for *Chemical Engineering Journal*, Elsevier (2016)
6. UMD Graduate Student Summer Research Fellowship (2015)
5. The Jacob K. Goldhaber travel grant (2014)
4. UMD Graduate Assistantship (2013-2014)
3. National Fellowship for Honored Student, China (2011-2012)
2. Fellowship for Honored Student, Shandong University (2010) & (2011)
1. Undergraduate Research Scholar Grant at Shandong University (2010-2012)

A.2 Publications/Presentations

A.2.1 Publications Related to This Thesis



Figure A.1: Journal covers highlighting publications from this thesis.

8. **C. Gong**, J. Huddy, F. E. Gabaly, E J. Fuller, A. A. Talin, M. S. Leite, “3D Tomography of Li ion distribution in all-solid-state batteries,” In preparation
7. **C. Gong**, A. Kaplan, A. Kaplan, Z. A. Benson, D. R. Baker, J. P. McClure, A. A. Rocha, M. S. Leite, “Band structure engineering by alloying for photonics,” Under review
6. Z. A. Benson, **C. Gong**, M. S. Leite, “Optical response of nanostructures: from pure to alloyed metals,” **Book Chapter**, In press
5. M. R. Dias*, **C. Gong***, Z. A. Benson, M. S. Leite, “Lithography-free, omnidirectional, CMOS-compatible AlCu alloys for thin film superabsorbers,” Adv. Optical Mater. 6, 1700830 (2018) (***equal contribution**) **Front cover**
4. E. M. Tennyson, **C. Gong**, M. S. Leite, “Imaging energy harvesting and storage system at the nanoscale,” ACS Energy Lett. 2, 2761 (2017) **Front cover**
3. **C. Gong***, M. R. Dias*, G. Wessler, J. A. Taillon, L. G. Salamanca-Riba, M. S. Leite, “Near-field optical properties of fully alloyed noble metal nanoparticles,” Adv. Optical Mater. 5, 1600568 (2017) (***equal contribution**) **Front cover**
2. **C. Gong**, M. S. Leite. “Nobel metal alloys for plasmonics,” ACS Photonics, 3, 507 (2016). **Front cover**
1. **C. Gong**, D. Ruzmetov, A. Pearse, D. Ma, J. N. Munday, G. Rubloff, A. A. Talin, M. S. Leite. “Surface/Interface effects on high-performance thin-film all-solid-state Li-ion batteries,” ACS Applied Materials & Interfaces, 7, 26007 (2015). **Front cover**

A.2.2 Additional Publications during Ph.D.

2. D. Ha, **C. Gong**, M. S. Leite, J. N. Munday, “Demonstration of resonance coupling in scalable dielectric micro-resonator coatings for photovoltaics,” ACS Appl. Mater. Interfaces 8, 24536 (2016) **Front cover**

1. E. M. Tennyson, B. Roose, J. L. Garrett, **C. Gong**, J. N. Munday, A. Abate, M. S. Leite, “Fully reversible local electrical response of Caesium-incorporated triple cation perovskites.” In preparation

A.2.3 Oral Presentations

(Presenter marked by *)

27. M. R. Dias*, C. Gong, Z. A. Benson, M. S. Leite, “AlCu alloyed thin films for perfect absorbers in a planar bilayer configuration,” American Physical Society March Meeting, Los Angeles, CA (2018)

26. C. Gong*, Z. A. Benson, A. Kaplan, M. R. Dias, M. S. Leite, “Metal alloy thin films and nanostructures for plasmonics,” Materials Research Society Fall Meeting, Boston, MA (2017)

25. C. Gong*, E. J. Fuller, F. E. Gabaly, Z. Jadidi, A. A. Talin, M. S. Leite, “Investigation of the degradation mechanism for solid-state Li-ion batteries by chemical composition mapping,” Materials Research Society Fall Meeting, Boston, MA (2017)

24. C. Gong*, Z. Jadidi, F. E. Gabaly, E. J. Fuller, A. A. Talin, M. S. Leite, “Resolving lithium ions in all active layers of lithium ion all-solid-state batteries,”

232nd Electrochemical Society Meeting, National Harbor, MD, (2017)

23. C. Gong*, Z. Jadidi, F. E. Gabaly, E. J. Fuller, A. A. Talin, M. S. Leite, “Resolving the mechanism of capacity fading in Li-ion solid-state batteries,” American Chemistry Society Fall Meeting, Washington, DC (2017)

22. A. Kaplan*, C. Gong, M. R. Dias, M. S. Leite, “Dispersion measurements and calculations of AlCu thin films,” American Chemistry Society Fall Meeting, Washington, DC (2017)

21. Z. Benson*, M. R. Dias, C. Gong, M. S. Leite, “Exploring optical properties of self-assembled supracolloidal nanostructures with varying compositions and geometries,” American Chemistry Society Fall Meeting, Washington, DC (2017)

20. D. Ha*, C. Gong, M. S. Leite, J. N. Munday, “Dielectric resonator-based antireflection coatings,” Materials Research Society Spring Meeting, Phoenix, AZ (2017)

19. C. Gong, M. S. Leite*, “In situ investigation of capacity fade in all-solid-state batteries,” Materials Research Society Fall Meeting, Boston, MA (2016)

18. C. Gong, M. R. Dias, M. S. Leite*, “Metal alloys for plasmonic applications,” Materials Research Society Fall Meeting, Boston, MA (2016)

17. M. R. Dias, C. Gong, G. Wessler, M. S. Leite*, “Alloyed metallic nanoparticles for photovoltaics,” Materials Research Society Fall Meeting, Boston, MA (2016)

16. C. Gong, M. S. Leite*, “Optical response of noble metal alloys,” SPIE Optics and Photonics, San Diego, CA (2016)

15. Z. Jadidi*, C. Gong, M. S. Leite, “Mapping lithium in all-solid-state bat-

teries by time-of-flight secondary-ion mass spectrometry,” REU-NSF Transportation & Electrification Program, College Park, MD (2016)

14. C. Gong*, M. S. Leite, “Nobel metal alloyed thin-films with optical properties on demand,” American Physical Society March Meeting, Baltimore, MD (2016)

13. D. Ha*, C. Gong, M. S. Leite, J. N. Munday, “Dielectric micro-resonator arrays for optical coupling to solar cells,” American Physical Society March Meeting, Baltimore, MD (2016)

12. M. S. Leite*, C. Gong, D. Ruzmetov, A. A. Talin, “In situ analysis of capacity fade in thin-film anodes for high performance Li-ion all-solid-state batteries,” American Physical Society March Meeting, Baltimore, MD (2016)

11. G. Wessler*, C. Gong, M. R. Dias, J. A. Tailon, L. G. Salamanca-Riba, M. S. Leite, “Alloyed noble metal nanoparticles with tunable optical properties,” American Physical Society March Meeting, Baltimore, MD (2016)

10. M. R. Dias*, C. Gong, G. Wessler, M. S. Leite, “Metal alloyed nanostructured with tunable optical properties,” American Physical Society March Meeting, Baltimore, MD (2016)

9. C. Gong, M. S. Leite*, “Alloyed metallic thin-films with tunable dielectric function,” Materials Research Society Fall Meeting, Boston, MA (2015)

8. C. Gong, E. M. Tennyson, J. Garrett, G. Wessler, J. N. Munday, M. S. Leite*, “Mapping the contribution of plasmonic nanoparticles to the Voc of solar cells by scanning probe microscopy,” Materials Research Society Fall Meeting, Boston, MA (2015)

7. C. Gong, A. Chang, E. Cesewski, M. S. Leite*, “Alloyed thin-films and

nanostructures with dielectric function on demand,” SPIE Optics and Photonics, San Diego, CA (2015)

6. C. Yu*, G. Godbey, C. Gong, C. Blythe, M. S. Leite, “Fabrication of 3D self-rolled thin-films for high density energy storage devices,” REU-NSF Transportation & Electrification Program, College Park, MD (2015)

5. C. Blythe*, C. Gong, G. Godbey, C. Yu, M. S. Leite, “Modeling of self-rolling thin-film lithium-ion microbatteries,” REU-NSF Transportation & Electrification Program, College Park, MD (2015)

4. C. Gong*, M. S. Leite, “Nobel metal alloys with tunable optical properties,” Univ. of Maryland ResearchFest, College Park, MD (2015)

3. C. Gong, D. Ruzmetov, N. Bartelt, A. A. Talin, M. S. Leite*, “Al anodes for compact all-solid-state batteries,” Materials Research Society Spring Meeting, San Francisco, CA (2015)

2. C. Gong, A. Chang, J. A. Taillon, E. Cesewski, L. G. Salamanca-Riba, M. S. Leite*, “Alloyed metallic nanostructures with tunable Optical Response for Solar Cells Application,” Materials Research Society Spring Meeting, San Francisco, CA (2015)

1. C. Gong*, A. Pearse, D. Ruzmetov, G. Rubloff, N. C. Bartelt, A. A. Talin, and M. S. Leite, “Mapping capacity loss in Al anodes for ultra-lightweight and compact all-solid-state batteries,” SPIE Defense + Commercial Sensing, Baltimore, MD (2015)

A.2.4 Poster Presentations

18. J. Huddy, C. Gong, M. S. Leite, “Three-Dimensional Analysis of Ion Distributions within Thin-Film All-Solid-State Lithium-Ion Batteries,” REU-NSF Transportation & Electrification Program, College Park, MD (2017)
17. C. Gong, M. R. Dias, M. S. Leite, “Alloyed metallic thin films and nanostructures with tunable optical properties for plasmonics,” American Chemistry Society Fall Meeting, Washington, DC (2017)
16. C. Gong, M. R. Dias, M. S. Leite, “Alloyed thin films and nanoparticles with engineered optical properties for plasmonics,” ResearchFest, College Park, MD (2016)
15. C. Gong, M. R. Dias, M. S. Leite, “Metallic alloys for plasmonics and energy harvesting,” SPIE/IEEE/OSA poster competition, College Park, MD (2016)
14. C. Gong, D. Ruzmetov, A. A. Talin, M. S. Leite, “Large-capacity aluminum electrodes for all-solid-state Li-ion batteries,” Annual Meeting of the Center for Research in Extreme Batteries, College Park, MD (2016)
13. Z. Jadidi, C. Gong, M. S. Leite, “Mapping lithium distribution in thin-film all-solid-state batteries by time-of-flight secondary-ion mass spectrometry,” REU-NSF Transportation & Electrification Symposium, Arlington, VA (2016)
12. Z. Jadidi, C. Gong, M. S. Leite, “Mapping lithium in all-solid-state batteries by time-of-flight secondary-ion mass spectrometry,” REU-NSF Transportation & Electrification Program, College Park, MD (2016)
11. M. R. Dias, C. Gong, G. Wessler, M. S. Leite. “Metal alloyed nanostruc-

tures with on-demand optical response,” Schlumberger Foundation Faculty of the Future Forum. Boston, MA. November 2015.

10. D. Ha, C. Gong, M. S. Leite, J. N. Munday, “Dielectric micro-resonator coatings for photovoltaics,” Materials Research Society Fall Meeting, Boston, MA (2015)

9. C. Yu, G. Godbey, C. Gong, C. Blythe, M. S. Leite, “Fabrication of 3D self-rolled thin-films for high density energy storage devices,” REU-NSF Transportation & Electrification Program, College Park, MD (2015)

8. C. Blythe, C. Gong, G. Godbey, C. Yu, M. S. Leite, “Modeling of self-rolling thin-film lithium-ion microbatteries,” REU-NSF Transportation & Electrification Program, College Park, MD (2015)

7. A. Chang, C. Gong, E. Cesewski, M. S. Leite, “Alloyed metal nanoparticles with modulated optical properties for photovoltaics,” SPIE Defense + Commercial Sensing, Baltimore, MD (2015)

6. C. Gong, M. S. Leite, “Metal alloyed thin-films with tunable optical properties,” SPIE/IEEE/OSA poster competition, College Park, MD (2015)

5. A. Chang, C. Gong, M. S. Leite, “Alloyed metal nanoparticles with modulated optical properties for photovoltaics,” SPIE/IEEE/OSA poster competition, College Park, MD (2015)

4. C. Gong, D. Ruzmetov, N. C. Bartelt, A. A. Talin, M. S. Leite. “High spatial resolution mapping of capacity loss in Al anode all-solid-state batteries,” Materials Research Society Fall Meeting, Boston, MA (2014)

3. C. Gong, A. Chang, D. Ma, E. Tennyson, J. N. Munday, M. S. Leite, “Spec-

troscopy of metal alloyed nanoparticles with tunable optical properties,” Materials Research Society Fall Meeting, Boston, MA (2014)

2. A. Chang, C. Gong, M. S. Leite, “Developing low-loss plasmonic metal alloyed nanoparticles,” Univ. of Maryland Nanoday, College Park, MD (2014)

1. E. M. Tennyson, J. L. Garrett, C. Gong, J. A. Frantz, J. D. Myers, R. Y. Bekele, J. S. Sanghera, J. N. Munday, M. S. Leite, “Assessing local voltage in CIGS solar cells by nanoscale resolved kelvin probe force microscopy and sub-micron photoluminescence,” 40th IEEE Photovoltaic Specialists Conference, Denver, CO (2014)

A.3 Students Mentored during Ph.D.

8. Allen Chang (01/2014 - 07/2015). Now NSF-GRF fellow, PhD student at University of Massachusetts Amherst. Best MSE/UMD researcher award, IREAP Undergraduate Student Award, Outstanding ASPIRE Student Research Award, ASPIRE fellow

7. Ellen Cesewski (06/2014 - 05/2015). IREAP Undergraduate Student Award. Now PhD student at Virginia Tech

6. Garrett Wessler (06/2015 - 06/2016). Now NSF-GRF fellow, PhD student at Duke University. Best MSE/UMD researcher award, ASPIRE fellow

5. Clayton Blythe (summer 2015). Best Student presentation at NSF-REU. Now Machine Learning Engineer at Asurion

4. Cynthia Yu (summer 2015). Best Student presentation at NSF-REU. Now

Battery Engineering Intern at Tesla

3. Zinab Jadidi (06/2016 - 05/2017). Now NSF-GRF fellow, PhD student at UC Berkeley. ASPIRE fellow, Best overall project at NSF-REU

2. Alan Laplan (09/2016 - present). Now NSF-GRF fellow, undergraduate student in UMD. ASPIRE fellow

1. Julia Huddy (summer 2017). Now undergraduate student in Dickinson College. NSF-REU program

Bibliography

- [1] G. V. Naik, V. M. Shalaev, and A. Boltasseva. Alternative plasmonic materials: beyond gold and silver. *Advanced Materials*, 25(24):3264–3294, 2013.
- [2] G. V. Naik, B. Saha, J. Liu, S. M. Saber, E. A. Stach, J. M. K. Irudayaraj, T. D. Sands, V. M. Shalaev, and A. Boltasseva. Epitaxial superlattices with titanium nitride as a plasmonic component for optical hyperbolic metamaterials. *Proceedings of the National Academy of Sciences*, 111(21):7546–7551, 2014.
- [3] C. M. Soukoulis, T. Koschny, P. Tassin, N. Shen, and B. Dastmalchi. What is a good conductor for metamaterials or plasmonics. *Nanophotonics*, 4(1):6974, 2014.
- [4] H. R. Stuart and D. G. Hall. Island size effects in nanoparticle-enhanced photodetectors. *Applied Physics Letters*, 73(26):3815–3817, 1998.
- [5] S. A. Maier. *Plasmonics: fundamentals and applications*. Springer Science & Business Media, 2007.
- [6] L. G. Schulz. The optical constants of silver, gold, copper, and aluminum. I. the absorption coefficient k . *Journal of the Optical Society of America*, 44(5):357–362, 1954.
- [7] E. D. Palik. *Handbook of Optical Constants of Solids II*. Academic Press, 1991.
- [8] H. A. Atwater and A. Polman. Plasmonics for improved photovoltaic devices. *Nature Materials*, 9(3):205–213, 2010.
- [9] G. Neumann and C. Tuijn. *Self-diffusion and impurity diffusion in pure metals: handbook of experimental data*, volume 14. Elsevier, 2011.
- [10] M. L. Brongersma, N. J. Halas, and P. Nordlander. Plasmon-induced hot carrier science and technology. *Nature Nanotechnology*, 10(1):25–34, 2015.
- [11] C. Gong and M. S. Leite. Noble metal alloys for plasmonics. *ACS Photonics*, 3(4):507–513, 2016.
- [12] S. A. Maier, M. L. Brongersma, P. G. Kik, S. Meltzer, A. A. G. Requicha, and H. A. Atwater. Plasmonics a route to nanoscale optical devices. *Advanced Materials*, 13(19):1501–1505, 2001.

- [13] D. K. Gramotnev and S. I. Bozhevolnyi. Plasmonics beyond the diffraction limit. *Nature Photonics*, 4(2):83–91, 2010.
- [14] H. A. Atwater. The promise of plasmonics. *Scientific American*, 296:56–63, 2007.
- [15] D. A. Papaconstantopoulos. Handbook of the band structure of elemental solids, 1986.
- [16] P. R. West, S. Ishii, G. V. Naik, N. K. Emani, V. M. Shalaev, and A. Boltasseva. Searching for better plasmonic materials. *Laser & Photonics Reviews*, 4(6):795–808, 2010.
- [17] A. Boltasseva and H. A. Atwater. Low-loss plasmonic metamaterials. *Science*, 331(6015):290–291, 2011.
- [18] F. Falcone, T. Lopetegui, M. A. G. Laso, J. D. Baena, J. Bonache, M. Beruete, R. Marques, F. Martin, and M. Sorolla. Babinet principle applied to the design of metasurfaces and metamaterials. *Physical Review Letters*, 93(19):197401, 2004.
- [19] C. L. Holloway, E. F. Kuester, J. A. Gordon, J. OHara, J. Booth, and D. R. Smith. An overview of the theory and applications of metasurfaces: The two-dimensional equivalents of metamaterials. *IEEE Antennas and Propagation Magazine*, 54(2):10–35, 2012.
- [20] R. Sundararaman, P. Narang, A. S. Jermyn, I. W. A. Goddard, and H. A. Atwater. Theoretical predictions for hot-carrier generation from surface plasmon decay. *Nature Communications*, 5:5788, 2014.
- [21] T. Gong and J. N. Munday. Angle-independent hot carrier generation and collection using transparent conducting oxides. *Nano Letters*, 15(1):147–152, 2014.
- [22] K. Chen, R. Adato, and H. Altug. Dual-band perfect absorber for multi-spectral plasmon-enhanced infrared spectroscopy. *ACS Nano*, 6(9):7998–8006, 2012.
- [23] C. M. Watts, X. Liu, and W. J. Padilla. Metamaterial electromagnetic wave absorbers. *Advanced Materials*, 24(23):OP98–OP120, 2012.
- [24] L. Huang, D. R. Chowdhury, S. Ramani, M. T. Reiten, S. N. Luo, A. K. Azad, A. J. Taylor, and H. T. Chen. Impact of resonator geometry and its coupling with ground plane on ultrathin metamaterial perfect absorbers. *Applied Physics Letters*, 101(10):101102, 2012.
- [25] E. E. Narimanov and A. V. Kildishev. Optical black hole: Broadband omnidirectional light absorber. *Applied Physics Letters*, 95(4):041106, 2009.

- [26] N. Liu, M. Mesch, T. Weiss, M. Hentschel, and H. Giessen. Infrared perfect absorber and its application as plasmonic sensor. *Nano Letters*, 10(7):2342–2348, 2010.
- [27] K. Aydin, V. E. Ferry, R. M. Briggs, and H. A. Atwater. Broadband polarization-independent resonant light absorption using ultrathin plasmonic super absorbers. *Nature Communications*, 2:517, 2011.
- [28] T. Sndergaard, S. M. Novikov, T. Holmgaard, R. L. Eriksen, J. Beermann, Z. Han, K. Pedersen, and S. I. Bozhevolnyi. Plasmonic black gold by adiabatic nanofocusing and absorption of light in ultra-sharp convex grooves. *Nature Communications*, 3:969, 2012.
- [29] R. Alaei, M. Farhat, C. Rockstuhl, and F. Lederer. A perfect absorber made of a graphene micro-ribbon metamaterial. *Optics Express*, 20(27):28017–28024, 2012.
- [30] N. I. Landy, S. Sajuyigbe, J. J. Mock, D. R. Smith, and W. J. Padilla. Perfect metamaterial absorber. *Physical Review Letters*, 100(20):207402, 2008.
- [31] X. L. Liu, T. Starr, A. F. Starr, and W. J. Padilla. Infrared spatial and frequency selective metamaterial with near-unity absorbance. *Physical Review Letters*, 104(20):207403, 2010.
- [32] M. W. Knight, H. Sobhani, P. Nordlander, and N. J. Halas. Photodetection with active optical antennas. *Science*, 332(6030):702–704, 2011.
- [33] C. Clavero. Plasmon-induced hot-electron generation at nanoparticle/metal-oxide interfaces for photovoltaic and photocatalytic devices. *Nature Photonics*, 8(2):95–103, 2014.
- [34] Q. Guo, G. M. Ford, W. C. Yang, B. C. Walker, E. A. Stach, H. W. Hillhouse, and A. Rakesh. Fabrication of 7.2% efficient CZTSSe solar cells using CZTS nanocrystals. *Journal of the American Chemical Society*, 132(49):17384–17386, 2010.
- [35] D. B. Mitzi, O. Gunawan, T. K. Todorov, K. Wang, and S. Guha. The path towards a high-performance solution-processed kesterite solar cell. *Solar Energy Materials and Solar Cells*, 95(6):1421–1436, 2011.
- [36] F. Dimroth and S. Kurtz. High-efficiency multijunction solar cells. *MRS Bulletin*, 32(03):230–235, 2007.
- [37] M. A. Green. *Third Generation Photovoltaics: Advanced Solar Energy Conversion*. Springer Science & Business Media, 2006.
- [38] M. L. Brongersma, Y. Cui, and S. H. Fan. Light management for photovoltaics using high-index nanostructures. *Nature Materials*, 13(5):451–460, 2014.

- [39] A. Polman and H. A. Atwater. Photonic design principles for ultrahigh-efficiency photovoltaics. *Nature Materials*, 11(3):174–177, 2012.
- [40] J. N. Munday and H. A. Atwater. Large integrated absorption enhancement in plasmonic solar cells by combining metallic gratings and antireflection coatings. *Nano Letters*, 11(6):2195–2201, 2011.
- [41] R. A. Pala, J. White, E. Barnard, J. Liu, and M. L. Brongersma. Design of plasmonic thin-film solar cells with broadband absorption enhancements. *Advanced Materials*, 21(34):3504–3509, 2009.
- [42] J. Wu and Z.M. Wang. *Quantum Dot Solar Cells, Lecture Notes in Nanoscale*. Springer, New York, 2014.
- [43] K. Nakayama, K. Tanabe, and H. A. Atwater. Plasmonic nanoparticle enhanced light absorption in GaAs solar cells. *Applied Physics Letters*, 93(12):121904, 2008.
- [44] N. P. Hylton, X. F. Li, V. Giannini, K. H. Lee, N. J. Ekins-Daukes, J. Loo, D. Vercruyse, P. Van Dorpe, H. Sodabanlu, M. Sugiyama, and S. A. Maier. Loss mitigation in plasmonic solar cells: aluminium nanoparticles for broadband photocurrent enhancements in GaAs photodiodes. *Scientific Reports*, 3:2874, 2013.
- [45] M. W. Knight, L. Liu, Y. Wang, L. Brown, S. Mukherjee, N. S. King, H. O. Everitt, P. Nordlander, and N. J. Halas. Aluminum plasmonic nanoantennas. *Nano Letters*, 12(11):6000–6004, 2012.
- [46] K. R. Catchpole and A. Polman. Plasmonic solar cells. *Optics Express*, 16(26):21793–21800, 2008.
- [47] Y. A. Akimov, K. Ostrikov, and E. P. Li. Surface plasmon enhancement of optical absorption in thin-film silicon solar cells. *Plasmonics*, 4(2):107–113, 2009.
- [48] A. Basch, F. J. Beck, T. Soderstrom, S. Varlamov, and K. R. Catchpole. Combined plasmonic and dielectric rear reflectors for enhanced photocurrent in solar cells. *Applied Physics Letters*, 100(24):243903, 2012.
- [49] F. J. Beck, A. Polman, and K. R. Catchpole. Tunable light trapping for solar cells using localized surface plasmons. *Journal of Applied Physics*, 105(11):114310, 2009.
- [50] F. J. Beck, S. Mokkaapati, and K. R. Catchpole. Plasmonic light-trapping for Si solar cells using self-assembled, Ag nanoparticles. *Progress in Photovoltaics: Research and Applications*, 18(7):500–504, 2010.

- [51] X. Chen, B. Jia, J. K. Saha, B. Cai, N. Stokes, Q. Qiao, Y. Wang, Z. Shi, and M. Gu. Broadband enhancement in thin-film amorphous silicon solar cells enabled by nucleated silver nanoparticles. *Nano Letters*, 12(5):2187–92, 2012.
- [52] S. Mokkaapati, F. J. Beck, A. Polman, and K. R. Catchpole. Designing periodic arrays of metal nanoparticles for light-trapping applications in solar cells. *Applied Physics Letters*, 95(5):053115, 2009.
- [53] H. Tan, R. Santbergen, A. H. Smets, and M. Zeman. Plasmonic light trapping in thin-film silicon solar cells with improved self-assembled silver nanoparticles. *Nano Letters*, 12(8):4070–4076, 2012.
- [54] P. Matheu, S. H. Lim, D. Derkacs, C. McPheeters, and E. T. Yu. Metal and dielectric nanoparticle scattering for improved optical absorption in photovoltaic devices. *Applied Physics Letters*, 93(11):113108, 2008.
- [55] L. Lu, Z. Luo, T. Xu, and L. Yu. Cooperative plasmonic effect of Ag and Au nanoparticles on enhancing performance of polymer solar cells. *Nano Letters*, 13(1):59–64, 2013.
- [56] J. L. Wu, F. C. Chen, Y. S. Hsiao, F. C. Chien, P. Chen, C. H. Kuo, M. H. Huang, and C. S. Hsu. Surface plasmonic effects of metallic nanoparticles on the performance of polymer bulk heterojunction solar cells. *ACS Nano*, 5(2):959–967, 2011.
- [57] F. X. Xie, W. C. H. Choy, C. D. Wang, W. E. I. Sha, and D. S. Fung. Improving the efficiency of polymer solar cells by incorporating gold nanoparticles into all polymer layers. *Applied Physics Letters*, 99(15):153304, 2011.
- [58] J. Yang, J. You, C. C. Chen, W. C. Hsu, H. R. Tan, X. W. Zhang, Z. Hong, and Y. Yang. Plasmonic polymer tandem solar cell. *ACS Nano*, 5(8):6210–6217, 2011.
- [59] K. Kim and D. L. Carroll. Roles of Au and Ag nanoparticles in efficiency enhancement of poly(3-octylthiophene)/C₆₀ bulk heterojunction photovoltaic devices. *Applied Physics Letters*, 87(20):203113, 2005.
- [60] Y. Zhang, Z. Ouyang, N. Stokes, B. Jia, Z. Shi, and M. Gu. Low cost and high performance Al nanoparticles for broadband light trapping in si wafer solar cells. *Applied Physics Letters*, 100(15):151101, 2012.
- [61] M. Castro-Lopez, D. Brinks, R. Sapienza, and N. F. van Hulst. Aluminum for nonlinear plasmonics: Resonance-driven polarized luminescence of Al, Ag, and Au nanoantennas. *Nano Letters*, 11(11):4674–4678, 2011.
- [62] E. Eizner, O. Avayu, R. Ditcovski, and T. Ellenbogen. Aluminum nanoantenna complexes for strong coupling between excitons and localized surface plasmons. *Nano Letters*, 15(9):6215–6221, 2015.

- [63] M. B. Cortie and A. M. McDonagh. Synthesis and optical properties of hybrid and alloy plasmonic nanoparticles. *Chemical Reviews*, 111(6):3713–3735, 2011.
- [64] W. Cao, Y. A. Chang, J. Zhu, S. Chen, and W. A. Oates. Thermodynamic modeling of the Cu-Ag-Au system using the cluster/site approximation. *Intermetallics*, 15(11):1438–1446, 2007.
- [65] S. Link, Z. L. Wang, and M. A. El-Sayed. Alloy formation of gold-silver nanoparticles and the dependence of the plasmon absorption on their composition. *The Journal of Physical Chemistry B*, 103(18):3529–3533, 1999.
- [66] N. E. Motl, E. Ewusi-Annan, I. T. Sines, L. Jensen, and R. E. Schaak. AuCu alloy nanoparticles with tunable compositions and plasmonic properties: Experimental determination of composition and correlation with theory. *The Journal of Physical Chemistry C*, 114(45):19263–19269, 2010.
- [67] M. G. Blaber, M. D. Arnold, and M. J. Ford. A review of the optical properties of alloys and intermetallics for plasmonics. *Journal of Physics: Condensed Matter*, 22(14):143201, 2010.
- [68] J. Rivory. Comparative study of the electronic structure of noble-metal-noble-metal alloys by optical spectroscopy. *Physical Review B*, 15(6):3119–3135, 1977.
- [69] M. Gaudry, J. Lerme, E. Cottancin, M. Pellarin, J. L. Vialle, M. Broyer, B. Prevel, M. Treilleux, and P. Melinon. Optical properties of $(\text{Au}_x\text{Ag}_{1-x})_n$ clusters embedded in alumina: evolution with size and stoichiometry. *Physical Review B*, 64(8):085407, 2001.
- [70] B. R. Cooper, H. Ehrenreich, and H. R. Philipp. Optical properties of noble metals. ii. *Physical Review*, 138(2A):A494, 1965.
- [71] P. B. Johnson and R. W. Christy. Optical constants of the noble metals. *Physical Review B*, 6(12):4370–4379, 1972.
- [72] K. M. McPeak, S. V. Jayanti, S. J. P. Kress, S. Meyer, S. Iotti, A. Rossinelli, and D. J. Norris. Plasmonic films can easily be better: Rules and recipes. *ACS Photonics*, 2(3):326–333, 2015.
- [73] M. N. Obrovac and V. L. Chevrier. Alloy negative electrodes for Li-ion batteries. *Chemical Reviews*, 114(23):11444–11502, 2014.
- [74] M. S. Whittingham. Ultimate limits to intercalation reactions for lithium batteries. *Chemical Reviews*, 114(23):11414–11443, 2014.
- [75] K. Xu. Electrolytes and interphases in Li-ion batteries and beyond. *Chemical Reviews*, 114(23):11503–11618, 2014.

- [76] M S. Whittingham. Electrical energy storage and intercalation chemistry. *Science*, 192(4244):1126–1127, 1976.
- [77] C. Gong, D. Ruzmetov, A. Pearse, D. Ma, J. N. Munday, G. Rubloff, A. A. Talin, and M. S. Leite. Surface/interface effects on high-performance thin-film all-solid-state Li-ion batteries. *ACS Applied Materials & Interfaces*, 7(47):26007–26011, 2015.
- [78] J. F. M. Oudenhoven, L. Baggetto, and P. H. L. Notten. All-solid-state lithium-ion microbatteries: A review of various three-dimensional concepts. *Advanced Energy Materials*, 1(1):10–33, 2011.
- [79] T. H. Kim, J. S. Park, S. K. Chang, S. Choi, J. H. Ryu, and H. K. Song. The current move of lithium ion batteries towards the next phase. *Advanced Energy Materials*, 2(7):860–872, 2012.
- [80] M. Armand and J. M. Tarascon. Building better batteries. *Nature*, 451(7179):652–657, 2008.
- [81] J. B. Goodenough and K. S. Park. The Li-ion rechargeable battery: a perspective. *Journal of the American Chemical Society*, 135(4):1167–1176, 2013.
- [82] P. V. Braun, J. Cho, J. H. Pikul, W. P. King, and H. Zhang. High power rechargeable batteries. *Current Opinion in Solid State and Materials Science*, 16(4):186–198, 2012.
- [83] S. Kirklin, B. Meredig, and C. Wolverton. High-throughput computational screening of new Li-ion battery anode materials. *Advanced Energy Materials*, 3(2):252–262, 2013.
- [84] A. Kraytsberg and Y. Ein-Eli. Higher, stronger, better... A review of 5 volt cathode materials for advanced lithium-ion batteries. *Advanced Energy Materials*, 2(8):922–939, 2012.
- [85] J. Le Bideau, J. B. Ducros, P. Soudan, and D. Guyomard. Solid-state electrode materials with ionic-liquid properties for energy storage: the lithium solid-state ionic-liquid concept. *Advanced Functional Materials*, 21(21):4073–4078, 2011.
- [86] H. Li, Z. X. Wang, L. Q. Chen, and X. J. Huang. Research on advanced materials for Li-ion batteries. *Advanced Materials*, 21(45):4593–4607, 2009.
- [87] J. Li, C. Ma, M. Chi, C. Liang, and N. J. Dudney. Solid electrolyte: the key for high-voltage lithium batteries. *Advanced Energy Materials*, 5:1401408, 2015.
- [88] G. Pistoia. *Lithium-Ion Batteries: Advances and Applications*. Elsevier, 2014.

- [89] R. A. Huggins. *Advanced Batteries: Materials Science Aspects*. Springer, 2008.
- [90] P. G. Bruce, B. Scrosati, and J. M. Tarascon. Nanomaterials for rechargeable lithium batteries. *Angewandte Chemie International Edition*, 47(16):2930–2946, 2008.
- [91] S. J. Harris, A. Timmons, D. R. Baker, and C. Monroe. Direct in situ measurements of Li transport in Li-ion battery negative electrodes. *Chemical Physics Letters*, 485(4-6):265–274, 2010.
- [92] Y. Qi and S. J. Harris. In situ observation of strains during lithiation of a graphite electrode. *Journal of The Electrochemical Society*, 157(6):A741, 2010.
- [93] G. N. Zhu, Y. G. Wang, and Y. Y. Xia. Ti-based compounds as anode materials for Li-ion batteries. *Energy & Environmental Science*, 5(5):6652–6667, 2012.
- [94] Y. G. Gennady, C. John, H. P. Jean, and C. B. Arnold. A model for the behavior of battery separators in compression at different strain/charge rates. *Journall of the Electrochemical Society*, 161:3065–3071, 2014.
- [95] C. K. Chan, H. L. Peng, G. Liu, K. McIlwrath, X. F. Zhang, R. A. Huggins, and Y. Cui. High-performance lithium battery anodes using silicon nanowires. *Nature Nanotechnology*, 3(1):31–35, 2008.
- [96] C. Gong, M. R. S. Dias, G. C. Wessler, J. A. Taillon, L. G. Salamanca-Riba, and M. S. Leite. Near-field optical properties of fully alloyed noble metal nanoparticles. *Advanced Optical Materials*, 5(1):1600568, 2017.
- [97] M. R. S. Dias, C. Gong, Z. A. Benson, and M. S. Leite. Lithography-free, omnidirectional, CMOS-compatible AlCu alloys for thin-film superabsorbers. *Advanced Optical Materials*, 6(2):1700830, 2018.
- [98] E. M. Tennyson, C. Gong, and M. S. Leite. Imaging energy harvesting and storage systems at the nanoscale. *ACS Energy Letters*, 2(12):2761–2777, 2017.
- [99] M. A. Kats, R. Blanchard, P. Genevet, and F. Capasso. Nanometre optical coatings based on strong interference effects in highly absorbing media. *Nature Materials*, 12(1):20–24, 2013.
- [100] A. V. Kildishev, A. Boltasseva, and V. M. Shalaev. Planar photonics with metasurfaces. *Science*, 339(6125):1289, 2013.
- [101] J. Park, J. H. Kang, A. P. Vasudev, D. T. Schoen, H. Kim, E. Hasman, and M. L. Brongersma. Omnidirectional near-unity absorption in an ultrathin planar semiconductor layer on a metal substrate. *ACS Photonics*, 1(9):812–821, 2014.

- [102] B. Y. Zheng, Y. Wang, P. Nordlander, and N. J. Halas. Color-selective and CMOS-compatible photodetection based on aluminum plasmonics. *Advanced Materials*, 26(36):6318–6323, 2014.
- [103] M. Green and S. Pillai. Harnessing plasmonics for solar cells. *Nature Photonics*, 6(3):3, 2012.
- [104] M. B. Cortie, J. Giddings, and A. Dowd. Optical properties and plasmon resonances of titanium nitride nanostructures. *Nanotechnology*, 21(11):115201, 2010.
- [105] D. Amram and E. Rabkin. Core(Fe)-shell(Au) nanoparticles obtained from thin Fe/Au bilayers employing surface segregation. *ACS Nano*, 8(10):10687–10693, 2014.
- [106] D. Rioux, S. Vallieres, S. Besner, P. Munoz, E. Mazur, and M. Meunier. An analytic model for the dielectric function of Au, Ag, and their alloys. *Advanced Optical Materials*, 2(2):176–182, 2014.
- [107] D. Gu, C. Zhang, Y. K. Wu, and L. J. Guo. Ultrasoft and thermally stable silver-based thin films with subnanometer roughness by aluminum doping. *ACS Nano*, 8(10):10343–10351, 2014.
- [108] A. Kosoy, V. Merk, D. Simakov, K. Leosson, S. Kna-Cohen, and S. A. Maier. Gold films: Optical and structural properties of ultra-thin gold films. *Advanced Optical Materials*, 3(1):1, 2015.
- [109] K. DeSilva, A. Gentle, M. Arnold, V. J. Keast, and M. B. Cortie. Dielectric function and its predicted effect on localized plasmon resonances of equiatomic AuCu. *Journal of Physics D: Applied Physics*, 48(21):215304, 2015.
- [110] X. Ding, Y. Zou, and J. Jiang. AuCu₂S heterodimer formation via oxidization of AuCu alloy nanoparticles and in situ formed copper thiolate. *Journal of Materials Chemistry*, 22(43):23169–23174, 2012.
- [111] A. K. Sra and R. E. Schaak. Synthesis of atomically ordered AuCu and AuCu₃ nanocrystals from bimetallic nanoparticle precursors. *Journal of the American Chemical Society*, 126(21):6667–6672, 2004.
- [112] T. Klassen, U. Herr, and R. S. Averback. Ball milling of systems with positive heat of mixing: Effect of temperature in Ag-Cu. *Acta Materialia*, 45(7):2921–2930, 1997.
- [113] H. G. Tompkins, S. Tasic, J. Baker, and D. Convey. Spectroscopic ellipsometry measurements of thin metal films. *Surface and Interface Analysis*, 29(3):179–187, 2000.
- [114] B. Johs and J. S. Hale. Dielectric function representation by B-splines. *Physica Status Solidi (a)*, 205(4):715–719, 2008.

- [115] V. A. Lubarda. On the effective lattice parameter of binary alloys. *Mechanics of Materials*, 35(1):53–68, 2003.
- [116] S. H. Wei, A. A. Mbaye, L. G. Ferreira, and A. Zunger. First-principles calculations of the phase diagrams of noble metals: Cu-Au, Cu-Ag, and Ag-Au. *Physical Review B*, 36(8):4163, 1987.
- [117] J. Song, M. Zhou, R. Yi, T. Xu, M. L. Gordin, D. Tang, Z. Yu, M. Regula, and D. Wang. Interpenetrated gel polymer binder for high-performance silicon anodes in lithium-ion batteries. *Advanced Functional Materials*, 24(37):5904–5910, 2014.
- [118] O. Pluchery, R. Vayron, and K. Van. Laboratory experiments for exploring the surface plasmon resonance. *European Journal of Physics*, 32(2):585, 2011.
- [119] K. Matsubara, S. Kawata, and S. Minami. Optical chemical sensor based on surface plasmon measurement. *Applied Optics*, 27(6):1160–1163, 1988.
- [120] L. Novotny and B. Hecht. *Principles of nano-optics*. Cambridge university press, 2012.
- [121] Z. Feng, C. Jiang, Y. He, S. Chu, G. Chu, R. Peng, and D. Li. Widely adjustable and quasi-reversible electrochromic device based on core-shell Au-Ag plasmonic nanoparticles. *Advanced Optical Materials*, 2(12):1174–1180, 2014.
- [122] S. Pillai, K. R. Catchpole, T. Trupke, and M. A. Green. Surface plasmon enhanced silicon solar cells. *Journal of Applied Physics*, 101(9):093105, 2007.
- [123] S. Nie and S. R. Emory. Probing single molecules and single nanoparticles by surface-enhanced Raman scattering. *Science*, 275(5303):1102–1106, 1997.
- [124] K. P. Garca, K. Zarschler, L. Barbaro, J. A. Barreto, W. O’Malley, L. Spiccia, H. Stephan, and B. Graham. Zwitterionic-coated stealth nanoparticles for biomedical applications: Recent advances in countering biomolecular corona formation and uptake by the mononuclear phagocyte system. *Small*, 10(13):2516–2529, 2014.
- [125] C. T. Campbell. Ultrathin metal films and particles on oxide surfaces: structural, electronic and chemisorptive properties. *Surface Science Reports*, 27(13):1–111, 1997.
- [126] W. Rechberger, A. Hohenau, A. Leitner, J. R. Krenn, B. Lamprecht, and F. R. Aussenegg. Optical properties of two interacting gold nanoparticles. *Optics Communications*, 220(1):137–141, 2003.
- [127] S. Graells, R. Alcubilla, G. Badenes, and R. Quidant. Growth of plasmonic gold nanostructures by electron beam induced deposition. *Applied Physics Letters*, 91(12):121112, 2007.

- [128] F. A. A. Nugroho, B. Iandolo, J. B. Wagner, and C. Langhammer. Bottom-up nanofabrication of supported noble metal alloy nanoparticle arrays for plasmonics. *ACS Nano*, 10(2):2871–2879, 2016.
- [129] A. Genc, J. Patarroyo, J. Sancho-Parramon, R. Arenal, M. Duchamp, E. E. Gonzalez, L. Henrard, N. G. Bastus, R. E. Dunin-Borkowski, V. F. Puentes, and J. Arbiol. Tuning the plasmonic response up: Hollow cuboid metal nanostructures. *ACS Photonics*, 3(5):770–779, 2016.
- [130] Y. Hashimoto, G. Seniutinas, A. Balytis, S. Juodkazis, and Y. Nishijima. Au-Ag-Cu nano-alloys: tailoring of permittivity. *Scientific Reports*, 6:25010, 2016.
- [131] Y. Liu and X. Zhang. Metamaterials: a new frontier of science and technology. *Chemical Society Reviews*, 40(5):2494–2507, 2011.
- [132] C. Zhao, J. Zhang, and Y. Liu. Light manipulation with encoded plasmonic nanostructures. *EPJ Applied Metamaterials*, 1:6, 2014.
- [133] M. Xu, J. Feng, Y. S. Liu, Y. Jin, H. Y. Wang, and H. B. Sun. Effective and tunable light trapping in bulk heterojunction organic solar cells by employing Au-Ag alloy nanoparticles. *Applied Physics Letters*, 105(15):153303, 2014.
- [134] S. Liu, R. Jiang, P. You, X. Zhu, J. Wang, and F. Yan. Au/Ag core-shell nanocuboids for high-efficiency organic solar cells with broadband plasmonic enhancement. *Energy & Environmental Science*, 9(3):898–905, 2016.
- [135] R. Yu, P. Mazumder, N. F. Borrelli, A. Carrilero, D. S. Ghosh, R. A. Maniyara, D. Baker, F. J. Garca de Abajo, and V. Pruneri. Structural coloring of glass using dewetted nanoparticles and ultrathin films of metals. *ACS Photonics*, 3(7):1194–1201, 2016.
- [136] C. W. Hsu, B. Zhen, W. Qiu, O. Shapira, B. G. DeLacy, J. D. Joannopoulos, and M. Soljacic. Transparent displays enabled by resonant nanoparticle scattering. *Nature Communications*, 5:3152, 2014.
- [137] J. Olson, A. Manjavacas, L. Liu, W. S. Chang, B. Foerster, N. S. King, M. W. Knight, P. Nordlander, N. J. Halas, and S. Link. Vivid, full-color aluminum plasmonic pixels. *Proceedings of the National Academy of Sciences*, 111(40):14348–14353, 2014.
- [138] J. H. Liu, A. Q. Wang, Y. S. Chi, H. P. Lin, and C. Y. Mou. Synergistic effect in an AuAg alloy nanocatalyst: CO oxidation. *The Journal of Physical Chemistry B*, 109(1):40–43, 2005.
- [139] G. Guisbiers, R. Mendoza-Cruz, L. Bazan-Diaz, J. J. Velazquez-Salazar, R. Mendoza-Perez, J. A. Robledo-Torres, J. L. Rodriguez-Lopez, J. M.n Montejano-Carrizales, R. L. Whetten, and M. Jose-Yacamán. Electrum, the goldsilver alloy, from the bulk scale to the nanoscale: Synthesis, properties, and segregation rules. *ACS Nano*, 10(1):188–198, 2016.

- [140] S. Verma, B. T. Rao, A. P. Detty, V. Ganesan, D. M. Phase, S. K. Rai, A. Bose, S. C. Joshi, and L. M. Kukreja. Surface plasmon resonances of Ag-Au alloy nanoparticle films grown by sequential pulsed laser deposition at different compositions and temperatures. *Journal of Applied Physics*, 117(13):133105, 2015.
- [141] D. Rioux and M. Meunier. Seeded growth synthesis of composition and size-controlled gold-silver alloy nanoparticles. *The Journal of Physical Chemistry C*, 119:13160, 2015.
- [142] E. Thouti, N. Chander, V. Dutta, and V. K. Komarala. Optical properties of Ag nanoparticle layers deposited on silicon substrates. *Journal of Optics*, 15(3):035005, 2013.
- [143] M. Schmid, J. Grandidier, and H. A. Atwater. Scanning near-field optical microscopy on dense random assemblies of metal nanoparticles. *Journal of Optics*, 15(12):125001, 2013.
- [144] J. Okumu, C. Dahmen, A. N. Sprafke, M. Luysberg, G. Von Plessen, and M. Wuttig. Photochromic silver nanoparticles fabricated by sputter deposition. *Journal of Applied Physics*, 97(9):094305, 2005.
- [145] Carl V. Thompson. Solid-state dewetting of thin films. *Annual Review of Materials Research*, 42(1):399–434, 2012.
- [146] T. Zhai, Y. Wang, H. Liu, and X. Zhang. Large-scale fabrication of flexible metallic nanostructure pairs using interference ablation. *Optics Express*, 23(2):1863–1870, 2015.
- [147] S. Sabine, G. P. Vera, M. Mael, and B. Rabah. Gold island films on indium tin oxide for localized surface plasmon sensing. *Nanotechnology*, 19(19):195712, 2008.
- [148] M. S. Leite, T. I. Kamins, R. S. Williams, and G. Medeiros-Ribeiro. Intermixing during ripening in GeSi incoherent epitaxial nanocrystals. *The Journal of Physical Chemistry C*, 116(1):901–907, 2011.
- [149] Y. Nishijima, J. B. Khurgin, L. Rosa, H. Fujiwara, and S. Juodkazis. Tunable raman selectivity via randomization of a rectangular pattern of nanodisks. *ACS Photonics*, 1(10):1006–1012, 2014.
- [150] Y. Nishijima, J. B. Khurgin, L. Rosa, H. Fujiwara, and S. Juodkazis. Randomization of gold nano-brick arrays: a tool for SERS enhancement. *Optics Express*, 21(11):13502–13514, 2013.
- [151] H. Baker and H. Okamoto. *ASM Handbook, Volume 03 - Alloy Phase Diagrams*. ASM International, Materials Park, 1992.

- [152] A. I. Fernnndez-Dominguez, F. J. Garcia-Vidal, and L. Martin-Moreno. Unrelenting plasmons. *Nature Photonics*, 11(1):8, 2017.
- [153] D. Wang, A. Yang, W. Wang, Y. Hua, R. D. Schaller, G. C. Schatz, and T. W. Odom. Band-edge engineering for controlled multi-modal nanolasing in plasmonic superlattices. *Nature Nanotechnology*, 12(9):889, 2017.
- [154] J. Homola, S. S. Yee, and G. Gauglitz. Surface plasmon resonance sensors. *Sensors and Actuators B: Chemical*, 54(1):3–15, 1999.
- [155] S. Tu, D. Rioux, J. Perreault, D. Brouard, and M. Meunier. Fluorescence and scattering dual-mode multiplexed imaging with goldsilver alloy core silica shell nanoparticles. *The Journal of Physical Chemistry C*, 121(16):8944–8951, 2017.
- [156] R. Proietti Z., F. Bisio, G. Das, G. Maidecchi, M. Caminale, C. D. Vu, F. De Angelis, E. Di Fabrizio, A. Toma, and M. Canepa. Plasmonic color-graded nanosystems with achromatic subwavelength architectures for light filtering and advanced sers detection. *ACS Applied Materials & Interfaces*, 8(12):8024–8031, 2016.
- [157] W. L. Barnes, A. Dereux, and T. W. Ebbesen. Surface plasmon subwavelength optics. *Nature*, 424(6950):824–830, 2003.
- [158] M. B. Ross, J. C. Ku, B. Lee, C. A. Mirkin, and G. C. Schatz. Plasmonic metallurgy enabled by DNA. *Advanced Materials*, 28(14):2790–2794, 2016.
- [159] H. Y. Hong, J. S. Ha, S. Lee, and J. H. Park. Effective propagation of surface plasmon polaritons on graphene-protected single-crystalline silver films. *ACS Applied Materials & Interfaces*, 9(5):5014–5022, 2017.
- [160] R. Yu, L. M. Liz-Marzan, and F. J. G. de Abajo. Universal analytical modeling of plasmonic nanoparticles. *Chemical Society Reviews*, 46(22):6710–6724, 2017.
- [161] C. Zhang, N. Kinsey, L. Chen, C. Ji, M. Xu, M. Ferrera, X. Pan, V. M. Shalaev, A. Boltasseva, and L J. Guo. High-performance doped silver films: Overcoming fundamental material limits for nanophotonic applications. *Advanced Materials*, 29(19), 2017.
- [162] W. Zhou, M. Dridi, J. Y. Suh, C. H. Kim, M. R. Wasielewski, G. C. Schatz, and T. W. Odom. Lasing action in strongly coupled plasmonic nanocavity arrays. *Nature Nanotechnology*, 8(7):506, 2013.
- [163] S. Dai, Q. Ma, M. K. Liu, T. Andersen, Z. Fei, M. D. Goldflam, M. Wagner, K. Watanabe, T. Taniguchi, and M. Thiemens. Graphene on hexagonal boron nitride as a tunable hyperbolic metamaterial. *Nature Nanotechnology*, 10(8):682686, 2015.

- [164] O. Pena-Rodriguez, M. Caro, A. Rivera, J. Olivares, J. M. Perlado, and A. Caro. Optical properties of Au-Ag alloys: An ellipsometric study. *Optical Materials Express*, 4(2):403–410, 2014.
- [165] P. Chen, X. Liu, J. L. Hedrick, Z. Xie, S. Wang, Q. Lin, M. C. Hersam, V. P. Dravid, and C. A. Mirkin. Polyelemental nanoparticle libraries. *Science*, 352(6293):1565–1569, 2016.
- [166] A. Herz, M. Friak, D. Rossberg, M. Hentschel, F. Theska, D. Wang, D. Holec, M. Sob, O. Schneeweiss, and P. Schaaf. Facet-controlled phase separation in supersaturated Au-Ni nanoparticles upon shape equilibration. *Applied Physics Letters*, 107(7):073109, 2015.
- [167] G. Chen, R. Gao, Y. Zhao, Z. Li, G. I. N. Waterhouse, R. Shi, J. Zhao, M. Zhang, L. Shang, and G. Sheng. Alumina-supported CoFe alloy catalysts derived from layered-double-hydroxide nanosheets for efficient photothermal CO₂ hydrogenation to hydrocarbons. *Advanced Materials*, 30(3), 2018.
- [168] J. Li, H. Yin, X. Li, E. Okunishi, Y. Shen, J. He, Z. Tang, W. Wang, E. Ycelen, and C. Li. Surface evolution of a Pt-Pd-Au electrocatalyst for stable oxygen reduction. *Nature Energy*, 2:17111, 2017.
- [169] A. Holewinski, J. Idrobo, and S. Linic. High-performance AgCo alloy catalysts for electrochemical oxygen reduction. *Nature Chemistry*, 6(9):828–834, 2014.
- [170] J. Kim, C. Roh, S. K. Sahoo, S. Yang, J. n Bae, J. W. Han, and H. Lee. Highly durable platinum single-atom alloy catalyst for electrochemical reactions. *Advanced Energy Materials*, 8(1):1701476, 2018.
- [171] T. T. Ehler and L. J. Noe. Surface plasmon studies of thin silver/gold bimetallic films. *Langmuir*, 11(10):4177–4179, 1995.
- [172] C. Zhong, K. E. Ballantine, C. Kervick, C. M. Smith, D. Mullarkey, I. V. Shvets, J. F. Donegan, and D. McCloskey. Mapping of surface plasmon dispersion in thin AgAu layered composite films. *Journal of the Optical Society of America B*, 33(4):566–573, 2016.
- [173] M. Ives, T. M. Autry, S. T. Cundiff, and G. Nardin. Direct imaging of surface plasmon polariton dispersion in gold and silver thin films. *Journal of the Optical Society of America B*, 33(7):C17–C21, 2016.
- [174] G. Schider, J. R. Krenn, A. Hohenau, H. Ditlbacher, A. Leitner, F. R. Aussenegg, W. L. Schaich, I. Puscasu, B. Monacelli, and G. Boreman. Plasmon dispersion relation of Au and Ag nanowires. *Physical Review B*, 68(15):155427, 2003.
- [175] B. H. Ong, X. Yuan, S. C. Tjin, J. Zhang, and H. M. Ng. Optimised film thickness for maximum evanescent field enhancement of a bimetallic film

- surface plasmon resonance biosensor. *Sensors and Actuators B: Chemical*, 114(2):1028–1034, 2006.
- [176] S. Y. Park and D. Stroud. Surface-plasmon dispersion relations in chains of metallic nanoparticles: An exact quasistatic calculation. *Physical Review B*, 69(12):125418, 2004.
- [177] Z. Liu, D. Ji, X. Zeng, H. Song, J. Liu, S. Jiang, and Q. Gan. Surface dispersion engineering of AgAu alloy films. *Applied Physics Express*, 8(4):042601, 2015.
- [178] E. Kretschmann and H. Raether. Radiative decay of non radiative surface plasmons excited by light. *Zeitschrift fur Naturforschung A: Journal of Physical Sciences*, 23(12):2135–2136, 1968.
- [179] E. Hecht. Optics, 4th. *International edition, Addison-Wesley, San Francisco*, 3, 2002.
- [180] H. Raether. *Surface plasmons on smooth and rough surfaces and on gratings*. Surface plasmons on smooth and rough surfaces and on gratings. Springer, 1988.
- [181] C. Gao, Y. Hu, M. Wang, M. Chi, and Y. Yin. Fully alloyed Ag/Au nanospheres: combining the plasmonic property of Ag with the stability of Au. *Journal of the American Chemical Society*, 136(20):7474–7479, 2014.
- [182] J. D. Jackson. *Classical electrodynamics*. John Wiley & Sons, 2007.
- [183] I. H. Malitson. Interspecimen comparison of the refractive index of fused silica. *Journal of the Optical Society of America*, 55(10):1205–1209, 1965.
- [184] J. A. Dionne, L. A. Sweatlock, H. A. Atwater, and A. Polman. Planar metal plasmon waveguides: frequency-dependent dispersion, propagation, localization, and loss beyond the free electron model. *Physical Review B: Condensed Matter*, 72(7):075405, 2005.
- [185] T. Nahm, S. J. Oh, and S. M. Chung. Study of the electronic structure of disordered Au-Ag alloys using synchrotron radiation. *Journal of Electron Spectroscopy and Related Phenomena*, 78:127–130, 1996.
- [186] T. K. Sham, A. Bzowski, M. Kuhn, and C. C. Tyson. Observations on the d-band width of Au-Ag and Au-Cu alloys. *Solid State Communications*, 80(1):29–32, 1991.
- [187] A. Bzowski, M. Kuhn, T. K. Sham, J. A. Rodriguez, and J. Hrbek. Electronic structure of Au-Ag bimetallics: Surface alloying on Ru (001). *Physical Review B: Condensed Matter*, 59(20):13379, 1999.
- [188] J. M. Soler, E. Artacho, J. D. Gale, A. Garcia, J. Junquera, P. Ordejon, and D. Sanchez-Portal. The SIESTA method for ab initio order-N materials simulation. *Journal of Physics: Condensed Matter*, 14(11):2745, 2002.

- [189] L. J. Krayner, E. M. Tennyson, M. S. Leite, and J. N. Munday. Near-IR imaging based on hot carrier generation in nanometer-scale optical coatings. *ACS Photonics*, 5(2):306311, 2018.
- [190] L. Wang, Z. Zeng, C. Ma, Y. Liu, M. Giroux, M. Chi, J. Jin, J. Greeley, and C. Wang. Plating precious metals on nonprecious metal nanoparticles for sustainable electrocatalysts. *Nano Letters*, 17(6):3391–3395, 2017.
- [191] C. Zhu, Q. Shi, S. Fu, J. Song, H. Xia, D. Du, and Y. Lin. Efficient synthesis of MCu (M= Pd,Pt, and Au) aerogels with accelerated gelation kinetics and their high electrocatalytic activity. *Advanced Materials*, 28(39):8779–8783, 2016.
- [192] J. Chastain, R. C. King, and J. Moulder. *Handbook of X-ray photoelectron spectroscopy: a reference book of standard spectra for identification and interpretation of XPS data*. Physical Electronics Division, Perkin-Elmer Corporation Eden Prairie, Minnesota, 1992.
- [193] S. J. Clark, M. D. Segall, C. J. Pickard, P. J. Hasnip, M. I. J. Probert, K. Refson, and M. C. Payne. First principles methods using CASTEP. *Zeitschrift fur Kristallographie-Crystalline Materials*, 220(5/6):567–570, 2005.
- [194] B. G. Pfrommer, M. Cote, S. G. Louie, and M. Cohen. Relaxation of crystals with the quasi-newton method. *Journal of Computational Physics*, 131:233, 1997.
- [195] J. P. Perdew, K. Burke, and M. Ernzerhof. Generalized gradient approximation made simple. *Physical Review Letters*, 77(18):3865, 1996.
- [196] H. J. Monkhorst and J. D. Pack. Special points for Brillouin-zone integrations. *Physical Review B*, 13(12):5188, 1976.
- [197] M. Valenti, A. Venugopal, D. Tordera, M. P. Jonsson, G. Biskos, A. Schmidt-Ott, and W. A. Smith. Hot carrier generation and extraction of plasmonic alloy nanoparticles. *ACS Photonics*, 4(5):1146–1152, 2017.
- [198] S. Kim, H. Wakatsuchi, J. J. Rushton, and D. F. Sievenpiper. Switchable nonlinear metasurfaces for absorbing high power surface waves. *Applied Physics Letters*, 108(4):041903, 2016.
- [199] K. F. MacDonald, Z. L. Samson, M. I. Stockman, and N. I. Zheludev. Ultrafast active plasmonics. *Nature Photonics*, 3(1):55–58, 2009.
- [200] R. Walter, A. Tittl, A. Berrier, F. Sterl, T. Weiss, and H. Giessen. Large-area low-cost tunable plasmonic perfect absorber in the near infrared by colloidal etching lithography. *Advanced Optical Materials*, 3(3):398–403, 2015.

- [201] T. D. Dao, S. Ishii, T. Yokoyama, T. Sawada, R. P. Sugavaneshwar, K. Chen, Y. Wada, T. Nabatame, and T. Nagao. Hole array perfect absorbers for spectrally selective midwavelength infrared pyroelectric detectors. *ACS Photonics*, 3(7):1271–1278, 2016.
- [202] M. Farhat, T. C. Cheng, K. Q. Le, M. M. Cheng, H. Bagci, and P. Y. Chen. Mirror-backed dark alumina: A nearly perfect absorber for thermoelectronics and thermophotovoltaics. *Scientific Reports*, 6:19984, 2016.
- [203] Z. J. Coppens, I. I. Kravchenko, and J. G. Valentine. Lithography-free large-area metamaterials for stable thermophotovoltaic energy conversion. *Advanced Optical Materials*, 4(5):671–676, 2016.
- [204] C. Y. Yang, C. G. Ji, W. D. Shen, K. T. Lee, Y. Zhang, X. Liu, and L. J. Guo. Compact multilayer film structures for ultrabroadband, omnidirectional, and efficient absorption. *ACS Photonics*, 3(4):590–596, 2016.
- [205] J. Perini and L. S. Cohen. Design of broad-band radar-absorbing materials for large angles of incidence. *IEEE Transactions on Electromagnetic Compatibility*, 35(2):223–230, 1993.
- [206] Y. J. Yoo, S. Ju, S. Y. Park, Y. JuKim, J. Bong, T. Lim, K. W. Kim, J. Y. Rhee, and Y. Lee. Metamaterial absorber for electromagnetic waves in periodic water droplets. *Scientific Reports*, 5:14018, 2015.
- [207] E. Knott, J. F. Shaeffer, and M. T. Tuley. *Radar Cross Section*. Scitech, Raleigh, 2nd ed edition, 2004.
- [208] G. T. Ruck, D. E. Barrick, and W. D. Stuart. *Radar Cross Section Handbook*. Plenum, New York, 1970.
- [209] Y. Radi, C. R. Simovski, and S. A. Tretyakov. Thin perfect absorbers for electromagnetic waves: Theory, design, and realizations. *Physical Review Applied*, 3(3):037001, 2015.
- [210] A. Tittl, P. Mai, R. Taubert, D. Dregely, N. Liu, and H. Giessen. Palladium-based plasmonic perfect absorber in the visible wavelength range and its application to hydrogen sensing. *Nano Letters*, 11(10):4366–4369, 2011.
- [211] G. M. Akselrod, J. Huang, T. B. Hoang, P. T. Bowen, L. Su, D. R. Smith, and M. H. Mikkelsen. Large-area metasurface perfect absorbers from visible to near-infrared. *Advanced Materials*, 27(48):8028–8034, 2015.
- [212] Y. Chen, X. Li, X. Luo, S. A. Maier, and M. Hong. Tunable near-infrared plasmonic perfect absorber based on phase-change materials. *Photonics Research*, 3(3):54–57, 2015.

- [213] D. Hasan, P. Pitchappa, J. Wang, T. Wang, B. Yang, C. P. Ho, and C. Lee. Novel CMOS-compatible MoAlNMo platform for metamaterial-based mid-IR absorber. *ACS Photonics*, 4(2):302–315, 2017.
- [214] X. G. Zhao, J. D. Zhang, K. B. Fan, G. W. Duan, G. D. Metcalfe, M. I. Wraback, X. Zhang, and R. D. Averitt. Nonlinear terahertz metamaterial perfect absorbers using GaAs. *Photonics Research*, 4(3):A16–A21, 2016.
- [215] J. Yang, C. Gong, L. Sun, P. Chen, L. Lin, and W. Liu. Tunable reflecting terahertz filter based on chirped metamaterial structure. *Scientific Reports*, 6:38732, 2016.
- [216] J. B. You, W. J. Lee, D. Won, and K. Yu. Multiband perfect absorbers using metal-dielectric films with optically dense medium for angle and polarization insensitive operation. *Optics Express*, 22(7):8339–8348, 2014.
- [217] H. Song, L. Guo, Z. Liu, K. Liu, X. Zeng, D. Ji, N. Zhang, H. Hu, S. Jiang, and Q. Gan. Nanocavity enhancement for ultra-thin film optical absorber. *Advanced Materials*, 26(17):2737–2743, 2014.
- [218] H. Kocer, S. Butun, Z. Li, and K. Aydin. Reduced near-infrared absorption using ultra-thin lossy metals in Fabry-Perot cavities. *Scientific Reports*, 5:8157, 2015.
- [219] M. Yan. Metalinsulator-metal light absorber: a continuous structure. *Journal of Optics*, 15(2):025006, 2013.
- [220] S. Shu, Z. Li, and Y. Y. Li. Triple-layer Fabry-Perot absorber with near-perfect absorption in visible and near-infrared regime. *Optics Express*, 21(21):25307–25315, 2013.
- [221] W. Streyer, S. Law, G. Rooney, T. Jacobs, and D. Wasserman. Strong absorption and selective emission from engineered metals with dielectric coatings. *Optics Express*, 21(7):9113–9122, 2013.
- [222] S. T. Yen and P. K. Chung. Far-infrared quasi-monochromatic perfect absorption in a thin GaAs film on gold. *Optics Letters*, 40(16):3877–3880, 2015.
- [223] J. W. Cleary, R. Soref, and J. R. Hendrickson. Long-wave infrared tunable thin-film perfect absorber utilizing highly doped silicon-on-sapphire. *Optics Express*, 21(16):19363–74, 2013.
- [224] N. Kinsey, M. Ferrera, V. M. Shalaev, and A. Boltasseva. Examining nanophotonics for integrated hybrid systems: a review of plasmonic interconnects and modulators using traditional and alternative materials. *Journal of the Optical Society of America B*, 32(1):121–142, 2015.
- [225] J. Valentine, J. Li, T. Zentgraf, G. Bartal, and X. Zhang. An optical cloak made of dielectrics. *Nature Materials*, 8(7):568–571, 2009.

- [226] M. A. Kats and F. Capasso. Optical absorbers based on strong interference in ultra-thin films. *Laser & Photonics Reviews*, 10(5):735–749, 2016.
- [227] V. Fournee, I. Mazin, D. A. Papaconstantopoulos, and E. Belin-Ferre. Electronic structure calculations of Al-Cu alloys: Comparison with experimental results on Hume-Rothery phases. *Philosophical Magazine Part B*, 79(2):205–221, 1999.
- [228] Y. Jiang, S. Pillai, and M. A. Green. Realistic silver optical constants for plasmonics. *Scientific Reports*, 6:30605, 2016.
- [229] H. Reddy, U. Guler, K. Chaudhuri, A. Dutta, A. V. Kildishev, V. M. Shalaev, and A. Boltasseva. Temperature-dependent optical properties of single crystalline and polycrystalline silver thin films. *ACS Photonics*, 2017.
- [230] Y. Peng, W. Jiang, A. Eric, G. Alexander, and W. Zhiming. Dual-band absorber for multispectral plasmon-enhanced infrared photodetection. *Journal of Physics D: Applied Physics*, 49(36):365101, 2016.
- [231] T. B. Massalski. The AlCu (aluminum-copper) system. *Bulletin of Alloy Phase Diagrams*, 1(1):27–33, 1980.
- [232] F. E. Luborsky. *Amorphous Metallic Alloys (Butterworths monographs in materials)*. Butterworth & Co (Publishers) Ltd., 1983.
- [233] M. S. Whittingham. Lithium batteries and cathode materials. *Chemical Reviews*, 104(10):4271–4302, 2004.
- [234] A. Magasinski, P. Dixon, B. Hertzberg, A. Kvit, J. Ayala, and G. Yushin. High-performance lithium-ion anodes using a hierarchical bottom-up approach. *Nature Materials*, 9(4):353–358, 2010.
- [235] N. J. Dudney. Solid-state thin-film rechargeable batteries. *Materials Science and Engineering: B*, 116(3):245–249, 2005.
- [236] E. M. Erickson, C. Ghanty, and D. Aurbach. New horizons for conventional lithium ion battery technology. *The Journal of Physical Chemistry Letters*, 5(19):3313–3324, 2014.
- [237] D. Ruzmetov, V. P. Oleshko, P. M. Haney, H. J. Lezec, K. Karki, K. H. Baloch, A. K. Agrawal, A. V. Davydov, S. Krylyuk, Y. Liu, J. Y. Huang, M. Tanase, J. Cumings, and A. A. Talin. Electrolyte stability determines scaling limits for solid-state 3D Li ion batteries. *Nano Letters*, 12(1):505–511, 2012.
- [238] V. P. Oleshko, T. Lam, D. Ruzmetov, P. Haney, H. J. Lezec, A. V. Davydov, S. Krylyuk, J. Cumings, and A. A. Talin. Miniature all-solid-state heterostructure nanowire Li-ion batteries as a tool for engineering and structural diagnostics of nanoscale electrochemical processes. *Nanoscale*, 6(20):11756–11768, 2014.

- [239] F. Orsini, A. Du Pasquier, B. Beaudoin, J. M. Tarascon, M. Trentin, N. Langenhuizen, E. De Beer, and P. Notten. In situ scanning electron microscopy (SEM) observation of interfaces within plastic lithium batteries. *Journal of Power Sources*, 76(1):19–29, 1998.
- [240] M. S. Leite, D. Ruzmetov, Z. Li, L. A. Bendersky, N. C. Bartelt, A. Kolmakov, and A. A. Talin. Insights into capacity loss mechanisms of all-solid-state Li-ion batteries with Al anodes. *Journal of Materials Chemistry A*, 2(48):20552–20559, 2014.
- [241] D. Santhanagopalan, D. Qian, T. McGilvray, Z. Wang, F. Wang, F. Camino, J. Graetz, N. Dudney, and Y. S. Meng. Interface limited lithium transport in solid-state batteries. *The Journal of Physical Chemistry Letters*, 5(2):298–303, 2013.
- [242] C. Gong, Y. J. Bai, J. Feng, R. Tang, Y. X. Qi, N. Lun, and R. H. Fan. Enhanced electrochemical performance of FeWO_4 by coating nitrogen-doped carbon. *ACS Applied Materials & Interfaces*, 5(10):4209–4215, 2013.
- [243] A. Brazier, L. Dupont, L. Dantras-Laffont, N. Kuwata, J. Kawamura, and J. M. Tarascon. First cross-section observation of an all solid-state lithium ion nanobattery by transmission electron microscopy. *Chemistry of Materials*, 20(6):2352–2359, 2008.
- [244] X. H. Liu and J. Y. Huang. In situ TEM electrochemistry of anode materials in lithium ion batteries. *Energy & Environmental Science*, 4(10):3844–3860, 2011.
- [245] M. E. Holtz, Y. Yu, D. Gunceler, J. Gao, R. Sundararaman, K. A. Schwarz, T. A. Arias, H. D. Abrua, and D. A. Muller. Nanoscale imaging of lithium ion distribution during in situ operation of battery electrode and electrolyte. *Nano Letters*, 14(3):1453–1459, 2014.
- [246] N. S. Hudak and D. L. Huber. Size effects in the electrochemical alloying and cycling of electrodeposited aluminum with lithium. *Journal of The Electrochemical Society*, 159(5):A688, 2012.
- [247] M. J. Lindsay, G. X. Wang, and H. K. Liu. Al-based anode materials for Li-ion batteries. *Journal of Power Sources*, 119:84–87, 2003.
- [248] M. C. Lin, M. Gong, B. Lu, Y. Wu, D. Y. Wang, M. Guan, M. Angell, C. Chen, J. Yang, B. J. Hwang, and H. Dai. An ultrafast rechargeable aluminium-ion battery. *Nature*, 520(7547):324–328, 2015.
- [249] Y. Liu, N. S. Hudak, D. L. Huber, S. J. Limmer, J. P. Sullivan, and J. Y. Huang. In situ transmission electron microscopy observation of pulverization of aluminum nanowires and evolution of the thin surface Al_2O_3 layers during lithiation-delithiation cycles. *Nano Letters*, 11(10):4188–94, 2011.

- [250] N. Cabrera and N. F. Mott. Theory of the oxidation of metals. *Reports on progress in physics*, 12(1):163–184, 1949.
- [251] H. Magnusson and K. Frisk. Self-diffusion and impurity diffusion in the hydrogen, oxygen, sulphur and phosphorous in copper. *Swedish Nuclear Waste Management Company Technical Report TR-13-24*, 2013.
- [252] W. J. Zhang. A review of the electrochemical performance of alloy anodes for lithium-ion batteries. *Journal of Power Sources*, 196(1):13–24, 2011.
- [253] P. R. Abel, Y. M. Lin, H. Celio, A. Heller, and C. B. Mullins. Improving the stability of nanostructured silicon thin film lithium ion battery anodes through their controlled oxidation. *ACS Nano*, 6(3):2506–2516, 2012.
- [254] G. A. Tritsarlis, K. Zhao, O. U. Okeke, and E. Kaxiras. Diffusion of lithium in bulk amorphous silicon: A theoretical study. *The Journal of Physical Chemistry C*, 116(42):22212–22216, 2012.
- [255] B. A. Korgel. Nanomaterials developments for higher-performance lithium ion batteries. *The Journal of Physical Chemistry Letters*, 5(4):749–750, 2014.
- [256] R. Yi, F. Dai, M. L. Gordin, H. Sohn, and D. Wang. Influence of silicon nanoscale building blocks size and carbon coating on the performance of micro-sized Si-C composite Li-ion anodes. *Advanced Energy Materials*, 3(11):1507–1515, 2013.
- [257] M. Wakihara. Recent developments in lithium ion batteries. *Materials Science and Engineering: R: Reports*, 33(4):109–134, 2001.
- [258] C. P. Grey and J. M. Tarascon. Sustainability and in situ monitoring in battery development. *Nature Materials*, 16(1):45–56, 2017.
- [259] M. Clites, B. W. Byles, and E. Pomerantseva. Effect of aging and hydrothermal treatment on electrochemical performance of chemically pre-intercalated Na-V-O nanowires for Na-ion batteries. *Journal of Materials Chemistry A*, 4(20):7754–7761, 2016.
- [260] S. G. McArthur, L. Geng, J. Guo, and V. Lavallo. Cation reduction and comproportionation as novel strategies to produce high voltage, halide free, carborane based electrolytes for rechargeable Mg batteries. *Inorganic Chemistry Frontiers*, 2(12):1101–1104, 2015.
- [261] B. W. Byles, N. K. R. Palapati, A. Subramanian, and E. Pomerantseva. The role of electronic and ionic conductivities in the rate performance of tunnel structured manganese oxides in Li-ion batteries. *APL Materials*, 4(4):046108, 2016.

- [262] A. A. Talin, D. Ruzmetov, A. Kolmakov, K. McKelvey, N. Ware, F. El Gabaly, B. Dunn, and H. S. White. Fabrication, testing, and simulation of all-solid-state three-dimensional li-ion batteries. *ACS Applied Materials & Interfaces*, 8(47):32385–32391, 2016.
- [263] F. Han, Y. Zhu, X. He, Y. Mo, and C. Wang. Electrochemical stability of $\text{Li}_{10}\text{GeP}_2\text{S}_{12}$ and $\text{Li}_7\text{La}_3\text{Zr}_2\text{O}_{12}$ solid electrolytes. *Advanced Energy Materials*, 6(8):1501590, 2016.
- [264] N. Balke, S. Jesse, A. N. Morozovska, E. Eliseev, D. W. Chung, Y. Kim, L. Adamczyk, R. E. Garcia, N. Dudney, and S. V. Kalinin. Nanoscale mapping of ion diffusion in a lithium-ion battery cathode. *Nature Nanotechnology*, 5(10):749–754, 2010.
- [265] Q. Nataly Chen, Y. Liu, Y. Liu, S. Xie, G. Cao, and J. Li. Delineating local electromigration for nanoscale probing of lithium ion intercalation and extraction by electrochemical strain microscopy. *Applied Physics Letters*, 101(6):063901, 2012.
- [266] J. Zhu, L. Lu, and K. Zeng. Nanoscale mapping of lithium-ion diffusion in a cathode within an all-solid-state lithium-ion battery by advanced scanning probe microscopy techniques. *ACS Nano*, 7(2):1666–1675, 2013.
- [267] S. Kalinin, N. Balke, S. Jesse, A. Tselev, A. Kumar, T. M. Arruda, S. Guo, and R. Proksch. Li-ion dynamics and reactivity on the nanoscale. *Materials Today*, 14(11):548–558, 2011.
- [268] M. T. McDowell, S. W. Lee, J. T. Harris, B. A. Korgel, C. Wang, W. D. Nix, and Y. Cui. In situ TEM of two-phase lithiation of amorphous silicon nanospheres. *Nano Letters*, 13(2):758–764, 2013.
- [269] X. H. Liu, Y. Liu, A. Kushima, S. L. Zhang, T. Zhu, J. Li, and J. Y. Huang. In situ TEM experiments of electrochemical lithiation and delithiation of individual nanostructures. *Advanced Energy Materials*, 2(7):722–741, 2012.
- [270] M. T. McDowell, S. Xia, and T. Zhu. The mechanics of large-volume-change transformations in high-capacity battery materials. *Extreme Mechanics Letters*, 9, Part 3:480–494, 2016.
- [271] H. Takahara, M. Shikano, and H. Kobayashi. Quantification of lithium in LIB electrodes with glow discharge optical emission spectroscopy (GD-OES). *Journal of Power Sources*, 244:252–258, 2013.
- [272] D. X Liu, L. R. Cao, and A. C. Co. Demonstrating the feasibility of Al as anode current collector in Li-ion batteries via in situ neutron depth profiling. *Chemistry of Materials*, 28(2):556–563, 2016.

- [273] J. A. Dura, D. J. Pierce, C. F. Majkrzak, N. C. Maliszewskyj, D. J. McGillivray, M. Losche, K. V. O'Donovan, M. Mihailescu, U. Perez-Salas, D. L. Worcester, and S. H. White. AND/R: Advanced neutron diffractometer/reflectometer for investigation of thin films and multilayers for the life sciences. *Review of Scientific Instruments*, 77(7):074301, 2006.
- [274] S. C. DeCaluwe, B. M. Dhar, L. Huang, Y. He, K. Yang, J. P. Owejan, Y. Zhao, A. A. Talin, J. A. Dura, and H. Wang. Pore collapse and regrowth in silicon electrodes for rechargeable batteries. *Physical Chemistry Chemical Physics*, 17(17):11301–11312, 2015.
- [275] D. X. Liu and A. C. Co. Revealing chemical processes involved in electrochemical (de)lithiation of Al with in situ neutron depth profiling and X-ray diffraction. *Journal of the American Chemical Society*, 138(1):231–238, 2016.
- [276] A. Bordes, E. De Vito, C. Haon, C. Secouard, A. Montani, and P. Marcus. Investigation of lithium insertion mechanisms of a thin-film Si electrode by coupling time-of-flight secondary-ion mass spectrometry, X-ray photoelectron spectroscopy, and focused-ion-beam/SEM. *ACS Applied Materials & Interfaces*, 7(50):27853–27862, 2015.
- [277] J. Li, V. Maurice, J. Swiatowska-Mrowiecka, A. Seyeux, S. Zanna, L. Klein, S. Sun, and P. Marcus. XPS, time-of-flight-SIMS and polarization modulation IRRAS study of Cr_2O_3 thin film materials as anode for lithium ion battery. *Electrochimica Acta*, 54(14):3700–3707, 2009.
- [278] A. Bordes, E. De Vito, C. Haon, A. Boulineau, A. Montani, and P. Marcus. Multiscale investigation of silicon anode Li insertion mechanisms by time-of-flight secondary ion mass spectrometer imaging performed on an in situ focused ion beam cross section. *Chemistry of Materials*, 28(5):1566–1573, 2016.